

UNIVERSITAT POLITÈCNICA DE CATALUNYA

PHD PROGRAM IN PHOTONICS

**Detection of a single erbium ion in a
nanoparticle**

Author:
Chetan Deshmukh

Supervisor:
Prof. Dr. Hugues de
Riedmatten

*A thesis submitted to obtain the title of Doctor by the Universitat
Politècnica de Catalunya*

in the

QPSA - Quantum Photonics with Solids and Atoms *group*,
ICFO - The Institute of Photonic Sciences

March 18, 2022



Abstract

Encoding information into quantum mechanical properties of a system can lead to important applications in a wide array of fields, including computing and communication. Devices that will enable these applications can be envisioned to form part of a quantum network in the future. Quantum networks can be implemented using nodes that have the ability to generate and store entanglement efficiently for long durations as well as to process quantum information. The nodes also need to be interfaced with photons, which can faithfully carry information over long distances. Single rare-earth ions doped in crystals offer all these capabilities. The main goal of this thesis was to detect a single erbium ion, which operates in the telecommunication wavelength, in the solid-state and to investigate its feasibility as a spin-photon interface.

Detecting a single erbium is challenging due to its low emission rate, but it can be aided by Purcell-enhancing its emission via coupling to an optical cavity. In this thesis, we utilize erbium ions doped into nanoparticles, which facilitates their integration into cavities with small mode-volume that can achieve high Purcell-enhancement. In addition, nanoparticles provide the confinement required to isolate and individually manipulate spatially close-by single ion qubits, which is required for dipolar quantum gates. We hence first study the optical coherence properties of $\text{Er}^{3+}:\text{Y}_2\text{O}_3$ nanoparticles at cryogenic temperatures. We identify the mechanisms that limit the measured values and identify potential avenues for improvement in the future. We also study the optical and spin coherence properties of $\text{Pr}^{3+}:\text{Y}_2\text{O}_3$, which is a promising alternative to erbium.

Fiber-based microcavities can achieve high Purcell factors as they can simultaneously realize high finesse and small mode-volume. They are also ideally suited to be coupled to nanoparticles due to their tuning capabilities. However, stabilizing such a cavity inside a cryogenic environment, which is required to preserve the coherence properties of $\text{Er}^{3+}:\text{Y}_2\text{O}_3$ nanoparticles, is challenging. We hence first describe the construction of a custom setup, which enables us to stabilize the cavity while being coupled to a suitable nanoparticle at cryogenic temperatures. Utilizing the first iteration of this setup, we then report on the successful coupling of $\text{Er}^{3+}:\text{Y}_2\text{O}_3$ nanoparticles to a fiber-based high finesse microcavity. We achieve an average Purcell factor of 14 for a small ensemble of ions, while a small subset of ions show Purcell factor up to 70. We explain the obtained multi-exponential decay behaviour with the help of a detailed model. Furthermore, we demonstrate dynamic control of the Purcell-enhanced emission by tuning the cavity resonance on a time-scale faster than the spontaneous emission rate of the ions. This allows us to extract the natural lifetime of the ions as well as to shape the waveform of the emitted photons. However, we conclude that the achieved signal-to-noise ratio is not high enough to resolve single erbium ions.

For the final experiment, we operate the second iteration of the setup, which improves our sensitivity to single erbium ions by more than a factor 50. This enables us to demonstrate the first detection of a single erbium ion in a nanoparticle. The ion exhibits a Purcell factor of 60, leading to a cavity enhanced lifetime of $225 \mu\text{s}$, and a homogeneous linewidth of 380 MHz. The counts received from the ion show a clear saturation and we measure the second-order auto-correlation of the emitted photons to be 0.59, which reduces to 0.29 after background-subtraction. This is strong evidence that the photons are emitted by a single erbium ion. Our work opens the path for exploring single rare-earth-ions doped into nanoparticles as spin-photon interfaces for quantum information processing.

Resumen

La codificación de la información en las propiedades mecánico-cuánticas de un sistema puede dar lugar a aplicaciones en muchos campos, como la informática y la comunicación. Podemos imaginar que los dispositivos que permitan estas aplicaciones formen parte de una red cuántica en el futuro. Las redes cuánticas pueden implementarse utilizando nodos que tengan la capacidad de generar y almacenar el entrelazamiento de forma eficiente durante largos periodos de tiempo, así como de procesar la información cuántica. Los nodos también necesitan una interfaz con fotones, ya que estos pueden transportar fielmente la información a largas distancias. Los iones individuales de tierras raras dopados en cristales ofrecen todas estas capacidades. El objetivo principal de esta tesis fue detectar un ion individual de erbio, que opera en la longitud de onda de las telecomunicaciones, e investigar su viabilidad como interfaz espín-fotón.

La detección de un ion individual de erbio es un reto debido a su baja tasa de emisión, pero esta puede mejorarse mediante el acoplamiento a una cavidad óptica, debido al efecto Purcell. En esta tesis, utilizamos iones de erbio dopados en nanopartículas, lo que facilita su integración a cavidades con volúmenes de modo pequeños. Además, las nanopartículas proporcionan el confinamiento necesario para manipular bits cuánticos de iones individuales cercanos espacialmente, lo cual es necesario para construir puertas cuánticas dipolares. Por ello, estudiamos primero las propiedades de coherencia óptica de las nanopartículas de $\text{Er}^{3+}:\text{Y}_2\text{O}_3$ a temperaturas criogénicas. Identificamos los mecanismos limitantes e identificamos las vías de mejora en el futuro. También estudiamos las propiedades de coherencia

óptica y de espín de $\text{Pr}^{3+}:\text{Y}_2\text{O}_3$, que es una alternativa prometedora al erbio.

Las microcavidades basadas en fibra pueden alcanzar elevados factores de Purcell, ya que pueden lograr simultáneamente una gran finura y un pequeño volumen de modo. También son idóneas para ser acopladas a nanopartículas debido a su capacidad para ajustar la frecuencia de resonancia. Sin embargo, estabilizar una cavidad de este tipo en un entorno criogénico es un reto. Primero, describimos la construcción de un sistema personalizado que nos permitió estabilizar la cavidad mientras se acoplaba a una nanopartícula adecuada. Utilizando la primera iteración de esta configuración, informamos sobre el acoplamiento de nanopartículas de $\text{Er}^{3+}:\text{Y}_2\text{O}_3$ a una microcavidad de alta precisión basada en fibra. Conseguimos un factor Purcell medio de 14 para un pequeño conjunto de iones, mientras que un pequeño subconjunto de iones mostró un factor Purcell de hasta 70. Explicamos el comportamiento de decaimiento multiexponencial obtenido utilizando un modelo detallado. Además, demostramos el control dinámico de la emisión potenciada por el efecto Purcell ajustando la resonancia de la cavidad en una escala de tiempo más rápida que la tasa de emisión espontánea de los iones. Esto nos permitió extraer el tiempo de vida natural de los iones, así como moldear la forma de onda de los fotones emitidos.

Para el experimento final, operamos la segunda iteración de la configuración, que mejoró nuestra sensibilidad a los iones individuales de erbio en más de un factor 50. Esto nos permitió demostrar la primera detección de un ion de erbio en una nanopartícula. El ión presentó un factor Purcell de 60, lo que da un tiempo de vida realzado por la cavidad de $225 \mu\text{s}$, y un ancho de línea homogéneo de 380 MHz. Los recuentos recibidos del ion mostraron una clara saturación y la medida de autocorrelación de segundo orden de los fotones emitidos resultó en 0,59, que se reduce a 0,29 tras la sustracción de fondo. Esto es una fuerte evidencia de que los fotones son emitidos por un ion individual de erbio. Nuestro trabajo abre el camino para explorar los iones individuales de tierras raras dopados en nanopartículas como interfaces de espín-fotón para el procesamiento de información cuántica.

Acknowledgements

First of all, I would like to thank Hugues for giving me the opportunity to start this exciting experiment together with Bernardo in his group. We both knew this project would be challenging, but I don't think we anticipated just *how* difficult it actually turned out to be. But Hugues was always patient. He supported and motivated us when the going looked tough, but also inspired us to dream big. His door was always open to have discussions, be it scientific or personal, and I feel tremendously lucky to have had him as my advisor during the last five years.

I started this journey together with Bernardo, and I cannot imagine having done it without him. Working with him was undoubtedly the greatest learning experience of my lifetime. He was full of practical knowledge and advice, and I hope to carry some of it forward in the future. He has been a great mentor to me, both inside and outside the lab, and I will always cherish our time together here in Barcelona.

When I came to Spain from Canada five years ago, the amazing members of the QPSA group immediately made me feel like part of a family and I will forever be grateful to all of them. Their empathy and friendliness made stressful times more bearable and the fun times even more so. They are also a team of incredibly talented people and I have learnt so much from each one of them. They taught me the value of collaborative science, and I know they will go on to do great things in their lives.

Last but not least, I would like to thank my family for supporting me in my endeavour to get a PhD. Even though it wasn't easy for them to explain to others why their son was still a 'student' after so many years,

they never let it affect my ambitions. This PhD (if I defend it successfully!) feels as much theirs as it is mine.

List of publications

Published manuscripts

- B. Casabone*, C. Deshmukh*, S. Liu, D. Serrano, A. Ferrier, T. Hümmer, P. Goldner, D. Hunger & H. de Riedmatten. *Dynamic control of Purcell enhanced emission of erbium ions in nanoparticles*. Nature Communications 12 (2020).
- D. Serrano, C. Deshmukh, S. Liu, A. Ferrier, H. de Riedmatten & P. Goldner. *Coherent optical and spin spectroscopy of nanoscale $Pr^{3+}:Y_2O_3$* . Physical Review B 100 (2019).

Manuscripts in preparation

- C. Deshmukh*, M. Alquidra*, D. Serrano, B. Casabone, S. Liu, A. Ferrier, P. Goldner, A. Walther & H. de Riedmatten. *Optical coherence properties of nanoscale Kramers' rare-earth ions for quantum applications*. To be submitted (2022).
- C. Deshmukh*, E. Beattie*, S. Grandi, B. Casabone, D. Serrano, A. Ferrier, S. Liu, P. Goldner, D. Hunger & H. de Riedmatten. *Detection of a single erbium ion in a nanoparticle*. To be submitted (2022).

* : Equally contributing authors

Contents

1	Introduction	1
1.1	Quantum networks	1
1.2	Quantum nodes with single emitters	3
1.2.1	Single emitters in the solid-state	4
1.3	Rare-earth ions doped in crystals	5
1.3.1	Single rare-earth ions	6
1.4	Our system	7
1.4.1	Structure of this thesis	7
2	Theoretical background	10
2.1	Rare-earth ions	10
2.1.1	Energy level structure	11
2.1.2	Optical and spin spectroscopic properties	12
2.1.3	Rare-earth ion doped nano-materials	14
2.2	Atom-cavity coupling	14
2.3	Single emitter properties	17
2.3.1	Emitter saturation, Rabi frequency & linewidth	17
2.3.2	Statistics of light from single emitters	18
2.4	Cavity parameters	19
2.4.1	Mode of a cavity	19
2.4.2	Cavity finesse	21

3	Experimental setup	23
3.1	Erbium doped nanoparticles	24
3.1.1	Material synthesis	24
3.1.2	Number of erbium ions	26
3.1.3	Scattering loss	26
3.1.4	Preparing nanoparticles on planar mirror	28
3.2	Fiber microcavity	29
3.2.1	Dielectric coating	33
3.2.2	Purcell factor	37
3.2.3	Mode matching	38
3.2.4	Expected single-ion count rate	39
3.2.5	Lower transmissivity planar mirror	42
3.2.6	Estimating cavity-emitter parameters	43
3.3	Nano-positioner	45
3.3.1	Fiber and mirror holder	49
3.4	Cavity stability	52
3.5	Localizing nanoparticles	56
4	Spectroscopy of nano-scale $\text{Er}^{3+}:\text{Y}_2\text{O}_3$ and $\text{Pr}^{3+}:\text{Y}_2\text{O}_3$	59
4.1	Material	60
4.2	Methods	61
4.2.1	Sample preparation	61
4.2.2	Optical setup	61
4.3	Results	63
4.3.1	Branching ratio	63
4.3.2	Inhomogeneous linewidth and lifetime	64
4.3.3	Homogeneous linewidth versus temperature	66
4.3.4	Spectral diffusion via three-pulse echo	69
4.4	Prospects as a source of indistinguishable photons	71
4.5	$\text{Pr}^{3+}:\text{Y}_2\text{O}_3$ nanoparticles	73
4.5.1	Optical homogeneous linewidth	77
4.5.2	Spin coherence properties	80
4.5.3	Single Pr^{3+} ion as a spin-photon interface	82

5	Dynamic control of Purcell-enhanced emission	84
5.1	Introduction	85
5.2	Experimental setup	86
5.2.1	Cavity stability	88
5.3	Measurement of Purcell enhancement	91
5.4	Cavity switching	95
5.4.1	Measuring natural lifetime	97
5.4.2	Dynamic switching	99
5.5	Number of ions	101
5.6	Conclusion	103
6	Detection of a single erbium ion	104
6.1	Experimental setup	105
6.1.1	Experimental parameters	106
6.2	Results	107
6.2.1	Spectrum of a single ion	108
6.2.2	Purcell enhancement of a single ion	111
6.2.3	Measurement of $g^{(2)}(0)$	111
6.2.4	Higher Purcell factors	115
6.3	Conclusion	117
7	Conclusion & Outlook	119
7.1	Main results of this thesis	119
7.2	Outlook	121
A	Appendix	123
A.1	Model for multi-exponential decay	123
A.2	Cavity switching time	129
A.3	Emitters coupled to an off-resonance cavity	133

List of Figures

1.1	Illustration of a quantum repeater scheme	3
2.1	Plano-concave cavity	20
3.1	SEM image of the synthesized nanoparticles	25
3.2	Total scattering loss $2B$ induced by a nanoparticle inside a cavity as a function of its diameter.	27
3.3	Schematic drawing of the tunable fiber-based microcavity .	30
3.4	Mode volume V_m for a range of radius of curvatures R and lengths L	31
3.5	Overview of fibers with different radius of curvatures R and structural depths z_t	32
3.6	Transmissivity of fiber and planar mirror	33
3.7	Finesse of the cavity as a function of wavelength	34
3.8	Electric field intensity as a function of distance from the surface of the planar mirror	35
3.9	Effective Purcell factor C for $\text{Er}^{3+}:\text{Y}_2\text{O}_3$ with $F = 19,000$ for a range of radius of curvatures R and lengths L	37
3.10	Mode matching ϵ between the fiber and cavity mode and the product $C\epsilon$ as a function of radius of curvatures R and lengths L	38
3.11	Relevant parameters of the fiber microcavity to estimate mode-matching and out-coupling efficiency	40

3.12	Expected count rate γ_f in the fiber as a function of R and L	41
3.13	Picture of the second iteration of the nano-positioner indicating all the important components	45
3.14	Assembly of the fiber holder and mirror holder showing all the components utilized for fine-tuning and coarse-tuning the fiber and mirror	49
3.15	Cavity stability with and without the cryostat pump in the second iteration of our setup	54
3.16	Transmission of the cavity at 1535 nm in quiet parts of the cryostat cycle when the second iteration of our setup is cold	55
3.17	Map of normalized transmission signal and estimated scattering loss on a nanoparticle	57
4.1	SEM image of nanoparticles	60
4.2	Sample holder for both the ceramics and the nanoparticles .	62
4.3	Fluorescence spectra of $\text{Er}^{3+}:\text{Y}_2\text{O}_3$ nanoparticles	63
4.4	Measurement of inhomogeneous linewidth of $\text{Er}^{3+}:\text{Y}_2\text{O}_3$. .	64
4.5	Measurement of lifetime of $\text{Er}^{3+}:\text{Y}_2\text{O}_3$	65
4.6	Coherence time at lowest temperature of $\text{Er}^{3+}:\text{Y}_2\text{O}_3$	66
4.7	Homogeneous linewidth versus temperature of $\text{Er}^{3+}:\text{Y}_2\text{O}_3$.	68
4.8	Spectral diffusion of $\text{Er}^{3+}:\text{Y}_2\text{O}_3$	70
4.9	Fluorescence spectra of $\text{Pr}^{3+}:\text{Y}_2\text{O}_3$ nanoparticles	75
4.10	Optical inhomogeneous line of $\text{Pr}^{3+}:\text{Y}_2\text{O}_3$	76
4.11	Excited state lifetime of $\text{Pr}^{3+}:\text{Y}_2\text{O}_3$ nanoparticles	77
4.12	Coherence time at a temperature of 1.4 K of $\text{Pr}^{3+}:\text{Y}_2\text{O}_3$. .	78
4.13	Dependence of optical homogeneous linewidth on temperature of $\text{Pr}^{3+}:\text{Y}_2\text{O}_3$ ceramics	79
4.14	Hyperfine structure of $\text{Pr}^{3+}:\text{Y}_2\text{O}_3$ and spin coherence	81
5.1	Schematic of experimental setup	87
5.2	Locking the microcavity	88
5.3	Cavity noise spectrum	89
5.4	Map of scattering loss	91
5.5	Purcell enhanced lifetime measurements	92

5.6	Model to describe multi-exponential decay	93
5.7	Distribution of Purcell factors	95
5.8	Scheme to stabilize the length of the cavity on/off resonance with the ions	96
5.9	Sequence used to extract the natural lifetime.	97
5.10	Counts recorded as function of time for different delays	98
5.11	Counts as function of time as the cavity is switched dynamically	99
5.12	Rising and falling edge as the cavity is switched	100
5.13	Number of photons generated in the cavity mode as a function of the excitation power before the cavity	101
6.1	Counts received per trial as a function of laser frequency detuning from 1535.49 nm	107
6.2	Counts received per trial from ‘Ion 1’ as a function of laser frequency detuning from 1535.49 nm for different mean intra- cavity photon numbers	109
6.3	Counts received per trigger and linewidth of the emitter as a function of mean intra-cavity photon number	110
6.4	Purcell-enhanced lifetime of a single ion	112
6.5	Coincidence counts as a function of trial difference	113
6.6	Value of raw and corrected $g^{(2)}(0)$ as a function of the win- dow size considered	114
6.7	High Purcell-enhancement observed on a different nanoparticle	116
A.1	Normalized distributions p_d and p_{sw}	127
A.2	Reduction of the Purcell factor and the count-rate as func- tion of time	130
A.3	Residual noise in the cavity as a function of the switching time	132

List of Tables

3.1	Comparison between the two iterations of the setup including the temperature reached and the cavity stabilities achieved	51
-----	--	----

Chapter 1

Introduction

The quantum mechanical properties of a system, such as superposition and entanglement, have completely revolutionized our understanding of nature. The field of quantum information science involves encoding information into these quantum mechanical properties and studying how they behave. The basic unit into which quantum information is encoded in the discrete regime is called a quantum bit or ‘qubit’, which is analogous to a bit in classical computing. These studies have led to the proposal of several potentially ground-breaking applications including quantum computing and quantum simulation [1–3], which could solve certain problems that are beyond the reach of classical computers, quantum communication [4–6], which guarantees unconditionally secure transmission of information, and quantum sensing [7], which allows for ultra-precise measurements of physical properties of systems. Quantum devices with these capabilities can be interlinked in the future to form part of a quantum internet [8].

1.1 Quantum networks

Single photons are the medium of choice for the transfer of quantum information over such a quantum internet as they can faithfully carry it over long distances. However, the distance to which photons can be transmitted

directly will be limited due to their attenuation via absorption or scattering. And unlike classical communication, single qubits cannot be amplified without adding noise due to the no-cloning theorem. One solution to this problem involves what is called as a ‘quantum repeater’ [6, 9]. The main idea is to divide the total distance over which quantum information has to be transmitted into smaller ‘elementary links’ over which entanglement can be distributed and stored independently. Once this is achieved, entanglement can then be extended between any two nodes via so-called ‘entanglement-swapping’ operations. See Fig. 1.1 for a simple illustration of this idea, where we want to transfer quantum information between nodes A and D. We first divide the distance between A and D into two smaller elementary links, namely A-B and C-D. We begin by creating and storing entanglement between links A-B and C-D. We can then perform an entanglement-swapping operation at nodes B and C, which will result in the entanglement of nodes A and D. The entanglement-swapping operation is a so-called ‘Bell-state measurement’ (BSM) that projects the combined state onto a Bell-state [10].

The hardware necessary to realize the nodes of such a quantum network should satisfy certain conditions. Firstly, it needs to be able to generate and store entanglement efficiently for long durations. This means that the ‘de-coherence’ time, which characterizes the decay of quantum information with time, needs to be long. Second, it should be able to efficiently transfer quantum information to distant nodes via photons. It would be hugely beneficial for these photons to be at telecommunication wavelengths, as then these photons can be easily sent via existing commercial telecommunication fibers. The capability to multiplex in additional degrees of freedom would also be greatly beneficial in enhancing the efficiency to transfer quantum information. Finally, the nodes should be able to process quantum information, such as performing entanglement-swapping operations as described above.

Several platforms are currently investigated for the realization of quantum nodes, including cold atomic ensembles [9, 11, 12], neutral atoms [13], and trapped ions [14]. Several systems in the solid-state are also being studied, including vacancy centres in diamond [15, 16], quantum dots [17],

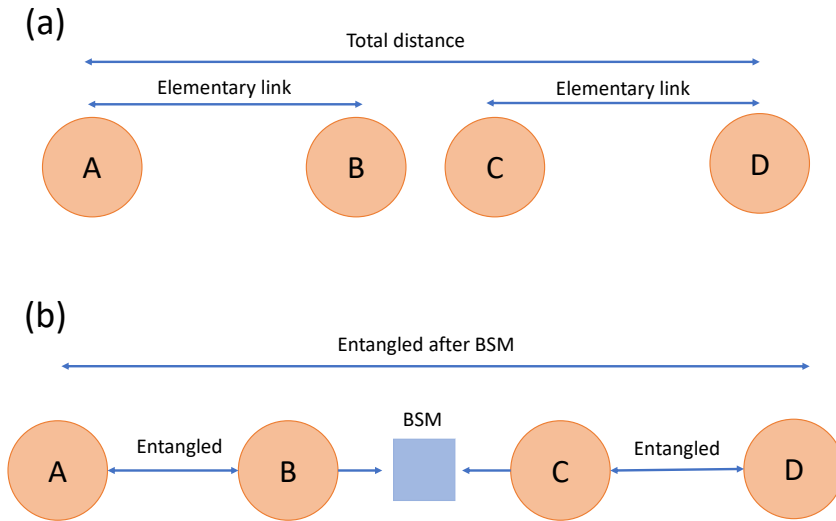


Figure 1.1: Illustration of a quantum repeater scheme. (a) A and D represent the two nodes over which quantum information has to be transferred. A-B and C-D constitute the elementary links over which entanglement is created first. (b) A Bell-state measurement (BSM) operation at nodes B and C results in the entanglement of nodes A and D.

rare-earth ion doped crystals [6, 18, 19], as well as optically active defect centres in a host of other materials [20].

1.2 Quantum nodes with single emitters

Single emitters with long-lived spin-states connected to an optical transition are a promising platform for building quantum networks. They also provide quantum processing capabilities which are highly desirable for the nodes of

a quantum internet [14, 21]. Single emitters can generate a photon that is entangled with the spin-state, which can then be transmitted to another node of a quantum internet. A Bell-state measurement between two such photons that are each entangled with a different emitter would entangle the two emitters.

One way to generate entanglement with single emitters involves the spontaneous decay from the optical excited state down to the spin-state generating spin-photon entanglement [22]. Since this process is not directional, it practically limits the efficiency with which this photon can be collected for distribution. However, the efficiency of collection can be increased by the use of an optical cavity in the Purcell regime [13, 23–25]. Purcell effect enhances the spontaneous emission rate of the emitter, which also results in the channelling of emission from the emitter into the cavity mode. In addition, Purcell enhancement also increases the indistinguishability of photons from the emitter in the presence of dephasing, which is crucial for a successful Bell-state measurement. Hence, sufficiently high Purcell enhancement could simultaneously enable fast and near-unity efficiency generation of indistinguishable single photons which would be highly desirable for quantum network applications.

1.2.1 Single emitters in the solid-state

Single emitters in the solid state are promising quantum hardware candidates as they offer miniaturization and scalability, both of which would be important to enable quantum networks over long distances [20]. Platforms such as vacancy centres in diamond [15, 16, 26], and quantum dots [17, 27] have been widely studied and used for demonstrating several key elements of a quantum internet, including the first loophole-free Bell-inequality violation [16]. However, it is necessary to couple these emitters to cavities to increase the efficiency of the spin-photon interface, which would require some nano-structuring of the host material.

This has proven very challenging due to significant additional dephasing in nano-structured materials. This can result from several mechanisms, including increased coupling to charge or magnetic noise on the surface of

the material as well as degradation of the host material due to the fabrication process. For instance, nitrogen vacancy centres implanted in diamond films with $\sim 1 \mu\text{m}$ thickness result in spectral diffusion of $\sim 1 \text{ GHz}$ [28], which is more than an order of magnitude higher than that in bulk diamond samples. While some recent works have improved upon these results [29], achieving properties similar to bulk samples in nano-scale materials remains challenging. While silicon vacancy centres have shown much better optical properties in nano-photonic structures [26], they need to be cooled to extremely low temperatures in order to achieve reasonable spin coherence times [25], which would be impractical to scale up. Vacancy centres due to other group-IV elements, such as tin, have shown much better spin coherence properties [30] and look promising to be successfully integrated into nano-photonic structures.

Even though quantum dots in semiconductors were one of the first solid-state platforms to be strongly coupled to micro-cavities in 2007 [31], achieving it while maintaining the optical coherence properties similar to bulk samples was only done recently [23]. Quantum dots have also shown short spin coherence times due to coupling to charge and magnetic noise of the host material [32]. However, some recent works on quantum dots in isotopically pure silicon have shown dramatic improvements in spin coherence times [33], which could make them promising for quantum networks [34].

In addition, a myriad of other solid-state emitters, including vacancy centres in silicon carbide [35], organic molecules [24], and rare-earth ions doped into crystals [36], are all being investigated to be used as an efficient cavity-enhanced spin-photon interface for quantum networking applications [20].

1.3 Rare-earth ions doped in crystals

Among solid-state materials, rare-earth ion doped crystals constitute a promising platform for quantum information processing and networking. They feature exceptional coherence properties on the $4f^n \rightarrow 4f^n$ inner-shell transitions when cooled to cryogenic temperatures due to shielding

from the outer lying $5s$ and $5p$ electrons [37]. In addition, they have also shown long spin coherence times [38–40], which could be used to store quantum information. They have hence been used extensively in ensembles as quantum memories [18, 19, 41–44].

In addition, rare-earth ions possess permanent dipole moments which are different in the ground and excited states, which enables strong dipolar interactions between nearby ions. This can enable the realization of quantum gates between two or more ions using a dipole blockade mechanism achieved by exciting one ion [45]. For example, a dipole-blockade gate between erbium and another ion species can greatly enhance the rate of entanglement distribution in a quantum network [46–48].

1.3.1 Single rare-earth ions

The $4f^n \rightarrow 4f^n$ transitions have very low emission rates, which makes detecting a single rare-earth ion challenging. Initial pioneering work to detect single rare-earth ions in the solid-state was performed in free-space by utilizing transitions to outer lying levels [49, 50], which have faster emission rates and higher quantum efficiencies. However, these transitions do not display the same coherence properties as the inner-shell transitions. A later work also detected a single Pr^{3+} ion using the inner shell transition but had a limited count-rate [51].

Recently, there have been several efforts to couple rare-earth ions to photonic cavities in order to enhance their emission on the $4f^n \rightarrow 4f^n$ transition and enable the detection of single ions. Utilizing evanescent coupling between Er^{3+} ions in Y_2SiO_5 and a nano-photonic resonator fabricated in silicon, Dibos et al. were able to detect a single erbium ion by enhancing its emission by a factor of 650 [52]. Further, by using selective Purcell enhancement of the spin-conserving transition in this setup, the authors were able to demonstrate single-shot readout of the spin-state [53] as well as coherent control of six spin-states with spatial separations within the diffraction limit of the control light [54]. Zhong et al. fabricated a nano-photonic resonator within the host YVO_4 crystal to detect single Nd^{3+} ions with an almost radiatively limited linewidth [55]. Employing

a similar setup, Kindem et al. have shown coherent optical and spin manipulation of a single Yb^{3+} ion [56]. Alternately, Ulanowski et al. were able to detect and a single Er^{3+} ion by embedding a $20\ \mu\text{m}$ thin crystal of $\text{Er}^{3+}:\text{Y}_2\text{SiO}_5$ into a Fabry-Perot resonator [57].

1.4 Our system

Rare-earth ions have been recently demonstrated to preserve their coherence properties in nanoparticles [58–60]. Their extremely small size enables integration into microcavities to reach strong Purcell enhancement, as is necessary for the emission of indistinguishable single photons in the presence of dephasing. In addition, nanoparticles provide the confinement required to isolate and individually manipulate spatially close-by single ion qubits ($\approx 10\ \text{nm}$ distance), as required for dipolar quantum gates [45].

For the experiments in this thesis, we will investigate erbium doped into Y_2O_3 nanoparticles coupled to a fiber-based microcavity. The ${}^4I_{15/2} - {}^4I_{13/2}$ transition in erbium lies in the telecom band and is hence very attractive from the prospect of integrating it into existing commercial telecom fiber networks. It has shown excellent optical and spin coherence properties in bulk materials [40, 61, 62]. But its coherence properties have not been measured in nano-structured materials, which is one of the goals of this thesis. The microcavity is composed of a fiber-mirror with a concave structure on the tip of the fiber on one side while the other side is a planar mirror. Such a fiber-based microcavity can achieve high Purcell factors of up to 10^4 [63], provide open access to the cavity mode for optimal overlap between the ions and the cavity field [64–66], and are small and lightweight enough to offer fast frequency tuning. Additionally, since the fiber can be used to access the cavity mode, it opens up opportunities for integrating it into an all-fiber setup.

1.4.1 Structure of this thesis

We begin this thesis by giving a theoretical description of the emitter-cavity coupling in Ch. 2. This chapter includes an introduction to rare-earth ions

doped into crystals and the behaviour of an emitter coupled to an optical cavity such as Purcell enhancement. We also derive various experimental cavity and emitter parameters that will be useful to characterize our setup. These include the cavity mode volume, cavity finesse, emitter-field coupling parameter, Rabi frequency and saturation parameter of the emitter, as well as its power-broadened linewidth.

Next, in Ch. 3, we describe details of our experimental setup. This chapter includes details about the synthesis of $\text{Er}^{3+}:\text{Y}_2\text{O}_3$ nanoparticles, their scattering cross section and the total number of erbium ions present in a nanoparticle with the average diameter. We then describe details about our fiber based micro-cavity, including the expected maximum Purcell enhancement for $\text{Er}^{3+}:\text{Y}_2\text{O}_3$ nanoparticles coupled to such a cavity, and the expected count-rate from a single erbium ion with realistic experimental parameters. We also custom built two versions of a so-called ‘nano-positioning’ stage to enable the operation of our setup in a cryogenic environment. Sec. 3.3 includes all the details about the nano-positioner, including the achieved stability of our microcavity, the total fine and coarse tuning range, and the final temperatures reached for various components of the setup.

In Ch. 4, we investigate the optical coherence properties of $\text{Er}^{3+}:\text{Y}_2\text{O}_3$ at cryogenic temperatures, including mechanisms that broaden the linewidth. With the measured properties of the current samples and the available state of the art technologies, we also study the feasibility of using single erbium ions as a source of indistinguishable photons. In the last section of this chapter, we study Pr^{3+} as an alternative to Er^{3+} by investigating the optical and spin coherence properties of the $^1D_2 - ^3H_4$ transition at 619 nm in Pr^{3+} doped into Y_2O_3 nanoparticles.

In Ch. 5, using the first iteration of our nano-positioner system, we report on the Purcell-enhanced emission from an ensemble of erbium ions (down to ≈ 10 ions) doped into Y_2O_3 nanoparticles coupled to our fiber microcavity. The emission is multi-exponential, which can be explained using a model that considers the limited stability of our cavity and the random dipole orientation of erbium ions in the nanoparticle. We demonstrate that by physically moving the fiber mirror with sub-nanometre precision using

a piezoelectric device we can tune the resonance frequency of our cavity on a time scale much faster than the spontaneous emission lifetime of erbium ions. We use this capability to show that we can shape in real time the Purcell enhanced emission of the ions to control the emitted photons' waveforms, without perturbing the emitter.

In Ch. 7, we report on the detection of a single erbium ion in $\text{Er}^{3+}:\text{Y}_2\text{O}_3$ nanoparticles coupled to a fiber micro-cavity. Sec. 6.1 describes several improvements we made to the setup that was used in Ch. 5 so as to enable higher sensitivity to single Er^{3+} ions. All the obtained results, including the spectrum of the isolated single ion and its Purcell enhanced lifetime are reported in Sec. 6.2. We also perform a measurement of the $g^{(2)}(0)$ of the emitted photons and illustrate how it is limited by the signal to noise ratio. Sec. 6.3 concludes the chapter with a summary of all the results.

Chapter 2

Theoretical background

This chapter provides a theoretical framework for the rest of the thesis. We begin by introducing rare-earth ions in Sec. 2.1, which includes details about their energy level structure, and their optical and spin coherence properties in bulk and nano-structured materials. In Sec. 2.2, we describe the behaviour of the atom-cavity system in the Purcell regime, including the Purcell enhancement experienced by the emitter. In Sec. 2.3, we detail all the relevant emitter parameters when coupled to an optical cavity, such as the Rabi frequency Ω , the saturation parameter S , as well as its power broadened linewidth Γ_{pb} . We also give a description of the second-order auto-correlation $g^{(2)}(0)$ function as a tool to measure the statistics of the emitted light. In Sec. 2.4 we describe the relevant cavity parameters such as cavity finesse and its mode volume, and rewrite the expected Purcell enhancement in terms of these experimental parameters.

2.1 Rare-earth ions

Rare-earth elements, when doped into certain solid-state inorganic crystals, form trivalent ions that feature interesting properties on the $4f^n \rightarrow 4f^n$ inner-shell transitions. These transitions, which are dipole-forbidden, become weakly allowed due to a mixing of energy levels in the presence of the

electrostatic field of the crystal. The resulting oscillator strengths are still extremely weak and hence these levels have slow relaxation rates. However, due to the outer lying $5s$ and $5p$ electrons, these transitions are shielded from the environment and are consequently less prone to de-coherence. When cooled to cryogenic temperatures, these transitions exhibit excellent coherence properties for both the optical and spin transitions [37], which makes them very promising for quantum network applications.

2.1.1 Energy level structure

The energy level structure of rare-earth ions doped in crystals is complex due to their high atomic number and perturbations by the solid-state matrix. The central Coulomb interaction of the nucleus and all the surrounding electrons is the strongest contributor to the energy level structure. The resulting energy levels are represented using the total orbital angular momentum L , the total spin angular momentum S and the total angular momentum J as $^{2S+1}L_J$. For Er^{3+} , which we study in this thesis, the ground and excited states of the transition at 1535 nm are $^4I_{15/2}$ and $^4I_{13/2}$, respectively.

The electrostatic interaction due to the crystal field is the next most significant contribution. The field splits each energy level into $2J + 1$ (for non-Kramers' ions) or $(2J + 1)/2$ multiplets (for Kramers' ions), which are called crystal field levels. Er^{3+} is a Kramers' ion as it has an odd number of electrons in the outer shell. It hence has 8 ($J = 15/2$) and 7 ($J = 13/2$) crystal field levels in the ground and excited state respectively. The energy separation between these multiplets is generally of the order few hundred GHz [37].

We then consider the interaction between the magnetic moment of the nucleus and that of the electrons, called the hyperfine interaction. This results in a further splitting of the energy levels into $2I + 1$ multiplets, where I is the total nuclear spin. Among the naturally occurring isotopes of Er^{3+} , only ^{167}Er (23 % abundance) has a nuclear spin $I = 7/2$, which results in 8 doubly degenerate levels in the ground and excited state. The interaction of the electron and nuclear spin with an externally applied magnetic field,

called the electron and nuclear Zeeman interaction, respectively, can also be an important consideration, especially for the case for Kramers' ions as they have a high magnetic moment for the electron spin. Interaction between the magnetic moment of the rare-earth ion with that of the host atoms, called the super-hyperfine interaction, forms the final contribution to the energy level structure.

2.1.2 Optical and spin spectroscopic properties

The oscillator strength of the $4f^n \rightarrow 4f^n$ inner-shell transitions in rare-earth ions is very small, which results in very long lifetimes for the excited state. Typical lifetimes, referred to as T_1 , range from hundreds of microseconds, such as for Tm^{3+} and Pr^{3+} , to a few milliseconds, such as for Eu^{3+} and Yb^{3+} , and up to 10 milliseconds for Er^{3+} . These transitions also lie in a wide range of wavelengths, from around 600 nm for Pr^{3+} to around 1535 nm for Er^{3+} [37].

As mentioned above, each of the ground and excited states constitute of multiple crystal field levels. Population transfer between different crystal field levels within the same energy level can happen extremely rapidly with the assist of phonons. These are called non-radiative processes. Cooling the crystals to cryogenic temperatures can get rid of available phonons in the crystal lattice and hence transitions involving the absorption of a phonon can be minimized. However, transitions involving the emission of a phonon depend on the phononic density of states, which cannot be prohibited easily [67]. In this context, transitions between the lowest lying crystal field level in the excited state to the lowest lying crystal field level in the ground state are interesting as there exist pathways between these levels that are purely radiative. These pathways are called zero-phonon-lines (ZPL). The probability of an emitter to decay to the lowest lying crystal field level from the excited state is called the branching ratio. Emitters with high branching ratios are particularly interesting as they can be easily manipulated and probed with optical pulses.

Due to shielding from the outer lying $5s$ and $5p$ electrons, ZPL transitions exhibit excellent coherence properties when cooled to cryogenic tem-

peratures [37]. The coherence time, referred to as T_2 , is related to its linewidth Γ_h as

$$\Gamma_h = 1/(\pi T_2) \quad (2.1)$$

The coherence time is limited fundamentally by the excited state lifetime as $T_2 \leq 2T_1$. However, in practice T_2 is lower than this limit due to the presence of additional dephasing. There are several factors that can contribute to dephasing. One source is the exchange of energy between two resonant spins in the vicinity of the emitter (referred to as a spin flip-flop) that could lead to a change in the local environment of the emitter. In solid-state materials, interaction with the host material in the form of coupling to phonons or via additional spins present in the host matrix leads to additional forms of dephasing. These mechanisms can have very different time-scales, with some causing spectral-diffusion on longer time scales. The effective linewidth of the ion could hence be broadened beyond the value given by its coherence time. Significant work has been done in trying to push the coherence time of several rare-earth ions towards their fundamental limit [62, 68, 69]. This has enabled their extensive use as ensemble-based quantum memories [18, 19, 41–44].

In addition to homogeneous linewidth, rare-earth ion doped materials experience a shifting in their spectral lines due to the inhomogeneity of the crystal field. This results in a so-called ‘inhomogeneous linewidth’ which is orders of magnitude larger than the homogeneous linewidth at low temperatures [37, 69]. This opens up opportunities for multiplexing in the spectral domain that is particularly useful for quantum network applications [70, 71]. If the rare-earth ions are doped sparsely, then this also enables individually addressing potentially a large number (~ 1000) of qubits based on single rare-earth ions via optical pulses [54, 57].

Moreover, the hyperfine transitions in rare-earth ions have demonstrated exceptional properties [40, 72], including a coherence time that was extended using dynamical decoupling to six-hours in $\text{Eu}^{3+}:\text{Y}_2\text{SiO}_5$, which is a record for any solid-state material. This has allowed them to be used as spin-photon interfaces in several demonstrations [44, 73–75].

2.1.3 Rare-earth ion doped nano-materials

Due to their exceptional optical and spin coherence properties, single rare-earth ions are an ideal candidate for a spin-photon interface with applications in quantum networking. In addition, rare-earth ions possess permanent dipole moments which are different in the ground and excited states, which enables strong dipolar interactions between nearby ions. This can enable the realization of quantum gates between two or more ions using a dipole blockade mechanism achieved by exciting one ion [45]. For example, a dipole-blockade gate between erbium and another ion species can greatly enhance the rate of entanglement distribution in a quantum network [46].

However, due to the low emission rates of the coherent transitions, detecting a single rare-earth ion has proved challenging. Some initial pioneering work to detect single rare-earth ions in free space was done by exciting the ions to outer levels with faster emission rates [49, 50]. A single Pr^{3+} ion has also been detected using the inner shell transition but with a limited count-rate [51]. Alternately, the weak transitions of rare-earth ions can be enhanced by coupling them to a cavity with high Q/V to enable single ion detection. This would require some nano-structuring of the host material, which causes significant additional dephasing of the emitter [76]. Although several recent works have demonstrated significant improvements in the coherence times [58–60, 77], they still remain far from the values obtained in bulk materials, which makes their use as spin-photon interfaces challenging.

In Ch. 4 of this thesis, we investigate the optical coherence properties of $\text{Er}^{3+}:\text{Y}_2\text{O}_3$ at cryogenic temperatures and identify the limiting mechanisms. In Sec. 4.5, we also study the optical and spin coherence properties of $\text{Pr}^{3+}:\text{Y}_2\text{O}_3$ as an alternative to erbium.

2.2 Atom-cavity coupling

In this section, we provide a description of the coupling between an atom and an electromagnetic field. Since we use an optical cavity in this thesis, we will assume in this section that the field is that of a single-mode cavity. Following a standard description, such as the one given in [78], the full

Hamiltonian of the system can be written as

$$\hat{H} = \hat{H}_a + \hat{H}_f + \hat{H}_{int} \quad (2.2)$$

where \hat{H}_a , \hat{H}_f and \hat{H}_{int} are the Hamiltonians of the free atom, the cavity field and the interaction between atom and field, respectively. For a two level system with eigenstates $|g\rangle$ and $|e\rangle$, the total Hamiltonian is given by the Jaynes-Cummings model as

$$\begin{aligned} \hat{H}_a &= \frac{\hbar\omega_0}{2} \hat{\sigma}_z \\ \hat{H}_f &= \hbar\omega \left(\hat{a}^\dagger \hat{a} + \frac{1}{2} \right) \\ \hat{H}_{int} &= \hbar g \left(\hat{a}^\dagger \hat{\sigma}_z + \hat{a} \hat{\sigma}_z^\dagger \right) \end{aligned} \quad (2.3)$$

where $\hat{\sigma}_z = |g\rangle\langle g| - |e\rangle\langle e|$ is the Pauli matrix, \hat{a} and \hat{a}^\dagger are the photon annihilation and creation operators of the cavity field, respectively, ω_0 and ω are the angular frequencies of the atom and field, respectively, and g is the coupling parameter between the emitter and the field. When the emitter is at the maximum of the electric field energy density and its dipole moment vector is aligned with the electric field vector, then it can be written as

$$g = \frac{\mu_{eg}}{\hbar} \sqrt{\frac{\hbar\omega}{2\epsilon_0 V_m}} \quad (2.4)$$

where μ_{eg} is the dipole moment of the atom, ϵ_0 is the vacuum permittivity and V_m is the volume of the cavity mode. To account for losses, we can introduce complex frequencies for the atom and field as

$$\begin{aligned} \omega_0 &\rightarrow \omega_0 - i \Gamma_1 \\ \omega &\rightarrow \omega - i \kappa \end{aligned} \quad (2.5)$$

where Γ_1 and κ are the decay rates of the emitter population and cavity field, respectively. For the case when the emitter and cavity are resonant

with each other ($\omega_0 = \omega$), the eigenvalues of the Jaynes-Cummings Hamiltonian are given as [78, 79]

$$\lambda_{\pm} = \omega_0 - i \frac{(\kappa + \Gamma_1)}{2} \pm \sqrt{g^2 - \frac{(\kappa - \Gamma_1)^2}{4}} \quad (2.6)$$

Considering the case where $\kappa \gg g \gg \Gamma_1$, which is considered the ‘Purcell’ regime, we can see that the solutions simplify to

$$\begin{aligned} \lambda_+ &= \omega_0 + i \frac{g^2}{\kappa} \\ \lambda_- &= \omega_0 + i \kappa \end{aligned} \quad (2.7)$$

The real values of both eigenfrequencies are the same ($= \omega_0$) but their imaginary parts are different. The rate of decay of energy in the two eigenstates is then given as $2g^2/\kappa$ and 2κ ¹. We can identify that the former is the rate of decay of the emitter which is modified by the presence of the cavity, and the latter is the decay of the cavity field which is unaffected by the presence of the emitter. The ratio C_0 of the modified spontaneous emission rate of the emitter due to the cavity to the one without the cavity Γ_1 can be written as

$$C_0 = \frac{2g^2}{\kappa\Gamma_1} \quad (2.8)$$

which is called the Purcell factor. If the emitter experiences no additional dephasing, then the C_0 is equivalent to the cooperativity. The spontaneous emission rate of the emitter in free space Γ_1 is given by the Fermi’s golden rule as [80]

$$\Gamma_1 = \frac{1}{3\pi} \frac{|\vec{\mu}_{eg}|^2 \omega_0^3}{\hbar \epsilon_0 c^3} \quad (2.9)$$

where $\vec{\mu}_{eg}$ is the dipole moment vector of the atom and ω_0 is the frequency of the atom. If the emitter is at the maximum of the electric field energy density of the cavity field and its dipole moment vector is perfectly aligned

¹The factor 2 arises because the decay of energy is given by the square of the imaginary part of the eigenfrequencies

with the electric field vector, then we can substitute Eq. 2.9 and Eq. 2.4 into Eq. 2.8 to obtain

$$C_0 = \frac{3(\lambda/n)^3}{4\pi^2} \frac{Q}{V_m} \quad (2.10)$$

Here we have used $c/\omega_0 = (\lambda_0/n)/2\pi$, where λ_0 is the wavelength in vacuum and n is the refractive index of the medium, and $\kappa = \omega_0/Q$, where Q is the quality factor of the cavity. If the emitter has a branching ratio ζ for the transition, then the effective Purcell factor C is given by $C = \zeta C_0$. Additionally, the efficiency β to emit in the mode of the cavity can be written as $\beta = C/(C + 1)$. Hence, sufficiently high C can simultaneously result in higher emission rate and higher collection efficiency in the mode of the cavity.

2.3 Single emitter properties

2.3.1 Emitter saturation, Rabi frequency & linewidth

For all the experiments in this thesis on the emitter-cavity system, we follow a procedure of resonantly exciting the emitter followed by collecting the spontaneously emitted photons. Both the excitation and collection are done by using the fiber mirror of our microcavity which provides direct access to the cavity mode. The behaviour of the emitter can be understood by looking at the evolution of its density matrix elements as given by the optical Bloch equations. For a two level system with eigenstates $|g\rangle$ and $|e\rangle$, the diagonal density matrix elements ρ_{gg} and ρ_{ee} express the probability to occupy the $|g\rangle$ and $|e\rangle$ states respectively, while the off-diagonal elements ρ_{ge} and ρ_{eg} are the coherence between the two levels.

As the main objective of this thesis is to detect a single emitter by collecting the fluorescence from the spontaneous decay of the emitter from $|e\rangle$ to $|g\rangle$, we are mainly interested in the diagonal elements of the density matrix. Considering the steady-state regime of the Bloch equations, these

elements assume the expressions [81, 82]

$$\rho_{ee} = \frac{1}{2} \frac{S}{\left(1 + \frac{\Delta^2}{\Gamma_2^2} + S\right)} \quad (2.11)$$

$$\rho_{gg} = 1 - \rho_{ee}$$

where Δ is the detuning between the emitter and field, and S is the saturation parameter defined as

$$S = \frac{\Omega^2}{\Gamma_1 \Gamma_2} \quad (2.12)$$

where Ω is the Rabi frequency, Γ_1 is the rate of decay of population from $|e\rangle$ to $|g\rangle$ and Γ_2 is the rate of decoherence between the two states. We can see that ρ_{ee} as a function of Δ has a Lorentzian shape with a linewidth Γ_{pb} given by

$$\Gamma_{pb} = \Gamma_h \sqrt{1 + S} \quad (2.13)$$

where Γ_h is the linewidth of the emitter at zero power given as $\Gamma_h = \Gamma_2/\pi$. As the value of Γ_{pb} increases with the input power, we will refer to it as the power-broadened linewidth.

The Rabi frequency Ω experienced by the emitter is related to the emitter-field coupling parameter g by $\Omega = 2g\sqrt{N_{ph}}$, where N_{ph} is the average intra-cavity photon number. N_{ph} can be calculated as [52, 55]

$$N_{ph} = \frac{4P_{in}}{\hbar\omega\kappa} \quad (2.14)$$

where P_{in} is the power that is put into the cavity, ω is the angular frequency of the photons and κ is the angular decay rate of the cavity.

2.3.2 Statistics of light from single emitters

In addition to understanding the behaviour of a single emitter based on its saturation and power broadened linewidth, it is important to also study the statistics of the emitted photons. In particular, we can measure the second-order correlation function $g^{(2)}$ of the emitted photons which is defined as

[80]

$$g^{(2)}(t, \tau) = \frac{\langle \hat{a}_1^\dagger(t) \hat{a}_2^\dagger(t + \tau) \hat{a}_2(t + \tau) \hat{a}_1(t) \rangle}{\langle \hat{a}_1^\dagger(t) \hat{a}_1(t) \rangle \langle \hat{a}_2^\dagger(t + \tau) \hat{a}_2(t + \tau) \rangle} \quad (2.15)$$

where (1, 2) are the modes between which the second-order correlation is being computed for, and \hat{a}_i^\dagger and \hat{a}_i are the creation and annihilation operators, respectively, for the light in mode i . Generally, $g^{(2)}$ doesn't change as a function of the absolute time t , and is hence written only in terms of the relative time delay τ between the two modes. One can show that for coherent light $g^{(2)}(0) = 1$, while for a photon number state $|n\rangle$, $g^{(2)}(0) = (n - 1)/n$. Hence, for a single photon state $g^{(2)}(0) = 0$. A measurement of the $g^{(2)}(0)$ value can hence be useful to classify the input photon state.

To measure the value of $g^{(2)}(0)$, one can perform a Hanbury Brown-Twiss (HBT) experiment. It involves sending the photon state through a 50:50 beam-splitter followed by detecting the photons in each of the output modes. The detectors are single photon counters that record the arrival time of each photon. Eq. 2.15 can then be rewritten as

$$g^{(2)}(0) = \frac{\langle N_{1,2}(t) \rangle}{\langle N_1(t) \rangle \langle N_2(t) \rangle} \quad (2.16)$$

where N_i is the counts detected in mode i and $N_{1,2}$ is the number of coincidences between mode 1 and 2. In practice, the number of counts in each mode are recorded in finite time-intervals. Hence, the numerator is proportional to the probability to record a coincidence between modes 1 and 2 within the set time-interval while the denominator is proportional to the product of the individual probabilities to detect a photon in mode 1 and mode 2, respectively, within the time-interval.

2.4 Cavity parameters

2.4.1 Mode of a cavity

Optical cavities can confine light at specific frequencies via interference of the circulating light. They typically consist of two spherical mirrors

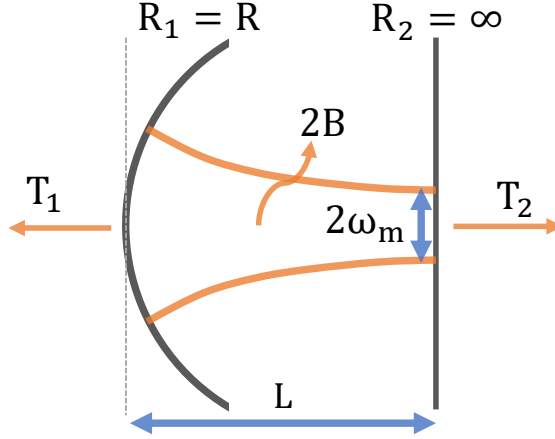


Figure 2.1: Plano-concave cavity with radii of curvatures $R_1 = R$, $R_2 = \infty$, length L .

which have to be placed in specific geometric configurations to be stable. Following a ray-tracing approach such as in [83], we see that for a cavity formed by spherical mirrors with radii of curvatures R_1 and R_2 and length L , the cavity is considered to be in the stable regime if it satisfies

$$0 \leq b_1 b_2 \leq 1 \quad (2.17)$$

where $b_1 = 1 + (L/R_1)$ and $b_2 = 1 + (L/R_2)$. In this thesis, we make use of a plano-concave cavity formed by a concave surface with radius of curvature $R_1 = R$ on one side and a planar mirror ($R_2 = \infty$) on the other side (see Fig. 2.1). The stability criteria then simplifies to $0 \leq L/R \leq 1$.

Gaussian modes whose curvature at the position of either of the mirrors matches the curvature of the respective mirror are supported by the cavity. A general solution similar to Eq. 2.17 for the Gaussian modes supported by a cavity can be derived [83]. For a plano-concave cavity such as the one used in this thesis with radius of curvature R for the concave mirror

and length L , the mode-waist ω_m of the Gaussian mode supported by the cavity for short lengths L simplifies to [63]

$$\omega_m \approx \sqrt{\frac{\lambda}{\pi}} (LR)^{1/4} \quad (2.18)$$

where λ is the wavelength of light. The mode is centred on the planar mirror and its curvature on the concave mirror matches the curvature R of the mirror (see Fig. 2.1). The mode volume V_m of the cavity is given by

$$V_m = \frac{\pi}{4} \omega_m^2 L = \frac{\lambda}{4} \sqrt{RL^3} \quad (2.19)$$

The quality factor Q of a cavity is related to its finesse F as $Q = F(2L/\lambda)$. Rewriting the Purcell factor given in Eq. 2.10 in terms of the mode-volume of the plano-concave cavity and the finesse we get

$$C_0 = \frac{6\lambda}{\pi^2} \frac{F}{\sqrt{RL}} \quad (2.20)$$

Hence, in order to achieve a high Purcell factor we need to have a high F and simultaneously reduce R and L .

2.4.2 Cavity finesse

For a cavity formed by mirrors with transmissivities T_1 and T_2 , and round trip intra-cavity loss $2B$, the finesse F is given by [63]

$$F = \frac{2\pi}{(T_1 + T_2 + 2B)} \quad (2.21)$$

The total transmission through the cavity is given by

$$T_c = \frac{4T_1T_2}{(T_1 + T_2 + 2B)^2} \quad (2.22)$$

Note that unity transmission is only achieved when $T_1 = T_2$ and $B = 0$. Given that a photon is generated inside the cavity, the efficiency η_{esc} with

which it will escape the cavity through the mirror with transmissivity T_1 is given by

$$\eta_{ecs} = \frac{T_1}{(T_1 + T_2 + 2B)} \quad (2.23)$$

Hence to maximise the escape efficiency of the photon through the mirror with transmissivity T_1 , we need to have $T_1 \gg T_2 + 2B$. In our case, the fiber mirror is used for both excitation and collection of photons, while the transmission through the planar mirror is utilized for monitoring the cavity. The main contribution to intra-cavity loss comes from scattering loss due to the nanoparticle. The values of T_1 and T_2 hence need to be chosen so as to simultaneously maximize the Purcell enhancement and the out-coupling through the fiber mirror. Sec. 3.2.1 details the parameters that were chosen for this thesis.

Chapter 3

Experimental setup

Single rare-earth ions are a very promising platform for quantum networking. Due to their extremely small size, rare-earth ion doped nanoparticles enable integration into microcavities to reach strong Purcell enhancement. In addition, they also provide the confinement required to isolate and individually manipulate spatially close-by single ion qubits. The objective of this thesis is to investigate erbium-doped Y_2O_3 nanoparticles coupled to a fiber-based microcavity. The ${}^4I_{15/2} - {}^4I_{13/2}$ transition in erbium lies in the telecom band and can be integrated into existing fiber networks easily. Fiber-based microcavities can achieve high Purcell factors and are ideally suited to be coupled to nanoparticles due to their tuning capabilities.

This chapter describes our experimental setup, including all methods and procedures. We begin in Sec. 3.1 with the $\text{Er}^{3+}:\text{Y}_2\text{O}_3$ nanoparticles, which includes details about material synthesis, scattering cross section and the total number of erbium ions present. In Sec. 3.2, we describe details about our fiber based micro-cavity as well as the expected maximum Purcell factor for $\text{Er}^{3+}:\text{Y}_2\text{O}_3$ coupled to these cavities. It also includes details about the expected count-rate from a single erbium ion with realistic experimental parameters.

To couple the $\text{Er}^{3+}:\text{Y}_2\text{O}_3$ nanoparticles to the fiber microcavity, we spin-coat the nanoparticles on the planar mirror and position the fiber

mirror at the location of a suitable nanoparticle. As spin-coating randomly distributes the nanoparticles on the surface of the planar mirror, we need some tuning range in order to be able to locate a suitable nanoparticle. In addition, the nanoparticles need to be cooled to cryogenic temperatures to achieve good coherence properties. Since the closed cycle cryostat used in this thesis adds mechanical noise, our setup needs to be decoupled from it in order to stabilize a high finesse cavity in that environment. Since no commercial system was found that could simultaneously achieve both the desired tuning range and mechanical stability, we built a custom so-called ‘nano-positioner’ system to enable the operation of our setup in a cryogenic environment. Two iterations of the nano-positioner were built during the duration of this thesis, and all details regarding them including the achieved stability of the microcavity, the total fine and coarse tuning range, and the final temperatures reached for the nanoparticles are described in detail in Sec. 3.3.

3.1 Erbium doped nanoparticles

3.1.1 Material synthesis

The $\text{Er}^{3+}:\text{Y}_2\text{O}_3$ nanoparticles that were investigated in this study were synthesized by Dr. Shuping Liu, Dr. Diana Serrano and Dr. Alban Ferrier in the group of Dr. Philippe Goldner at ChimieParisTech, Paris. We give here a short description of the fabrication process. The synthesis route is based on homogeneous precipitation followed by high-temperature annealing [77, 84]. It starts by mixing an appropriate amount of urea in an aqueous solution of erbium and yttrium nitrates, which precipitates Er^{3+} doped yttrium carbonate nanoparticles. The size of the nanoparticles can be controlled by the amount of urea added to the solution, where higher concentration of urea results in smaller nanoparticles. Similarly, the concentration of erbium doping can be controlled by varying the concentration of erbium nitrate used in the initial solution. To obtain $\text{Er}^{3+}:\text{Y}_2\text{O}_3$ nanoparticles, the erbium doped yttrium basic carbonates were annealed at a temperature of 1200 °C. The average diameter of the resulting $\text{Er}^{3+}:\text{Y}_2\text{O}_3$ nanoparti-

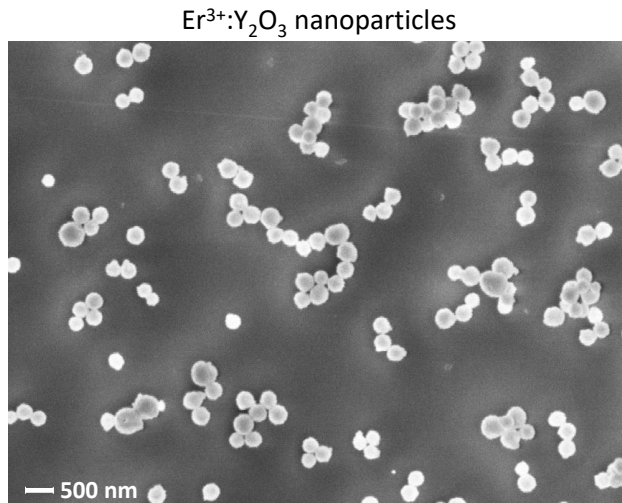


Figure 3.1: SEM image of the synthesized 200 ppm $\text{Er}^{3+}:\text{Y}_2\text{O}_3$ nanoparticles with an average diameter of 140 nm and an average crystallite domain size of ≈ 80 nm as determined by X-ray diffraction.

cles was 140 nm as assessed using a scanning electron microscope (SEM), with a Er^{3+} doping concentration of 200 ppm (see Fig. 3.1). Annealing also changes the morphology of the resulting nanoparticles. The crystalline phase was determined by X-ray diffraction (XRD) to be body-centered cubic (BCC) with Ia-3 space group. The $\text{Er}^{3+}:\text{Y}_2\text{O}_3$ nanoparticles appear poly-crystalline, with a crystallite domain size of ≈ 80 nm. The crystallite size can be increased by annealing at a higher temperature. However, this can lead to an increase in the average size of the nanoparticles, which can be detrimental due to an increase in scattering loss that will make it challenging to integrate them into microcavities (see Sec. 3.1.3 below).

3.1.2 Number of erbium ions

In this section we estimate the total number of ions that are present in a nanoparticle with a diameter of 140 nm. For Y_2O_3 , molar mass = 225.8 g/mole, and density = 5.01 g/cm³ [85]. The atomic weight of yttrium = 88.9 u , oxygen = 16 u , where $u = 1.66 \times 10^{-24}$ g is the atomic mass unit. Using this information, we can estimate that the density of Y_2O_3 unit cells is = 1.34×10^{22} /cm³. We can then estimate that the number of Y_2O_3 units in a sphere with diameter 100 nm = 7×10^6 , and the number of yttrium atoms is = 14×10^6 . Since the doping concentration in our case is based on the number of yttrium atoms that are replaced with erbium, for a doping concentration of 200 ppm we have about 2800 erbium ions in a Y_2O_3 nanoparticle of diameter 100 nm. In our case the average diameter of the Y_2O_3 nanoparticles is 140 nm, in which case the total number of erbium ions is about 7500.

3.1.3 Scattering loss

The scattering loss introduced by a nanoparticle is an important factor to consider when integrating them into microcavities. As discussed in Sec. 2.4.2, low scattering loss results in a higher finesse for the microcavity (and consequently a higher Purcell factor) as well as a higher escape efficiency for the generated photons. The scattering loss B induced by a nanoparticle is related to its scattering cross section σ as [86]

$$B = 4\sigma/\pi w_0^2 \quad (3.1)$$

where w_0 is the mode waist of the light beam at the position of the particle. The scattering cross section σ can be calculated as

$$\sigma = \left(\frac{2\pi}{\lambda}\right)^4 \frac{\alpha^2}{6\pi} \quad (3.2)$$

where λ is the wavelength of light and α is the polarizability of the nanoparticle. When the nanoparticles are placed on a dielectric surface (the surface

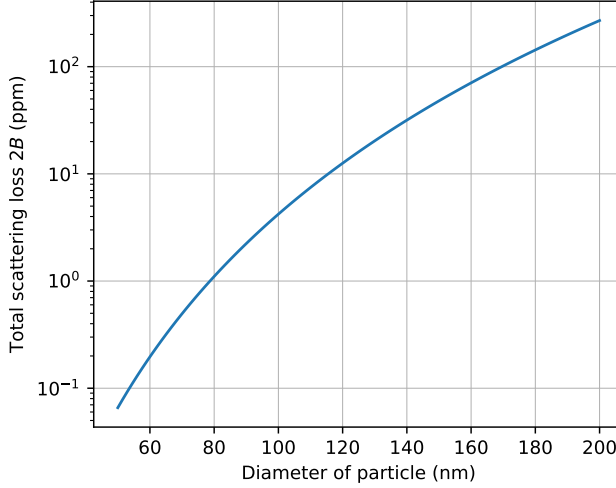


Figure 3.2: Total scattering loss $2B$ induced by a nanoparticle inside a cavity as a function of its diameter. To estimate the loss, we set $\lambda = 1535$ nm, $\epsilon_1 = 1$, $\epsilon_2 = 13$, and $\epsilon_3 = 3.9$, and $\omega_0 = 2.4$ μm , which corresponds to a plano-concave cavity with $R = 50$ μm , $L = 3$ μm . For a particle of 140 nm diameter, which is the average size of a nanoparticle used in this thesis, the total scattering loss $2B = 31.7$ ppm.

of a planar mirror in our case) which is then placed in vacuum, then α is given by [87]

$$\alpha = \frac{\epsilon_1(\epsilon_3 - \epsilon_1)V}{\epsilon_1 + L(\epsilon_3 - \epsilon_1)} \quad (3.3)$$

where ϵ_1 , ϵ_2 and ϵ_3 are, respectively, the dielectric constants of vacuum, the nanoparticle, and the dielectric surface, $V = 4/3\pi r^3$ is the volume of the nanoparticle, and L is the depolarization factor given by

$$L = \frac{1}{3} \left(1 - \frac{1}{8} \frac{\epsilon_2 - \epsilon_1}{\epsilon_2 + \epsilon_1} \right) \quad (3.4)$$

For the $\text{Er}^{3+}:\text{Y}_2\text{O}_3$ nanoparticles spin coated on a silica substrate as in this thesis, we have $\epsilon_1 = 1$, $\epsilon_2 = 13$ [88], and $\epsilon_3 = 3.9$ [89]. In Fig. 3.2, we estimate the expected total round-trip scattering loss $2B$ as a function of diameter of the particle by setting $\lambda = 1535$ nm and $\omega_0 = 2.4$ μm . The value of ω_0 corresponds to a plano-concave cavity with $R = 50$ μm , $L = 3$ μm , which are typical values for fiber cavities that will be used in this thesis. For a particle of 140 nm diameter, which is the average size of a nanoparticle used in this thesis, the total scattering loss $2B = 31.7$ ppm. For integration into microcavities, the total scattering loss $2B$ has to be kept as low as possible (see Sec. 2.4.2), which implies that the diameter of the particle has to be kept small. However, a smaller size typically comes with a degradation in the optical coherence time T_2 [58], which would make it more challenging to produce indistinguishable photons from the emitters (see Sec. 1.2). The average diameter of 140 nm was hence chosen as a good compromise between cavity performance and good coherence properties [60, 90].

3.1.4 Preparing nanoparticles on planar mirror

The nanoparticles can be integrated into our microcavity by simply spin-coating them onto the planar mirror and then utilizing the fiber mirror to locate and couple to a desirable nanoparticle (see Sec. 3.5). In this section, we provide a description of the procedure that was followed to spin-coat the nanoparticles on the planar mirror. The procedure was carried out at ICFO by the author of this thesis with the help of Dr. Bernardo Casabone.

The nanoparticles have an average size of 140 nm but there is a considerable spread in the size of individual nanoparticles. Additionally, there is the possibility that small nanoparticles agglomerate to form larger particles. As the scattering loss $2B$ scales very strongly with the diameter (see Fig. 3.2), it is desirable to only spin-coat nanoparticles with the right size onto the planar mirror. We hence follow a two-step process to mitigate both these issues. First, we make use of an ultrasonic bath in which the nanoparticles can be placed to break the agglomerated particles into smaller ones. Second, we centrifugate to segregate them according to their

size and then pick the ones with the appropriate size to spin-coat.

The procedure begins by preparing a solution with 1 mg of $\text{Er}^{3+}:\text{Y}_2\text{O}_3$ nanoparticles in 1 ml of highly pure ethanol ($> 99.99\%$). We then leave this solution for 30 minutes in an ultrasonic bath which delivers 500 W of ultrasonic power at a frequency of 40 kHz. The solution appears milky after the ultrasonic treatment. Post this we centrifugate the solution by adapting to our setup the parameters described in [91], which were in turn arrived at by following the procedure described in [92]. After centrifugation at a relative centrifugation force of ≈ 1000 (corresponds to 3000 rotations per minute for our centrifugator) for 1 minute, the solution appears clean at the top with clear sedimentation at the bottom. We estimate that most of the nanoparticles larger than 200 nm should have settled at the bottom of our 1 cm tube, and there should be very few nanoparticles larger than 140 nm roughly half way in the tube.

We then prepare the surface of the mirror for spin coating by treating it to oxygen plasma at high pressure, which makes the surface hydrophilic. 60 μl of the centrifugated sample from around the half-way mark in the tube is then spin-coated onto the surface of the planar mirror by spinning the mirror at 2500 rpm, which results in a good distribution of nanoparticles with diameters around 140 nm (see Fig. 3.17).

3.2 Fiber microcavity

The microcavity used in this thesis is composed of a concave fiber-mirror on one side and a bulk planar mirror on the other (see Fig. 3.3). The concave surface is fabricated on the tip of a fiber using CO_2 laser ablation. The fabrication was performed by Dr. Bernardo Casabone at LMU (Munich, Germany) in the group of Prof. David Hunger. The fiber is commercially available (AL1300 from IVG Fiber) and is single mode at 1535 nm. The fiber tip is composed of silica which has a strong absorption at 10.6 μm . A CO_2 laser pulse incident on the tip of the fiber is hence absorbed within a few μm resulting in thermal evaporation. It also leaves behind a thin layer of melted silica with low viscosity that produces very smooth surfaces with

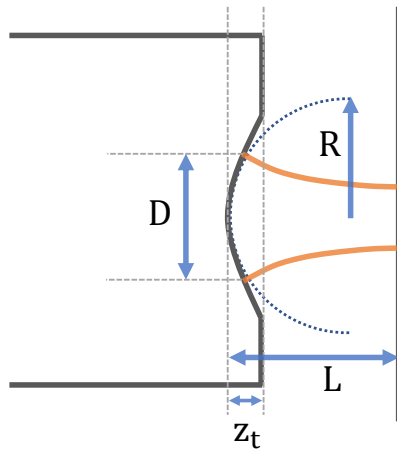


Figure 3.3: Schematic drawing of the tunable fiber-based microcavity. The cavity is formed by the curved tip of a fiber mirror on one side and a planar mirror on the other side. Parameters indicated: R is the radius of curvature of the fiber tip close to the centre of the profile, z_t is the profile depth, D is the structure diameter, and L is the total length of the cavity.

very low scattering [93]. The concave surfaces are spherical close to the centre of the profile. The structure diameter D estimates the part of the concave profile that is spherical and hence useful. The radius of curvature R of the profile and its depth z_t can be controlled by varying laser parameters such as peak power, beam waist and the duration and number of pulses used for ablation. Note that the structural depth z_t puts a lower limit on the cavity length L which is achieved when the two mirrors are physically touching. D , R and z_t are related by [63]

$$z_t \approx \frac{D^2}{8R} \quad (3.5)$$

As discussed in Sec. 2.4.1, for a plano-concave cavity with radius of curvature R and length L , the mode-waist ω_m of the Gaussian mode supported

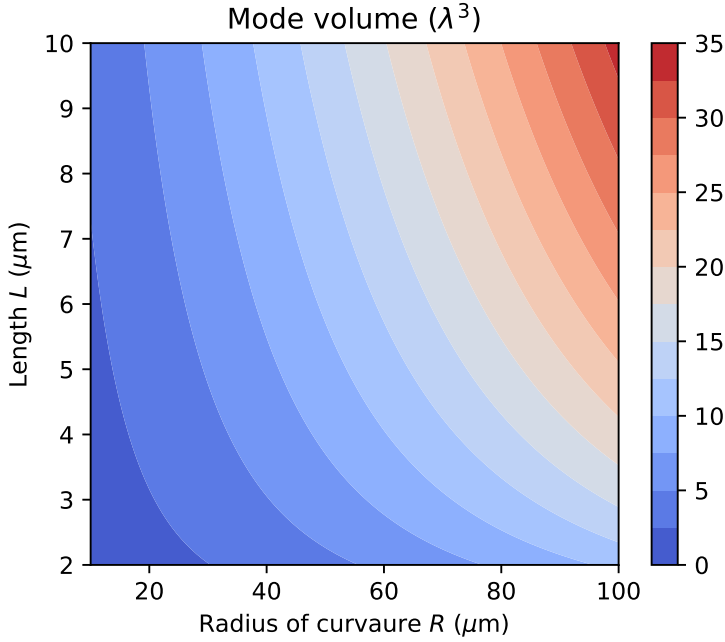


Figure 3.4: Mode volume V_m in units of λ^3 for a range of radius of curvatures R and lengths L .

by the cavity for short lengths L simplifies to [63]

$$\omega_m \approx \sqrt{\frac{\lambda}{\pi}} (LR)^{1/4} \quad (3.6)$$

where λ is the wavelength of light and the mode is centred on the planar mirror. The mode volume V_m of the cavity in this regime is given by

$$V_m = \frac{\pi}{4} \omega_m^2 L = \frac{\lambda}{4} \sqrt{RL^3} \quad (3.7)$$

Hence, in order to achieve a small mode-volume as required to obtain high Purcell enhancement, one needs to simultaneously reduce R and L .

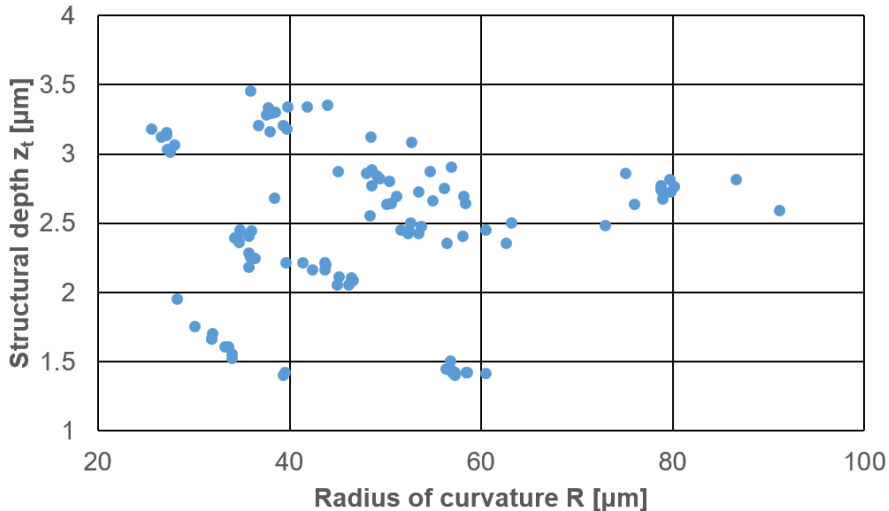


Figure 3.5: Overview of fibers with different radius of curvatures R and structural depths z_t that were fabricated for the purpose of this thesis.

Laser ablation techniques can achieve concave profiles down to $R \approx 10 \mu\text{m}$ with structural depths $z_t \approx 1 \mu\text{m}$. In addition, due to the small size of fiber tips ($\approx 125 \mu\text{m}$) they can be brought much closer to the planar mirror even with small misalignments in the angle. These factors together enable fiber based microcavities to achieve small mode volumes. Mode volume V_m for a range of radius of curvatures R and lengths L is shown in Fig. 3.4. V_m of the order of few λ^3 at $\lambda \approx 1.5 \mu\text{m}$ is hence feasible for realistic values of R and L . For instance, for a cavity with $R = 50 \mu\text{m}$ and $L = 3 \mu\text{m}$, which are typical values for cavities used in this thesis, we obtain $V_m \approx 4\lambda^3$.

As will be discussed in more detail below in Sec. 3.2.3, mode-matching is more challenging with small R . Hence, fiber tips with a range of radius of curvatures R and structural depths z_t were fabricated for the purpose of this thesis to give some flexibility, as shown in Fig. 3.5.

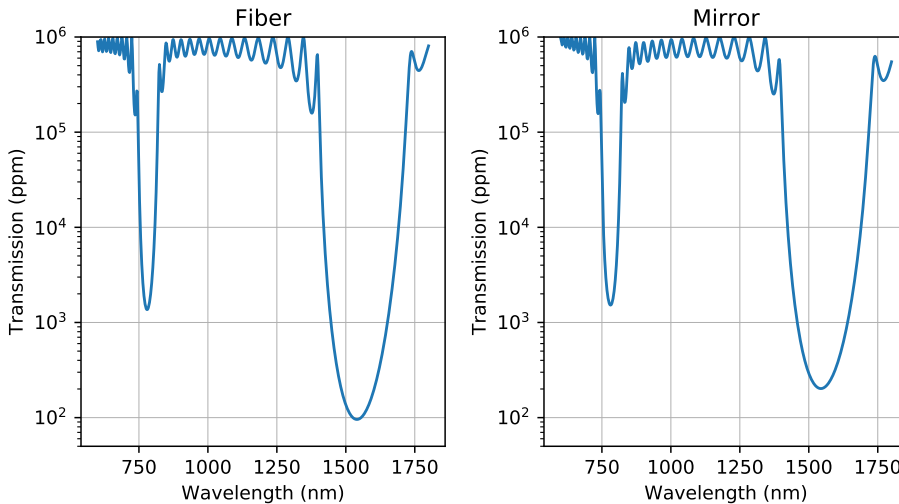


Figure 3.6: Transmissivity in ppm of fiber (left) and planar mirror (right) as a function of wavelength. Transmission for the fiber mirror is ≈ 1400 ppm at 790 nm and ≈ 100 ppm at 1535 nm, while for the planar mirror is ≈ 1700 ppm at 790 nm and ≈ 200 ppm at 1535 nm.

3.2.1 Dielectric coating

In order to obtain high Purcell enhancement, we need to achieve a high finesse F for the microcavity. However, increasing the finesse arbitrarily would be undesirable for the following reasons. First, if F is increased while keeping the total scattering loss $2B$ of the nanoparticle constant, then the escape efficiency of the generated photons would decrease (see Sec. 2.4.2 and Sec. 3.2.4). Second, increasing finesse much beyond the stability of the cavity would not result in any improvement in the effective Purcell enhancement. To illustrate this, let us consider a cavity with finesse F . The FWHM of the cavity resonance is given by $\lambda/(2F)$. If the fluctuation in the cavity length is much greater than the FWHM, then the cavity would be mostly off-resonant with respect to the set resonance, which reduces the

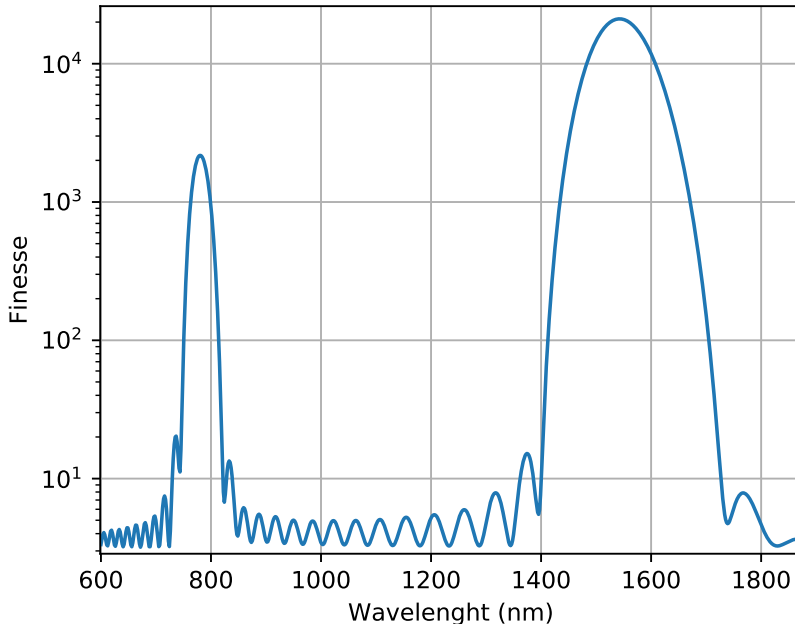


Figure 3.7: Finesse of the cavity as a function of wavelength. Finesse at 790 nm is $\approx 2,100$ and at 1535 nm is $\approx 21,000$.

achieved Purcell factor. For a more detailed discussion, see Sec. A.1.

Hence, we target a finesse of $\approx 21,000$ which gives high out-coupling efficiency with our nanoparticles (see Sec. 3.2.3) and is at the limit set by our cavity stability (see Sec. 3.4). In addition, we will use a second resonance at 790 nm with a finesse of $\approx 2,100$ to stabilize the length of the cavity (see Sec. 3.4 for more details). The coating was designed such that for every 1535 nm mode, there is a close by 790 nm mode for cavity lengths in the 2 to 20 μm range.

The dielectric coating on the fiber and planar mirror surfaces consist of alternating layers of SiO_2 and Ta_2O_5 to form a distributed Bragg reflector. The coating was custom designed and fabricated commercially by

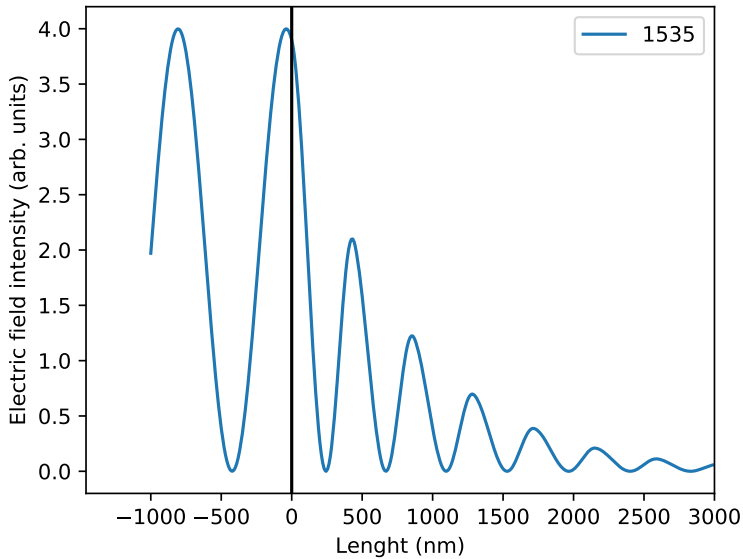


Figure 3.8: Electric field intensity as a function of distance from the surface of the planar mirror. Positive length represents distance into the mirror, while negative length represents distance away from the surface of the mirror. Black line represents the surface of the mirror. The closest electric field intensity maximum is at a distance of 50 nm away from the surface of the planar mirror.

Laseroptik GmbH. If the transmissivities of the fiber mirror and planar mirror are T_f and T_m respectively, then the finesse of the cavity is given by $F = 2\pi/(T_f + T_m)$. The transmissivities at a certain wavelength are chosen so as to result in the desired finesse at that wavelength. Fig. 3.6 shows the transmissivities in ppm of the fiber mirror (left) and the planar mirror (right) as a function of wavelength. The resulting finesse is plotted in Fig. 3.7 as a function of wavelength.

Two other factors have to be taken into consideration while designing the dielectric coating at 1535 nm. First, the coating has to be done so that

the resulting standing wave of the cavity mode at 1535 nm has a maximum at the position of the emitter to achieve the maximum Purcell factor (see Sec. 2.2). Second, the design needs to minimize the penetration depth (or equivalently the group delay (GD)) of 1535 nm inside the dielectric layers so as to minimize the effective length L of the microcavity. We hence decided to have slightly different coatings on the fiber and planar mirrors. The dielectric coating on the fiber was optimized so as to minimize the penetration depth at 1535 nm while achieving transmissivities of ≈ 1400 ppm at 790 nm and ≈ 100 ppm at 1535 nm, as shown on left in Fig. 3.6. The resulting group delay (GD) at 1535 nm is 5.3 fs.

The planar mirror has the same coating as the fiber mirror with an additional layer of SiO₂ with a thickness of 240 nm deposited on top. The thickness of this layer was chosen so as to result in a maximum for the standing wave at a position 50 nm above the surface of the planar mirror (see Fig. 3.8). For our nanoparticles with 140 nm diameter, this would result in a significant number of ions in the nanoparticle sitting at the maximum of the electric field. This additional layer slightly increases the transmissivity of the planar mirror to ≈ 1700 ppm at 790 nm and ≈ 200 ppm at 1535 nm, as shown on the right in Fig. 3.6. This results in the microcavity having a finesse of 2,100 at 790 nm and 21,000 at 1535 nm. The GD is slightly increased to 5.5 fs. Hence, the total GD due to the dielectric layers on both the fiber and the mirror is ≈ 10.8 fs, which translates to a total penetration depth of $d_p \approx 1620$ nm. This implies that for a physical distance of d_0 between the fiber mirror and the planar mirror, the actual length of the resulting cavity is given by $d = d_0 + d_p$.

Since we utilize the fiber mirror for collection of emitted photons, having a higher transmissivity on the planar mirror at 1535 nm compared with the fiber mirror reduces the overall escape efficiency η_{esc} of the photons through the fiber mirror (see Sec. 3.2.4). Hence, for a second set of experiments in Ch. 7 that report on the detection of a single erbium ion, a planar mirror with a transmissivity lower than that of the fiber mirror was utilized. This results in a higher overall finesse for the cavity at 1535 nm, as well as a higher escape efficiency for the emitted photons, which should result in better sensitivity to single ion detection. Sec. 3.2.5 discusses details about

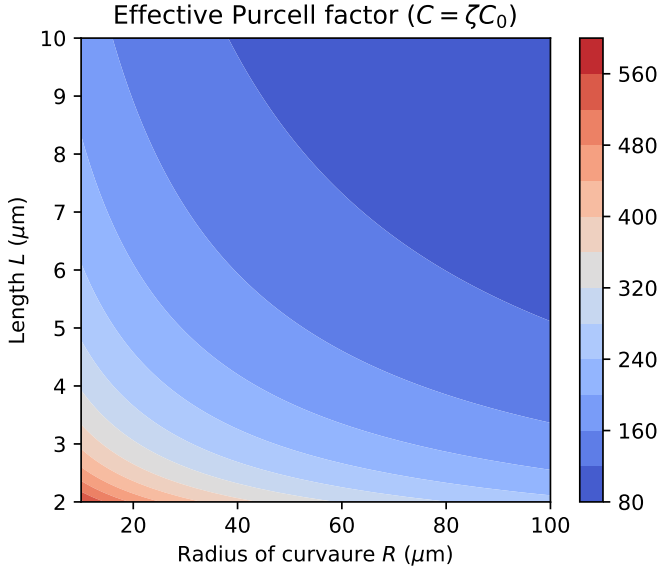


Figure 3.9: Effective Purcell factor C for $\text{Er}^{3+}:\text{Y}_2\text{O}_3$ with $F = 19,000$ for a range of radius of curvatures R and lengths L .

this second generation planar mirror.

3.2.2 Purcell factor

The Purcell factor C for an emitter in a plano concave cavity with radius of curvature R and length L in the regime of small L is given by (see Sec. 2.2)

$$C = \zeta \frac{6\lambda}{\pi^2} \frac{F}{\sqrt{RL}} \quad (3.8)$$

where F is the finesse and λ is the wavelength, and ζ is the branching ratio of the relevant transition of the emitter. For our $\text{Er}^{3+}:\text{Y}_2\text{O}_3$ nanoparticles, $\lambda = 1535$ nm and $\zeta = 0.13$ (see Sec. 4.3.1). If we couple to a nanoparticle with average diameter of 140 nm, which introduces total intra-cavity losses

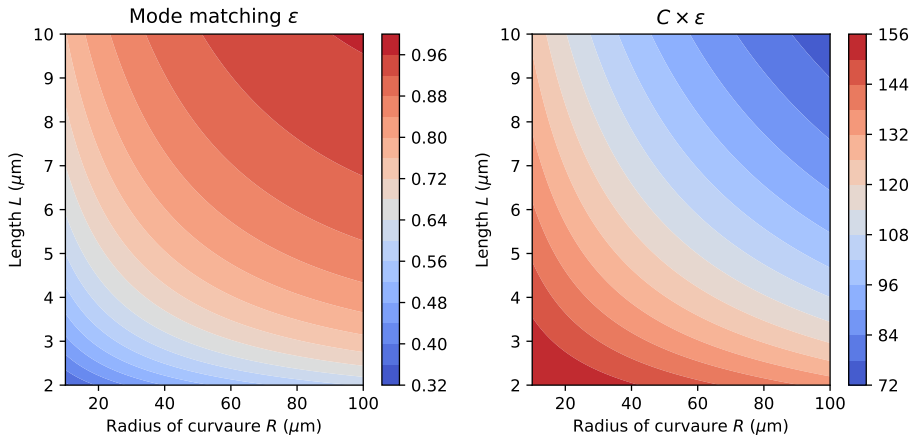


Figure 3.10: Mode matching ϵ between the fiber and cavity mode (left) and the product $C \times \epsilon$ (right) as a function of radius of curvatures R and lengths L .

of 31.7 ppm, then F reduces to 19,000. The effective Purcell factor C we can achieve for a range of radius of curvatures R and lengths L is shown in Fig. 3.9. For instance, for a cavity with length $L = 3 \mu\text{m}$ and radius of curvature $50 \mu\text{m}$, we expect an effective Purcell factor $C \approx 200$. The emission efficiency into the cavity mode defined as $\beta = C/(C + 1)$ corresponds to 99.5 %. Hence, the emitter would almost entirely emit into the mode of the cavity.

3.2.3 Mode matching

One of the main advantages of having a fiber-based microcavity is that the fiber gives direct access to the mode of the cavity, which makes the experiment extremely convenient. The fiber can hence be used to resonantly excite erbium ions as well as to collect the emitted photons. It is hence important to achieve good mode-matching between the mode of the fiber and that of the cavity. For two Gaussian modes with mode-waists ω_f

and ω_m and separated by length L , as is the case for our plano-concave microcavity (see Fig. 3.11), the mode matching efficiency ϵ is given by [63]

$$\epsilon = \frac{4}{\left(\frac{\omega_f}{\omega_m} + \frac{\omega_m}{\omega_f}\right)^2 + \frac{L^2}{Z_f Z_m}} \quad (3.9)$$

where Z_f and Z_m are Rayleigh lengths given by $Z_f = \pi\omega_f^2/\lambda$ and $Z_m = \pi\omega_m^2/\lambda$ with λ as the wavelength. Note that imperfections, such as centering error between the core of the fiber mode and that of the cavity mode as well as misalignments between the two modes, are ignored to arrive at this equation. We utilize a commercial fiber (AL1300 from IVG Fiber) which has a specified mode waist of $\omega_f = 4.5 \mu\text{m}$. The mode-waist ω_m of the cavity mode depends on the radius of curvature R and the length L of the microcavity (see Sec. 3.2). The power transfer coefficient ϵ between the fiber and cavity modes for a range of R and L is plotted on left in Fig. 3.10. For a cavity with $R = 50 \mu\text{m}$ and $L = 3 \mu\text{m}$, we get $\epsilon = 0.70$. High mode-matching is achieved for high R and L . This is however contrary to the Purcell factor which is maximized by minimizing R and L (see Fig. 3.9). Hence, if the objective is to detect a single ion, then we want to maximize the obtained count-rate for the emitted photons, which we discuss in the following section.

3.2.4 Expected single-ion count rate

If the fiber is used to collect the emitted photons and assuming no other channel of loss, then the expected count-rate in the fiber γ_f from the emitter for a given R and L is $\gamma_f \propto C \times \epsilon$ for $C \gg 1$. The product $C \times \epsilon$ for a range of R and L is shown on the right in Fig. 3.10. For a cavity with $R = 50 \mu\text{m}$ and $L = 3 \mu\text{m}$, we get $C \times \epsilon = 131$. It can be seen that the best count-rate is expected for cavities with small R and L even though the mode-matching gets worse in those cases, as the corresponding increase in the Purcell factor more than compensates for it. Note however that working with larger R and L is not as bad as it seems from Fig. 3.9, as the increased mode-matching now partially compensates for the smaller Purcell factor.

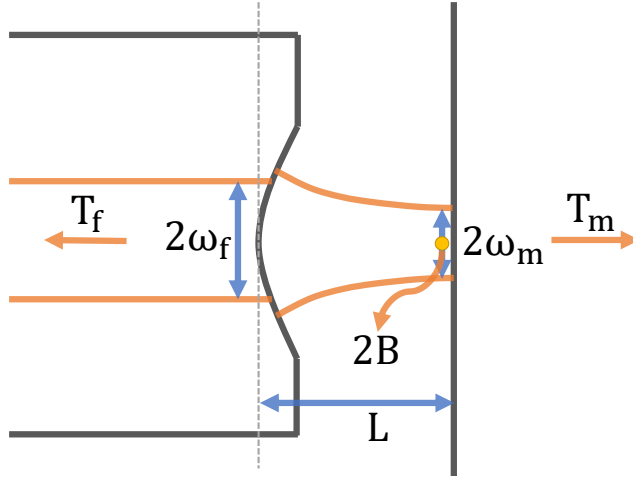


Figure 3.11: Relevant parameters of the fiber microcavity to estimate mode-matching and out-coupling efficiency. Parameters indicated: ω_f is the mode-waist of the fiber mode, ω_m is the mode-waist of the cavity mode, L is the length of the cavity, T_f is the total transmission of the fiber-mirror, T_m is the total transmission of the planar-mirror, and $2B$ is the total losses induced by the nanoparticle (yellow circle) inside the cavity (see main text for details on each parameter). The fiber mirror can be moved in 3D, allowing us to set the length of the cavity and locate a nanoparticle inside the cavity (see Sec. 3.5 for more details).

To get a value for the expected count-rate γ_f we need to estimate the escape efficiency η_{esc} of the cavity. For a cavity with transmissivities T_f and T_m for its two mirrors and an intra-cavity loss of $2B$, the efficiency η_{esc} with which a photon generated inside the cavity escapes through the

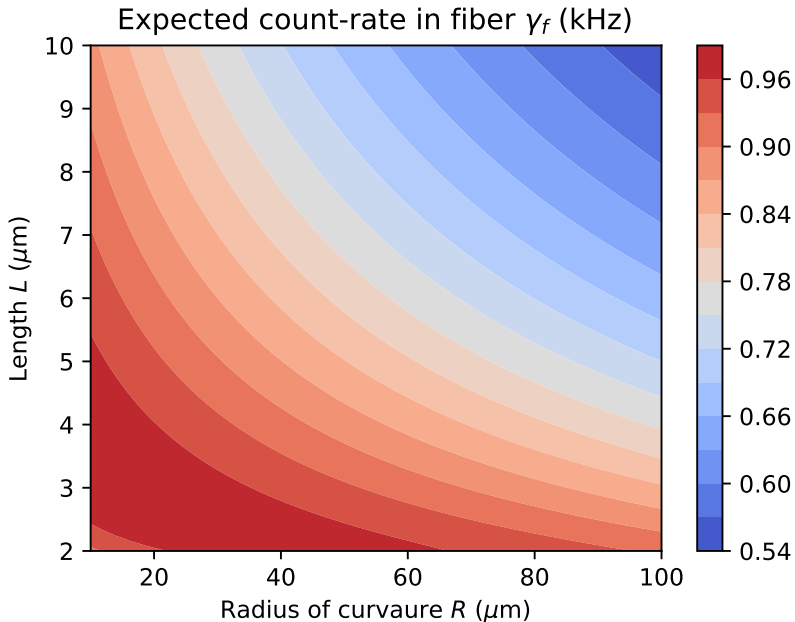


Figure 3.12: Expected count rate γ_f in the fiber as a function of R and L . We have used $T_f = 100$ ppm and $T_m = 200$ ppm. The total round-trip scattering loss for a nanoparticle of diameter 140 nm is also calculated at each R and L .

mirror with transmissivity T_f is given by

$$\eta_{esc} = \frac{T_f}{(T_f + T_m + 2B)} \quad (3.10)$$

The efficiency η_{out} with which a photon generated inside the cavity is collected into the fiber is then given by $\eta_{out} = \eta_{esc} \times \epsilon$. If we excite the emitter to reach a steady state (see Sec. 2.3.1) and detect the emission for a time given by the lifetime of the emitter, then the maximum expected count-rate

in the fiber γ_f approaches the value

$$\gamma_f = \eta_{out} \times C \times \frac{\Gamma_1}{2} \times (1 - 1/e) \quad (3.11)$$

where Γ_1 is the natural emission rate of the emitter in the absence of a cavity, and the factor $(1 - 1/e)$ gives the probability that the emitter decays within its lifetime. For $\text{Er}^{3+}:\text{Y}_2\text{O}_3$ nanoparticles, the natural lifetime of the excited state is $T_1 = 13.4$ ms, giving $\Gamma_1 = 74$ Hz (see Sec. 4.3.2). From Sec. 3.2.1 we have $T_f = 100$ ppm and $T_m = 200$ ppm. The total round-trip scattering loss $2B$ assuming we couple to a nanoparticle with a diameter of 140 nm is also calculated individually at each R and L to estimate η_{esc} . Using these values, the expected count-rate γ_f in the fiber for a range of R and L is shown in Fig. 3.12. For a cavity with $R = 50$ μm and $L = 3$ μm , we estimate $2B = 31.7$ ppm, $\eta_{esc} = 0.30$, $\eta_{out} = 0.21$, and $\gamma_f = 0.92$ kHz. If detected with an efficiency of 3 %, as is the case for the results presented in Ch. 5 with these cavities, this would result in a maximum detected count-rate for a single-ion of 27 Hz.

3.2.5 Lower transmissivity planar mirror

Note that, if we utilize the planar mirror instead of the fiber mirror as our outcoupling mirror, the escape efficiency is $\eta_{esc} = 0.60$, which is higher than that of the fiber mirror. Indeed, in the initial stages of the experiment, we had planned to utilize the planar mirror to collect the emitted photons. But as the design for our setup evolved to include a passive isolation stage for the cavity to minimize mechanical noise from the cryostat, we anticipated that coupling photons escaping from a ‘floating’ cavity into a single-mode fiber, as required for single photon counters at telecom wavelengths, might be challenging. Hence, the fiber mirror became a better choice for outcoupling as the photons generated in the cavity are already fairly mode-matched to it.

Hence, for the set of experiments reported in Ch. 7, a planar mirror with a transmissivity of 30 ppm at 1535 nm was utilized, where the coating is again optimized to result in a maximum for the resulting standing wave

at a position 50 nm above the surface of the planar mirror. The GD for the dielectric stack is almost unchanged at 5.3 fs and the cumulative absorption loss is 7 ppm. The reflectivity at 790 nm is also unchanged at 1400 ppm. This gives a finesse of 2,200 at 790 nm and 44,000 at 1535 nm. If we couple to a nanoparticle with an average diameter of 140 nm, which introduces a total scattering loss of 31.7 ppm, then the finesse reduces to 36,000. For a cavity with this finesse, $L = 3 \mu\text{m}$ and $R = 50 \mu\text{m}$, we expect an effective maximum Purcell factor of $C \approx 400$ for $\text{Er}^{3+}:\text{Y}_2\text{O}_3$, which is almost a factor 2 greater than the one expected with the previous planar mirror.

Using the fiber mirror as the outcoupling mirror, we have $\eta_{esc} = 0.59$. The efficiency with which a photon generated inside the cavity is collected into the fiber is $\eta_{out} = 0.42$. The expected count-rate in the fiber is $\gamma_f \approx 3.8$ kHz. Note that this is almost a factor 4 higher than the one expected with the previous set of planar mirrors. This is due to a combination of factor 2 improvement in the Purcell factor as well as another factor 2 improvement in the outcoupling efficiency. If detected with an efficiency of 35 %, as is the case for the results presented in Ch. 7, this would result in a maximum detected count-rate for a single-ion of 1.3 kHz. Note however that this new cavity puts more stringent demands on the required stability of the cavity as well as the size of the nanoparticle being coupled to.

3.2.6 Estimating cavity-emitter parameters

In this section we try to estimate all the relevant experimental parameters for $\text{Er}^{3+}:\text{Y}_2\text{O}_3$ nanoparticles coupled to a plano-concave microcavity, such as the emitter-field coupling rate g , Rabi frequency Ω and saturation parameter S that were detailed in Sec. 2.3.1. To do so, we will use realistic parameters for our emitter and cavity. All the emitter properties used here are measured in Ch. 4.

The dipole moment μ_{eg} of Er^{3+} for the ${}^4I_{15/2} - {}^4I_{13/2}$ transition at 1535 nm in $\text{Er}^{3+}:\text{Y}_2\text{SiO}_5$ is reported in [94] as 2.07×10^{-32} C-m. Using $T_1 = 13.68$ ms as measured in Sec. 4.3.2, we can estimate that $\mu_{eg} = 2.27 \times 10^{-32}$ C-m for $\text{Er}^{3+}:\text{Y}_2\text{O}_3$. The branching ratio for the transition is measured to be $\zeta = 0.13$ in Sec. 4.3.1. In Sec. 4.3.3, we measure the

rate of de-coherence between the two states to be $\Gamma_2 = 380$ kHz in the best case. The microcavity considered is one with $R = 50 \mu\text{m}$ and $L = 3 \mu\text{m}$ and a finesse of $F = 20,000$, which are typical values of the cavities we make use of in the experiment (see Sec. 3.2). As coupling to the cavity will result in Purcell enhancement of the emission, we need to correct the value of Γ_1 by this factor. The expected Purcell factor for the considered cavity is $C \approx 200$ in the ideal case, which gives $\Gamma_1 = 15.2$ kHz. All values are computed for a coupled power of 1 nW into the cavity.

When the emitter is at the maximum of the cavity electric field energy density and its dipole moment vector is perfectly aligned with that of cavity electric field vector, the emitter-field coupling rate g is given as

$$g = \frac{\mu_{eg}}{\hbar} \sqrt{\frac{\hbar\omega}{2\epsilon_0 V_m}} \quad (3.12)$$

where ϵ_0 is the vacuum permittivity and V_m is the volume of the cavity mode. Using the mode-volume V_m of the cavity used in this case ($\approx 4\lambda^3$ at $\lambda = 1535$ nm), we can estimate $g = 2\pi \times 0.78$ MHz. Note that this is the maximum possible value of g and any experimental imperfections will only lower it.

For the considered cavity, we have $\kappa = 2\pi \times 2.49$ GHz. If the power coupled into the cavity at 1535 nm ($\omega = 2\pi \times 195$ THz) is 1 nW, then the mean number of intra-cavity photons N_{ph} can be calculated as

$$N_{ph} = \frac{4P_{in}}{\hbar\omega\kappa} \quad (3.13)$$

which gives $N_{ph} \approx 2$ photons. The Rabi frequency, which is given as $\Omega = 2g\sqrt{N_{ph}}$, is $\Omega = 2\pi \times 2.19$ MHz. The saturation parameter is calculated to be $S = 138$ for these parameters. The power broadened linewidth Γ_{pb} can be written as

$$\Gamma_{pb} = \Gamma_h \sqrt{1 + S} \quad (3.14)$$

where Γ_h is the linewidth of the emitter at zero power given by $\Gamma_h = 1/(\pi T_2)$. In our case, we have measured $\Gamma_2 = 380$ kHz at a temperature of 3 K. With $S = 829$ at input power of 1 nW, we have $\Gamma_{pb} = 52$ MHz. The

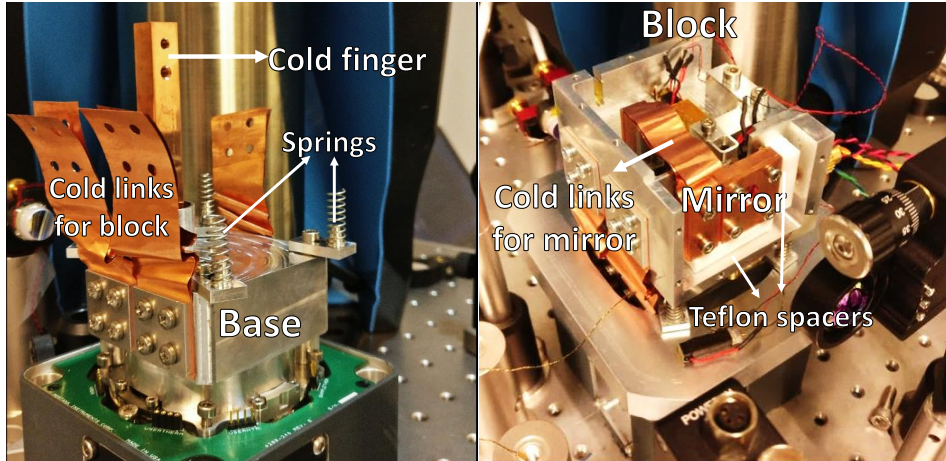


Figure 3.13: Picture of the second iteration of the nano-positioner indicating all the important components. (left) Base, which is in contact with Stage-1 of the cryostat, cold-finger, which is in contact with the sample platform, $50\ \mu\text{m}$ thin copper cold links for the block, and springs on which the block will rest. (right) Block, resting on the base via springs, and already in thermal contact with base via cold links, mirror assembled on the block, which is thermally isolated from block via Teflon spacers but in thermal contact with the cold finger via $25\ \mu\text{m}$ thin copper cold links.

probability to be in the excited state ρ_{ee} is given as $S/(2S + 2)$. Hence, at $S = 829$, we have $\rho_{ee} \approx 0.5$, which is the maximum steady state value.

3.3 Nano-positioner

To couple the $\text{Er}^{3+}:\text{Y}_2\text{O}_3$ nanoparticles to the fiber microcavity, we spin-coat the nanoparticles on the planar mirror and position the fiber mirror at the location of a suitable nanoparticle. As spin-coating randomly dis-

tributes the nanoparticles on the surface of the planar mirror, we need some tuning range in order to be able to locate a suitable nanoparticle. In addition, the nanoparticles need to be cooled to cryogenic temperatures to achieve good coherence properties. Even though the cryostat we use in this thesis (Montana Instruments Cryostation s50) has a passive vibration isolation stage, the residual noise on the platform where the setup is mounted is too high to stabilize a high finesse cavity. Since no commercial system was found that could simultaneously achieve both the desired tuning range and mechanical stability, we built a custom so-called ‘nano-positioner’ system to enable the operation of our setup in a cryogenic environment. The stage was originally designed at LMU (Munich, Germany) by Dr. Thomas Hümmer in the group of Prof. David Hunger (now in the process of commercialization by Qlibri GmbH) and we improved on several aspects of the design. This section describes in detail the two iterations of the nano-positioner that were built during the duration of this thesis.

The nano-positioning system needs to satisfy three requirements to enable the operation of our setup in a cryogenic environment. First, it needs to passively isolate our microcavity from the noisy environment of the cryostat so that it could be actively stabilized. Second, as our $\text{Er}^{3+}:\text{Y}_2\text{O}_3$ nanoparticles are not deterministically placed inside the microcavity, it needs to provide for some tunability so that we can search for and couple to a suitable nanoparticle. Finally, it needs to cool the nanoparticles to cryogenic temperatures, ideally to the base temperature of our cryostat of ≈ 3 K. Two iterations of the nano-positioner were built during the duration of this thesis, the second one improving upon the limitations of the first. The following sections include all the details about both versions of the nano-positioner, including the achieved stability of our microcavity, the total fine and coarse tuning range, and the final temperatures reached for the nanoparticles.

The mechanical noise of our cryostat has a frequency of ~ 1 kHz. The basic idea to achieve good passive stability for the cavity is to place it on a stage that is passively isolated from the cryostat via springs that act as low pass filters. Thermal contact between this stage and the cold stages of the cryostat is made with the use of multiple thin copper sheets.

Noise in the low frequency regime can be compensated for by an active feedback mechanism. Fine-tuning range is provided with the help of three piezoelectric actuators that can push the fiber to position it at the desired location in all three dimensions. Coarse tuning range is provided by two stepper motors that push the planar mirror in a plane perpendicular to the fiber.

We first design a so-called ‘block’ on which the fiber microcavity setup will be placed. The block is designed to allow for the assembly of various other parts of our setup onto it, including the holder for the fiber and planar mirrors, piezoelectric actuators on the fiber holder to provide fine-tuning range and stepper motors to provide coarse tuning range for the mirror holder. It sits on springs that are attached to a platform that is henceforth called ‘base’ (on left in Fig. 3.13). Thermal contact between the block and the base is provided by 50 μm thin copper sheets. The base is in thermal contact with the so-called ‘Stage-1’ of the cryostat, which cools down to a temperature of ~ 30 K. Ideally, both the base and the block should be cooled down to the temperature of Stage-1. This will help minimise radiative heating of the planar mirror that is assembled on the block onto which the erbium doped Y_2O_3 nanoparticles are spin-coated.

Note that even though the planar mirror is assembled on the block with the help of the mirror holder, it is thermally isolated from the block with the help of spherical silica balls and Teflon spacers that minimize the heat transfer between them. The mirror holder is in thermal contact with a so-called ‘cold finger’ via copper sheets of 25 μm thickness. The cold finger is in turn in thermal contact with the so-called ‘sample platform’ of the cryostat that cools down to a temperature of ~ 3 K. The thin copper sheets help to minimize the transfer of mechanical noise to the mirror holder.

Fig. 3.13 shows all the components of our nano-positioner in the second iteration. In the second iteration, we made the choice to make the base and block bigger by about 25 % in each dimension for improved performance on all the three key requirements. We hence needed to build a bigger custom vacuum chamber for our cryostat to accommodate the bigger setup. The lowest temperature reached on the base, block and the mirror holder are 66 K, 83 K and 8 K, respectively, in about 5 hours of cooling for the first

iteration, and 61 K, 77 K and 6.5 K, respectively, in about 12 hours of cooling for the second iteration. Note that all the achieved temperatures are lower in the second iteration of the setup. However, as the block, base and mirror holder are all bigger in the second iteration, it takes much longer for them to cool down. The lower temperature achieved on the base in the second iteration could be due to better thermal contact with the Stage-1 of the cryostat. The block also cools down to lower temperatures as the overall larger surface area of both the base and the block in the second iteration allows for numerous cold links for better heat transfer between them.

However, both of them are still higher than the ~ 30 K temperature reached on the Stage-1 of the cryostat. This is mainly due to the high thermal load on the base, combined with imperfect thermal contact between the base and the Stage-1. The high thermal load on the base is not only due to the block, but also to a set of four piezoelectric actuators and three stepper motors that are needed to provide the required fine and coarse scanning range for our setup (see section below).

The temperature of the mirror holder is the most important as that is where the mirror on which the nanoparticles are spin-coated is placed. The mirror holder, which is put in thermal contact with the cold finger via 25 μm thin copper sheets, should ideally reach ~ 3 K. However, the mirror cools down to about 8 K in the first iteration and about 6.5 K in the second iteration. So even though there is an improvement, it is still far from the ideal temperature of ~ 3 K. This temperature can be lowered by improving the heat transfer to the cold finger via the cold links by using multiple layers of copper sheets that are only connected at the end point of contact. However, achieving good thermal contact in this case is difficult due to the extreme thinness of the sheets. Additionally, heating from the block on which the mirror holder is assembled via thermal conduction as well as radiation could also be a significant contribution. Thermal conduction is already minimized in the current configuration by utilizing spacers made out of thermally insulating materials like silica and Teflon wherever there is a contact point. Thermal radiation can be minimized by cooling the block further.

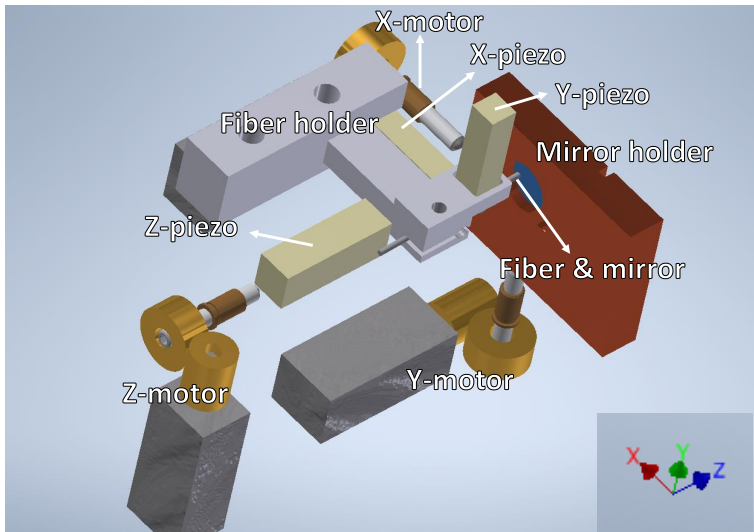


Figure 3.14: Assembly of the fiber holder and mirror holder showing all the components utilized for fine-tuning and coarse-tuning the fiber and mirror. The three piezoelectric actuators provide fast tuning of the cavity position in all three directions by physically moving the fiber. Similarly, the three stepper motors provide coarse tuning in all three directions. In X and Y direction, the X-motor and Y-motor push the mirror holder parallel to the plane, while in the Z direction the Z-motor pushes the Z-piezo thereby pushing the fiber. As indicated, the X and Y axes are defined to lie in the plane of the planar mirror, and the Z-axis is defined perpendicular to that plane along the fiber.

3.3.1 Fiber and mirror holder

The fiber and mirror holder are assembled on the block, which has passive isolation from the mechanical noise coming from the cryostat. The resonance of the block-spring system is measured to be ≈ 20 Hz in the first iteration and ≈ 10 Hz in the second iteration. This translates to an isolation of ≈ 30 dB and ≈ 40 dB at the main frequency component of the

cryostat noise at ≈ 800 Hz. Even with this level of isolation, non-negligible amount of noise is expected to be transmitted to the block. Hence, one design consideration for the fiber and mirror holder is to keep their mechanical resonances away from 800 Hz so as to minimize the coupling to this residual transmitted noise. In addition, both the fiber and mirror holder need to provide for some scanning range so as to locate a suitable nanoparticle among the several that are located at random positions on the planar mirror.

Since the fiber is much lighter than the planar mirror, we decided to design the fiber plus fiber holder system such that it has a high mechanical resonance frequency. This enables the fiber to be used for a high-bandwidth feedback to keep the cavity on resonance via a piezoelectric actuator along the length of the cavity. In addition, we also use the fiber to provide fast scanning range along the surface of the planar mirror via piezoelectric actuators that push the fiber to the desired position. On the other hand, the planar mirror plus holder system is held onto the block with the help of a pulling spring and was designed to have a resonance frequency below 800 Hz. The pull spring enables the mirror holder to be pushed along the surface of the block on which it rests with the help of two stepper motors. Fig. 3.14 shows the entire assembly of the fiber holder and mirror holder in the second iteration with all the components utilized for fine-tuning and coarse-tuning the fiber and mirror.

For the fiber holder, we would ideally want to keep the resonance frequency as high as possible. As the mechanical resonance frequency f depends on the spring constant k and mass m as $f \propto \sqrt{k/m}$, we would like to make it as light and stiff as possible. The first iteration of the fiber holder was made with aluminium to keep it light with a mass of ≈ 5 g. The stiffness cannot be arbitrarily increased in our case as it comes at the cost of reduced fine and coarse tuning range in the Z-direction. We hence designed a fiber holder with an intermediate stiffness that had a resonance frequency $f = 1.8$ kHz. However, aluminium has a very low damping coefficient at low temperatures that leads to very high quality factors for the mechanical oscillator. This is not ideal as the long decay time of mechanical oscillations would result in an oscillating cavity. Hence, following the advice of

	Base	Block	Mirror holder	Range (X,Y)	Stability (full cycle)	Stability (quiet region)
Version 1	66 K	83 K	8 K	50 μm , 30 μm	31 pm	21 pm
Version 2	61 K	77 K	6.5 K	100 μm , 80 μm	18 pm	13 pm

Table 3.1: Comparison between the two iterations of the setup including the temperatures reached on the various components and the cavity stabilities achieved.

Dr. Khaled Karrai from Attocube Systems AG, for the second iteration it was decided to use stainless steel for constructing the fiber holder as it has a higher damping coefficient. The resulting fiber holder had a resonance frequency $f = 5.2$ kHz.

The piezos placed on the fiber holder provide for fast tuning range in all three dimensions. As indicated in Fig. 3.14, they are labelled according to the axis they act on. The X and Y axes are defined to lie in the plane of the planar mirror, and the Z-axis is defined as perpendicular to that plane along the fiber. While the total tuning range available in Z allows us to access cavity modes with different lengths, the tuning range in X and Y allows us to scan for a suitable nanoparticle in that area. In the first iteration of our setup, the total available range was $\sim 50 \mu\text{m}$, $\sim 30 \mu\text{m}$ and $\sim 8 \mu\text{m}$ in the X, Y and Z axes respectively. Due to more available space in the second iteration, we were able to use bigger piezos with more range as well as place them appropriately to maximise the achieved range. Hence the total available range in the second iteration was $\sim 100 \mu\text{m}$, $\sim 80 \mu\text{m}$ and $\sim 20 \mu\text{m}$ in the X, Y and Z axes, respectively.

As the resonance of the mirror holder together with the pulling spring is very low, it should not couple strongly to the cryostat noise. However, it is important that it makes stable contact with the block. In addition, these contacts have to be thermally insulating as the mirror needs to be

much colder than the block. Hence, spherical silica balls were placed on the edge of the mirror holder to make these contacts. Since the point of contact for spherical balls is minimal, they were the best choice to simultaneously provide a stable point of contact and to reduce heat transfer due to conduction. Moreover, as the mirror holder needs to be pushed to have coarse scanning range, the spherical balls provide for smooth sliding along the face of the block.

As the block was smaller in the first iteration, the mirror holder was limited in size. This resulted in the points of contact being too close to each other, that could potentially destabilize the position of the mirror. This also resulted in limited coarse tuning range for the mirror holder due to the limited sliding space on the block. Additionally, the cold links between the mirror holder and the cold finger were thinner, which limited the effective cooling power on the mirror holder. The larger block in the second iteration allowed us to make the mirror holder slightly larger. This gave us more coarse tuning range as well as allowed us to make larger cold links which improves the temperature of the mirror holder from ~ 8 K in the first iteration to ~ 6.5 K in the second iteration. Table. 3.1 summarizes the temperatures reached on various components as well as the fine-scanning range available for both versions of the setup.

3.4 Cavity stability

To ensure the highest Purcell factor, a cavity length stability smaller than the FWHM of the cavity linewidth $\lambda/2F$ is required. For the first generation cavities with $F = 21,000$, this corresponds to a stability better than 37 pm, while for the second generation of cavities with $F = 44,000$ this corresponds to 18 pm. The passively stable nano-positioning platform we have built is robust against the high frequency noise coming from the closed-cycle cryostat such that active stabilization in the low frequency domain of $\sim 50 - 100$ Hz is enough to stabilize the cavity.

We use a second laser at 790 nm to actively stabilize the length of the cavity on an arbitrary point on the transmission fringe. Fig. 3.15(a) shows a

transmission scan at 1535 nm and 790 nm while scanning the cavity length for the second generation of cavities. For this particular measurement, the finesse F of cavity at 790 nm is 2,100 and at 1535 nm is 42,000, which is close to the expected values. The transmission of the 1535 nm light shows two distinct peaks that arise due to a birefringence in our cavity caused by the non-symmetric nature of the concave surface fabricated on the tip of the fiber mirror. Note that for performing all subsequent measurements, including the cavity stability measurements shown in Fig. 3.15(b)-(c), the input polarization was adjusted to interact with only one of these modes.

To stabilize the length of the cavity, we fine-tune the wavelength of the 790 nm laser such that the maximum of the 1535 nm transmission peak overlaps with the middle of the 790 fringe. Then, the transmission of the 790 nm laser is used to monitor cavity drifts and feedback is applied to a piezoelectric actuator to keep this signal at a constant level (side of fringe lock). Fig. 3.15(b) shows the transmission of both lasers as function of the time with the feedback system on while the cryostat is turned off in the second iteration of our setup. As is clear, the transmission of the 1535 nm light is maintained very close to the maximum. The FWHM of the 790 nm mode ($= 188$ pm) can be used to convert the observed change in transmission signal into change in length. The root mean square (RMS) change in the length of the cavity around the set point with the cryostat off is measured to be 3.5 pm at a bandwidth of 5 kHz that is set by the used amplified detector.

When the cryostat is turned on, the lock gets visibly worse as can be seen from Fig. 3.15(c), which shows the cavity transmission over two cycles of the cryostat while the whole setup is still warm. The transmission of the 1535 nm mode drops significantly around the times corresponding to the pumping cycles of the cryostat. This is mainly due to the ~ 1 kHz noise from the cryostat getting transmitted to the cavity through the passive isolation stage. As we don't apply any feedback in this frequency regime, we rely on the natural damping of these oscillations. This is why the transmission is again high in the intermediate regions between the pumping cycle of the cryostat. For the second iteration of our setup, the stability over the whole cycle of the cryostat when the setup is warm is measured to

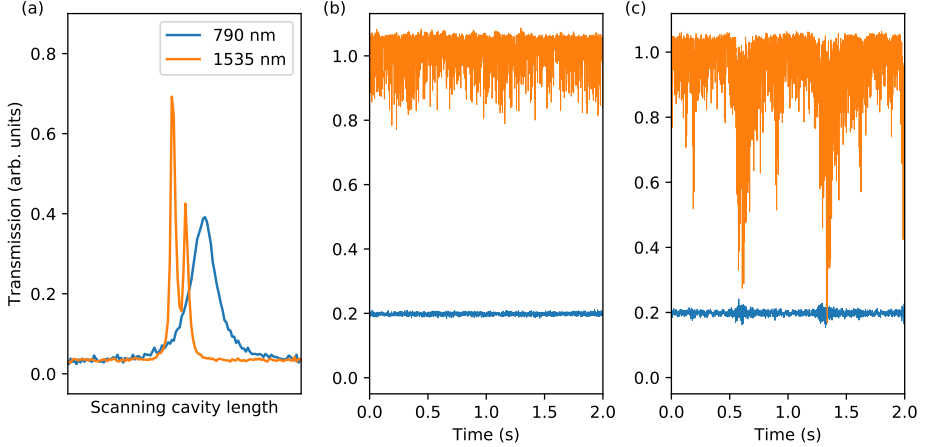


Figure 3.15: Cavity stability in the second iteration of our setup. (a) 790 nm (blue) and 1535 nm (orange) cavity transmission while scanning the cavity length. The cavity length is actively stabilized to the side fringe of the 790 nm transmission while it is on resonance at 1535 nm. For this measurement, the cavity finesse at 790 nm and 1535 nm was 2,100 and 42,000 respectively. The 1535 transmission shows two peaks due to the birefringence of our cavity. (b) Transmission of both the modes during 2 seconds while the cryostat pump is switched off. Estimated cavity stability is 3.5 pm at a bandwidth of 5 kHz. (c) Transmission of both the modes during 2 seconds while the cryostat pump is switched on while the setup is still warm. Estimated cavity stability is 5.6 pm over the whole cycle of the cryostat at a bandwidth of 5 kHz, while in the quiet region it is ≈ 4 pm.

be 5.6 pm, while the stability in the quiet region is ≈ 4 pm.

As discussed before, the natural damping of the mechanical oscillations due to the cryostat noise at ~ 1 kHz when the setup cools down is significantly reduced due to the reduction in the damping coefficient of the material at low temperatures. This problem is significantly worse for aluminium, which was used to fabricate the fiber holder in the first iteration

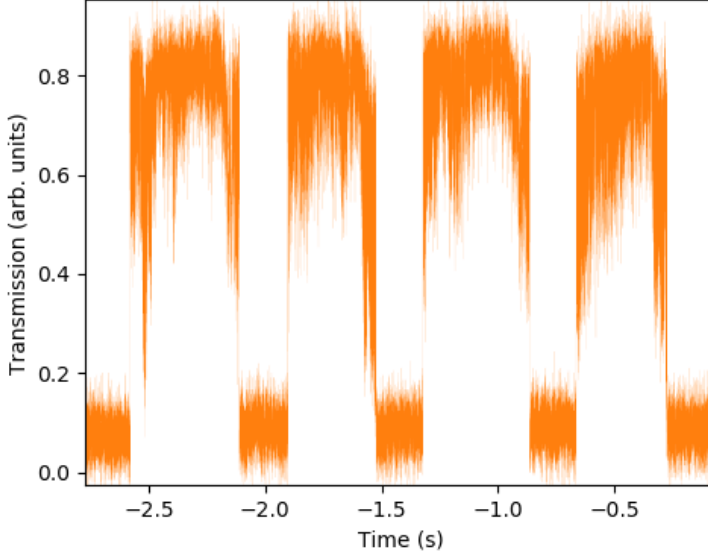


Figure 3.16: Transmission of the cavity at 1535 nm with finesse 17,000 in the quiet parts of the cryostat when the second iteration of our setup is cold. 1535 nm light is turned off during the pumping cycle of cryostat. The stability over the whole cycle of the cryostat is 18 pm, while in the quiet part the stability is ≈ 13 pm

of our setup. In this case, the stability over the whole cycle of the cryostat when the setup was cold was measured to be 31 pm, which reduces to 21 pm in the quiet parts of the cycle (see Sec. 5.2.1 for details). As we used first generation cavities with a finesse of 21,000 (FWHM = 37 pm) with this setup, the achieved stability was sufficient for the measurements that are reported in Ch. 5.

Hence, for the second iteration of our nano-positioner, stainless steel was used to fabricate the fiber holder. This resulted in much better damping of mechanical oscillations at low temperatures compared to the previous fiber-holder. In this case, the stability over the whole cycle of the cryostat

when the setup is cold is measured to be 18 pm, while in the quiet part the stability is ≈ 13 pm, as shown in Fig. 3.16. For the experiments shown in Ch. 7, we perform the experiment only in the quiet region, as shown in Fig. 3.16.

As the second generation of cavities, which had a finesse of 42,000 (FWHM = 18 pm), are used with this nano-positioner, the measured values of stability are within the limit of one FWHM set by the cavity linewidth. This should therefore lead to much better values of Purcell enhancement compared with the first version of our setup. The results obtained with this setup are reported in Ch. 7. Table 3.1 summarizes all the relevant metrics including the achieved cavity stability for both versions of the setup.

3.5 Localizing nanoparticles

As spin-coating of the nanoparticles results in them being randomly spread on the surface of the planar mirror, we utilize both the fine-scanning range on the fiber and the coarse-scanning range on the mirror to identify a suitable nanoparticle. We do so by using the scattering loss microscopy technique [86]. The total transmission through our cavity with the transmissivity of the fiber T_f and that of the planar mirror T_m is given by

$$T_c = \frac{4 T_f T_m}{(T_f + T_m + 2B)^2} \quad (3.15)$$

where $2B$ is the total intra-cavity loss. Hence, knowing the transmission T_c , and the transmissivities of both the mirrors T_f and T_m allows us to calculate total intra-cavity losses $2B$. This can then be used to estimate the size of the nanoparticle, as detailed in Sec. 3.1.3. We look for nanoparticles that introduce a small detectable scattering signal, which maximizes the escape efficiency of the generated photons (see Sec. 3.2.4).

To obtain a map of the transmission of the cavity as a function of different positions on the planar mirror, we utilize the X and Y piezos to move the fiber before measuring the transmission. We begin by dividing the total fine-scanning range in X and Y piezos into discrete steps. To get

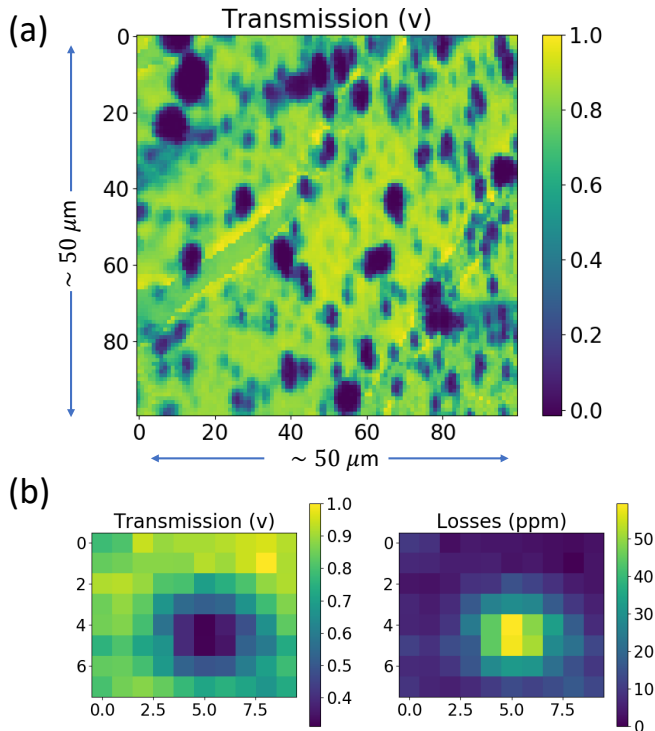


Figure 3.17: (a) Map of the normalized transmission signal as the cavity mode is scanned across a region corresponding to $\sim 50 \mu\text{m}$ in both X and Y directions in the second iteration of our nano-positioner. (b) Map of the normalized transmission signal (left) and the total scattering loss (right) introduced by a single nanoparticle.

an accurate map, this step size has to be smaller than the waist of the cavity mode. For our cavities, a step size of $\sim 1 \mu\text{m}$ is a good compromise between getting an accurate map and obtaining it in a reasonable time. The transmission at each position is measured by scanning the length of the cavity and then measuring the maximum of the obtained transmission

during that scan. All the piezos for scanning are driven using the analog output channels of a National Instruments Card (PCIe-6323) after being amplified with piezo-amplifiers that can drive voltages up to ± 150 V. The peak of the transmission signal is recorded with the help of a commercially available FPGA (Red Pitaya).

Fig. 3.17(a) shows a map of the normalized transmission signal as the cavity mode is scanned across a region corresponding to $\sim 50 \mu\text{m}$ in both X and Y directions in the second iteration of our nano-positioner. Regions with low transmission correspond to nanoparticles. Fig. 3.17(b) shows the map of the normalized transmission signal (left) and the total scattering loss (right) introduced by a single nanoparticle. By measuring the change in the transmission signal while the cavity mode is centred on the nanoparticle compared to a clean spot on the planar mirror, we estimate the total scattering loss introduced by the nanoparticle to be $2B = 54$ ppm, which corresponds to a diameter of 152 nm.

Chapter 4

Spectroscopy of nano-scale $\text{Er}^{3+}:\text{Y}_2\text{O}_3$ and $\text{Pr}^{3+}:\text{Y}_2\text{O}_3$

The ${}^4I_{15/2} - {}^4I_{13/2}$ transition in erbium lies in the telecom band and is hence very attractive from the prospect of integrating it into existing commercial telecom fiber networks. Erbium doped solids have shown excellent optical and spin coherence properties in bulk materials [40, 61, 62]. Except one previous work by Lutz et al. in 2017 [95], their coherence properties are not well studied in nano-scale materials. In this chapter, we perform a spectroscopic study of $\text{Er}^{3+}:\text{Y}_2\text{O}_3$ nanoparticles. We begin by detailing how the samples were synthesized in Sec. 4.1. In Sec. 4.2, we describe our sample preparation and our experimental setup. Following that, we perform measurements of: the optical inhomogeneous linewidth and lifetime in Sec. 4.3.2, homogeneous linewidth and its dependence on temperature in Sec. 4.3.3, and quantify time-dependent spectral diffusion in Sec. 4.3.4. In Sec. 4.4, we detail the prospect of using single erbium ions doped in Y_2O_3 nanoparticles as a source of indistinguishable single photons.

Finally in Sec. 4.5, we study Pr^{3+} as an alternative to erbium. Using Pr^{3+} doped into Y_2O_3 nanoparticles, we first investigate the optical coherence properties of the ${}^1D_2 - {}^3H_4$ transition at 619 nm and its dependence on temperature. Then we identify the hyperfine level structure

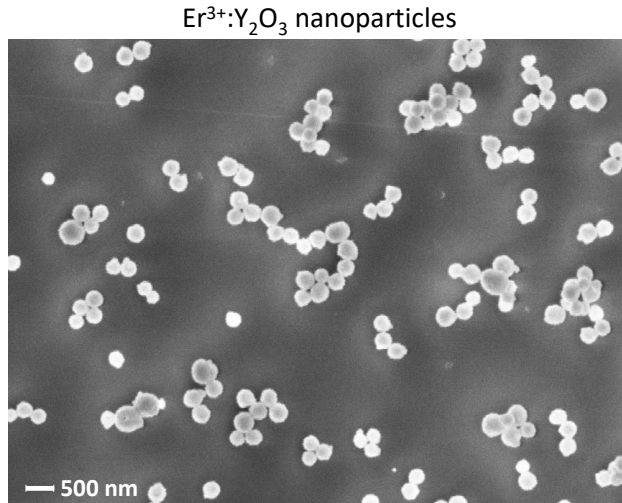


Figure 4.1: SEM image of $\text{Er}^{3+}:\text{Y}_2\text{O}_3$ nanoparticles with average size of 140 nm. Image courtesy: Dr. Diana Serrano, ChimieParistech, Paris

using spectral hole burning, and study the coherence properties of the spin transitions using spin-echo techniques implemented using two-colour Raman pulses. Finally, we comment on the prospect of using a single Pr^{3+} ion as a spin-photon interface.

The results regarding $\text{Er}^{3+}:\text{Y}_2\text{O}_3$ nanoparticles are taken from a paper that is currently in preparation together with other authors [96], while the results regarding $\text{Pr}^{3+}:\text{Y}_2\text{O}_3$ nanoparticles have been published in the journal *Physical Review B* [60].

4.1 Material

The Y_2O_3 nanoparticles that were investigated in this study were synthesized by Dr. Shuping Liu in the group of Dr. Philippe Goldner at

ChimieParisTech, Paris. They were doped with Er^{3+} at 200 ppm atomic concentration with an average particle size of 140 nm (see Fig. 4.1). The nanoparticles appear poly-crystalline, with crystal grains of the order of 100 nm. The synthesis route is based on homogeneous precipitation followed by high-temperature annealing (see Sec. 3.1.1).

In addition, Y_2O_3 ceramics doped with Er^{3+} at 200 ppm atomic concentration were also investigated to use as bulk references. Those were fabricated from a mix of commercial Y_2O_3 and Er_2O_3 oxide powders (with 99.99 % purity). The powders were pressed into pellets with a pressure of 5 MPa, and then annealed at 1500 °C for 48 h under air atmosphere. The obtained ceramics were cut into thin slabs of $\sim 250 \mu\text{m}$ for the optical measurements.

4.2 Methods

4.2.1 Sample preparation

Both the nanoparticle and ceramic samples are highly scattering and typical transmission for a thickness of few hundred microns is $< 10^{-4}$. Hence, we made use of a copper holder with a pinhole that transmits only the light that has interacted with the sample while blocking all other light (see Fig. 4.2). Nanoparticle samples were prepared by filling the copper holder with the nanoparticles and compressing, while ceramic samples were cut into small pieces and stuck on top of the pinhole. Small cylindrical permanent magnets with a hole in the centre were placed on top of the copper holder to apply a small magnetic field of ~ 100 G for all the measurements.

4.2.2 Optical setup

The transition of interest in Er^{3+} is the ${}^4I_{15/2} - {}^4I_{13/2}$ transition in site 1 at around 1535 nm, which lies in the telecom band. The excitation light was obtained from an extended cavity diode laser at 1535 nm (Toptica CTL), which was then amplified by a Keysight Erbium-doped Fibre Amplifier to reach a peak power of ~ 500 mW. The amplified light was sent through a

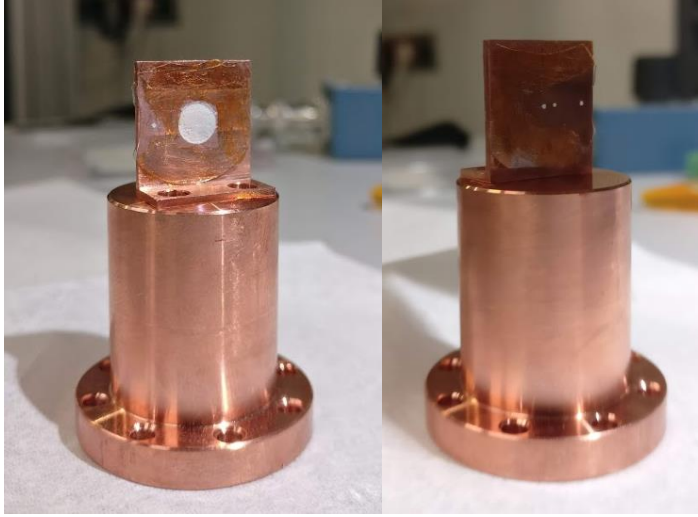


Figure 4.2: Sample holder for both the ceramics and the nanoparticles. It is a copper holder (left) with a pinhole in the back (right) that transmits only the light that has interacted with the sample while blocking all other light.

double-pass Acousto-Optic-Modulator (AOM) for pulse modulation. The light was then filtered with a bandpass filter at 1535 ± 3 nm before being focused onto the sample using a 35 mm spherical lens to achieve a spot-size of ≈ 100 μm . Typical peak power at the sample was ~ 150 mW. The samples were prepared on a copper holder with a pinhole and placed on the cold-finger of a Montana Instruments closed-cycle cryostat, which is cooled down to a minimum of 3 K. The transmitted light was then loosely focused onto an Avalanche Photo-Diode (Thorlabs APD130) with the help of two spherical lenses, each with a focal length of 60 mm. The signal from the APD was recorded on an oscilloscope. A small magnetic field of ~ 100 G was applied for all of the measurements in this chapter with the help of permanent magnets.

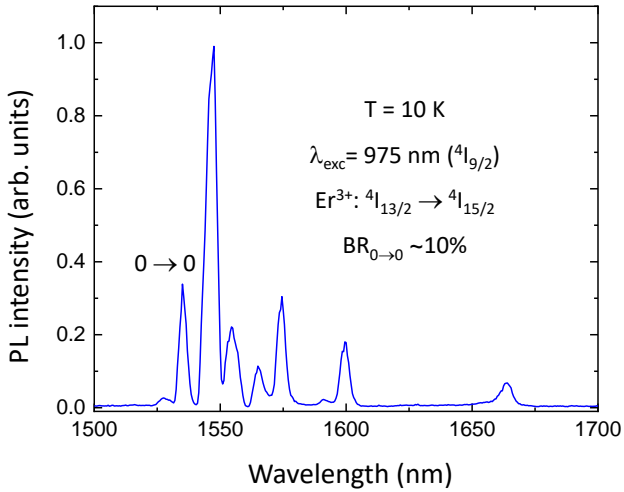


Figure 4.3: Fluorescence spectra from single nanoparticles of $Er^{3+}:Y_2O_3$ at 10 K on the ${}^4I_{15/2} - {}^4I_{13/2}$ transition at $1.5 \mu\text{m}$, where we measure a branching ratio of 13 % for the ZPL.

4.3 Results

4.3.1 Branching ratio

The low temperature emission spectra shown in Fig. 4.3 were recorded at 10 K using a close-cycle cryostat. These measurements were done in ChimieParistech (Paris) by Dr. Diana Serrano. Excitation was carried out with a tunable optical parametric oscillator (OPO) pumped by a $Nd^{3+}:YAG$ Q-switched laser (Ekspla NT342BSH with 6 ns pulse length and 10 Hz repetition rate). Spectra were recorded using an Acton SP2300 spectrometer equipped with 600 grooves/mm holographic grating centered at $1.2 \mu\text{m}$. A Ge detector was used to detect the Er^{3+} emission. The excitation wavelength was 975 nm while the collection was around $1.5 \mu\text{m}$ on the

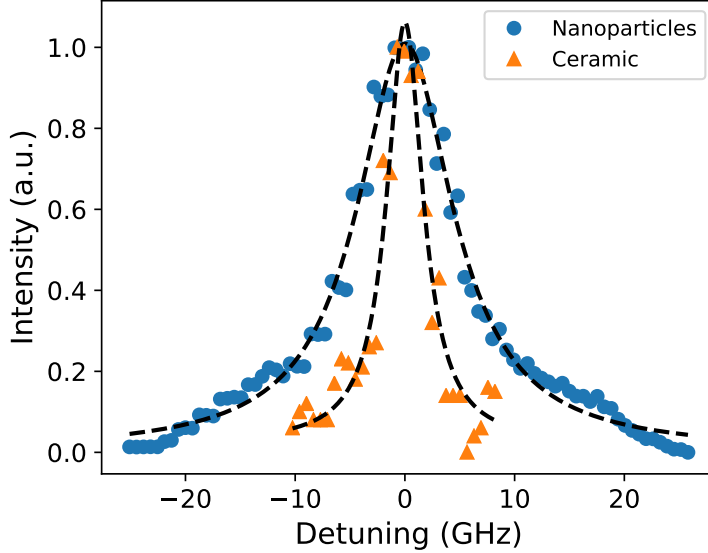


Figure 4.4: Inhomogeneous linewidth of $\text{Er}^{3+}:\text{Y}_2\text{O}_3$ was measured to be 3.98 GHz in ceramic (orange triangles), and 10.7 GHz in nanoparticles (blue circles).

${}^4I_{15/2} - {}^4I_{13/2}$ transition. We note that the spectrum in Fig. 4.3 contains lines from both C_2 and S_6 sites. We estimate a branching ratio of 13 % on the zero-phonon line (ZPL) for Er^{3+} ions in C_2 . This is however a lower bound value as not all S_6 emission lines could be resolved from C_2 and hence could not be subtracted from the total emission intensity estimation. All measurements reported in this chapter are done on the ZPL.

4.3.2 Inhomogeneous linewidth and lifetime

We first measured the inhomogeneous linewidth of the ZPL of our samples. For that purpose, the transition was excited by a ~ 100 μs pulse followed by fluorescence detection with an APD. The normalized integrated fluores-

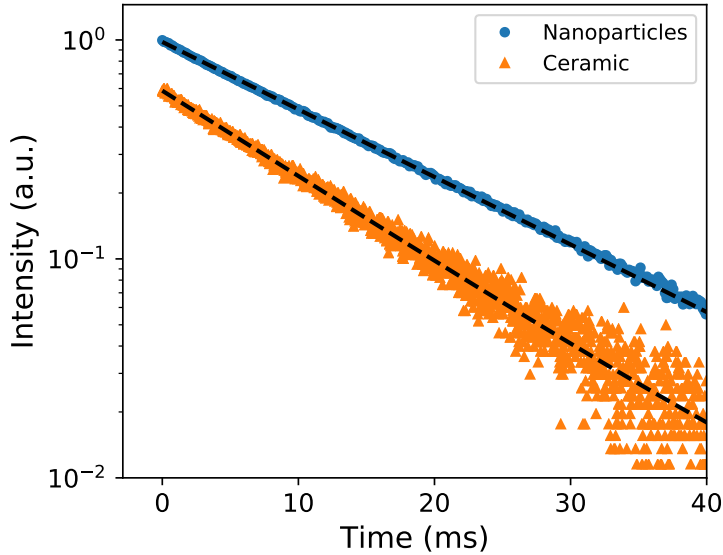


Figure 4.5: Lifetime of the excited state of $\text{Er}^{3+}:\text{Y}_2\text{O}_3$ was measured to be 10.91 ms in ceramic (orange triangles), and 13.68 ms in nanoparticles (blue circles).

cence as a function of excitation wavelength for both ceramics and nanoparticles is shown in Fig. 4.4. The center of the inhomogeneous line in the ceramic sample was found to be at 1535.43 nm with a linewidth of 3.9(4) GHz, while in the nanoparticles the line was red-shifted to 1535.48 nm, with a linewidth of 10.7(3) GHz. The red-shifting and broadening of the inhomogeneous line in nanoparticles as compared to the ceramics could be explained by the presence of tensile strain in the nanoparticles due to defects [60].

Excited state lifetimes were recorded at the centre of the inhomogeneous lines for both the samples by using a ~ 100 us excitation pulse followed by fluorescence detection with an APD. Fig. 4.5 shows the excited state lifetime measurements for all the samples. The excited state lifetime was found to be 10.91 ms in ceramic and 13.68 ms in nanoparticles. The increase in the

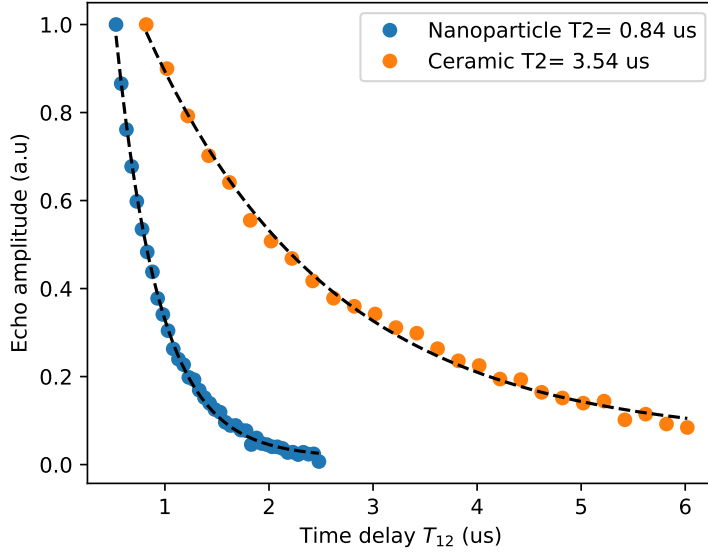


Figure 4.6: Coherence time of $\text{Er}^{3+}:\text{Y}_2\text{O}_3$ nanoparticles (blue) and ceramic (orange) measured at a temperature of 3 K and a magnetic field of 100 G. Dashed line is a fit to Eq.(4.1) that gives a coherence time T_2 of $0.84 \mu\text{s}$ for nanoparticles and $3.54 \mu\text{s}$ for ceramic.

lifetime of the nanoparticles compared to ceramic can be explained by the reduction of the effective surrounding refractive index in the nanoparticle samples. This agrees with previous work where a decrease in the lifetime of Eu^{3+} doped nanoparticles was found when it was embedded in a PMMA layer as compared to no embedding [66].

4.3.3 Homogeneous linewidth versus temperature

Coherent spectroscopy of the ZPL of the ${}^4I_{15/2} - {}^4I_{13/2}$ line was carried out using a two-pulse photon echo sequence followed by a heterodyne detection scheme. Ideally the pulse areas of the two pulses should be $\pi/2$ and π

respectively. However, the highly scattering nature of the samples leads to different parts of the sample seeing different pulse areas for the same pulse. Hence, both the $\pi/2$ and π pulses were 240 ns in length with a peak power of 150 mW focused onto a spot-size of $\approx 100 \mu\text{m}$. The pulse for heterodyne detection was 1 μs long with a frequency detuning of 24 MHz and less than 1 mW of power. The resulting beating signal from the APD was recorded on an oscilloscope after passing through a high-pass filter with a cut-off frequency of ~ 5 MHz to filter out electronic noise. A Fast Fourier Transform (FFT) of the signal allows us to extract the amplitude of the electric field at the beating frequency of 24 MHz. The electric field amplitude E of the echo is recorded as a function of the time delay between the first two pulses t_{12} , which is varied from few hundred nanoseconds upto few microseconds, and fit to the following equation

$$E = E_0 \exp(-2t_{12}/T_2). \quad (4.1)$$

Here T_2 is the coherence time of the transition, which is related to the homogeneous linewidth by $\Gamma_h = 1/(\pi T_2)$. At the lowest temperature of 3 K and a small magnetic field of ~ 100 G, we measure a T_2 of 840 ns ($\Gamma_h = 379$ kHz) for the nanoparticles, and a T_2 of $3.54 \mu\text{s}$ ($\Gamma_h = 90$ kHz) for the ceramics. Note that the reported temperature is the one that is recorded on a sensor that is mounted on the sample platform. As it is difficult to thermalize our samples, especially the nanoparticles, there is some uncertainty on the the actual temperature of the samples themselves.

We then investigated the dependence of homogeneous linewidth as a function of temperature for the nanoparticles, as shown in Fig. 4.7. The measurements were done at a magnetic field of 100 G. The homogeneous linewidth is expected to have the following behaviour [58]:

$$\Gamma_h(T) = \Gamma_0 + \alpha_{\text{TLS}}T + \frac{\alpha_{\text{Orb}}}{\exp\left(\frac{\Delta E}{k_B T}\right) - 1} \quad (4.2)$$

Here Γ_0 is the linewidth extrapolated to 0 K, the coefficients α_{TLS} and α_{Orb} quantify the coupling to Two-Level Systems (TLS) and resonant two-phonon Orbach processes, ΔE is the energy difference between the two

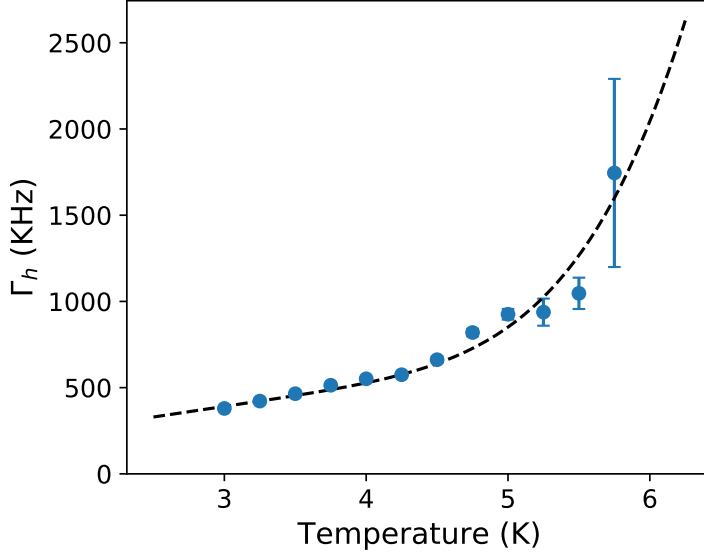


Figure 4.7: Homogeneous linewidth of $\text{Er}^{3+}:\text{Y}_2\text{O}_3$ nanoparticles measured as a function of temperature at a magnetic field of 100 G. Dashed line is a fit to Eq.(4.2) that gives: $\Gamma_0 = 9.8$ kHz, $\alpha_{\text{TLS}} = 121.7$ kHz/K, and $\alpha_{\text{Orb}} = 1.1\text{e}7$ kHz. All bars represent 95% confidence interval obtained from the fit.

lowest lying crystal field levels of the ground state, and k_B is the Boltzmann constant. TLSs are localized vibrational modes that exhibit a double-well potential energy structure. By tunnelling between the two states, they can drive spins that couple to them which can then lead to spectral diffusion. TLSs are typically found in amorphous materials, and a high coefficient typically suggests poor crystalline quality of the samples. Two-phonon Orbach processes can transfer ions from one state to the other in a lambda-type scheme assisted by two resonant phonons [97]. A fit to Eq. (4.2) with $\Delta E = 39 \text{ cm}^{-1}$ [98] gives $\Gamma_0 = 9.8$ kHz, $\alpha_{\text{TLS}} = 121.7$ kHz/K, and $\alpha_{\text{Orb}} = 1.1 \text{ e}7$ kHz. The linear dependence of homogeneous linewidth at

lower temperatures has been observed in similar systems and is attributed to spectral diffusion due to neighbouring two-level systems (TLSs) [58, 99].

For comparison, using a 80 ppm erbium doped silica fibers at a temperature of 0.7 K and a magnetic field of 600 G, Veissier et al. measured $\alpha_{\text{TLS}} = 1.1$ MHz/K, which is an order of magnitude higher value for the coefficient than our case [99]. This is to be expected as this coefficient depends on the crystalline quality of the material and our nanoparticles should in principle be more crystalline than fibers which are amorphous materials.

4.3.4 Spectral diffusion via three-pulse echo

We now investigate spectral diffusion in $Er^{3+}:Y_2O_3$ nanoparticles via the three-pulse photon echo (3PPE) technique where all three pulses are 240 ns in length. To quantify the broadening in Γ_{eff} as a function of time, we keep the separation between the first two pulses t_{12} constant at 150 ns, while varying the separation between pulses two and three t_{23} from 3 μs to 40 μs . The decay of echo amplitude in 3PPE technique is given by [62]:

$$E = E_0 \exp\left(\frac{-t_{23}}{T_1}\right) \exp(-2t_{12}\pi\Gamma_{\text{eff}}), \quad (4.3)$$

where T_1 is the excited state lifetime. We have $T_1 = 13.68$ ms (as measured above), and $3 \mu\text{s} \leq t_{23} \leq 40 \mu\text{s}$. Hence, the first factor is negligible for our parameters and all decay in echo amplitude is expected to come from a broadening of Γ_{eff} . We begin by recording the decay in the echo amplitude as a function of t_{23} . For the first point of $t_{23} = 3 \mu\text{s}$, we set Γ_{eff} to the value of Γ_h that was obtained from the 2PPE technique, that is $\Gamma_{\text{eff}} = 379$ kHz. By estimating the relative decay in echo amplitude for all subsequent t_{23} , we extract Γ_{eff} as a function of t_{23} that is shown in Fig. 4.8. For systems coupled to two-level systems (TLS), the Γ_{eff} is expected to have the following behaviour [99]:

$$\Gamma_{\text{eff}}(t_{12}, t_{23}) = \Gamma(t_0) + \gamma_{sd} \log_{10}\left(\frac{t_{23}}{t_0}\right), \quad (4.4)$$

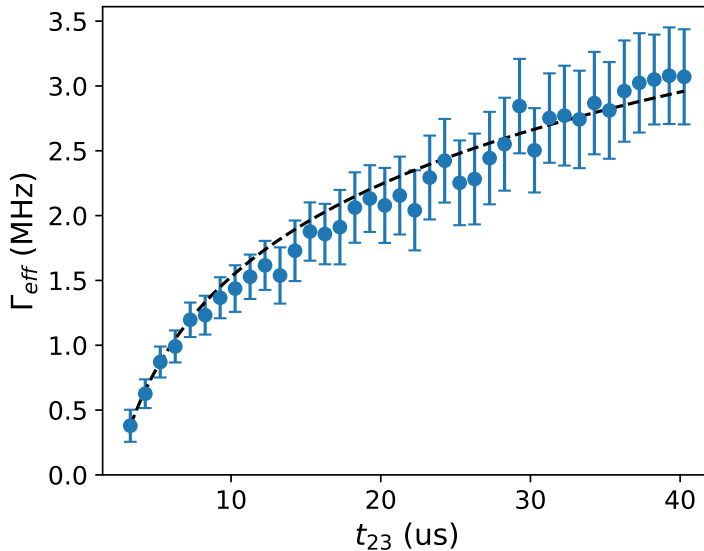


Figure 4.8: Effective homogeneous linewidth of $Er^{3+}:Y_2O_3$ nanoparticles as a function of t_{23} in a three-pulse photon echo sequence. Dashed line is a fit to Eq. 4.4, giving $\Gamma(t_0) = 378$ kHz and $\gamma_{sd} = 2.3$ MHz. Error bars are one standard deviation of parameter estimate from fit.

where t_0 is the minimum value of $t_{12} + t_{23}$ and γ_{sd} is a coupling coefficient. For our case, $t_0 \approx 3 \mu\text{s}$ and $\Gamma_0 = 379$ kHz. Fitting the Γ_{eff} that we obtained above to Eq.(4.4), we obtain $\gamma_{sd} = 2.3$ MHz. For comparison, Veissier et al. measured $\gamma_{sd} \approx 0.4$ MHz, which is much lower than our case. Since the main source of spectral diffusion in amorphous materials is coupling to TLS, a lower value for γ_{sd} for the fibers would imply a smaller coupling to TLSs in that material. But this is contradictory to our conclusion in the section above based on a comparison of the measured values of α_{TLS} . Since three pulse photon echoes probe spectral diffusion on longer time scales, different mechanisms could be causing spectral diffusion on these time-scales in both cases.

4.4 Prospects as a source of indistinguishable photons

Single erbium ions would be ideal candidates for use as quantum nodes in a quantum network due to their emission at telecommunication wavelengths. Furthermore, erbium ions that are spatially close to each other in the solid-state matrix allow for multi-qubit operations, which is highly desirable in a quantum network. A key requirement for using single-emitters as quantum nodes is that the emitted photons should be indistinguishable. To extract indistinguishable photons from a single erbium ion in the absence of spectral diffusion, we need to satisfy the condition $T_2 = 2T_1$, where T_1 is the lifetime of the excited state, and T_2 is the coherence time. This can be also written as $\Gamma_h = \Gamma_r$, where $\Gamma_h = 1/(\pi T_2)$ is the homogeneous linewidth and $\Gamma_r = 1/(2\pi T_1)$ is the radiative linewidth. The presence of spectral diffusion can make the photons distinguishable by shifting the frequency of the emitter as a function of time. This results in an effective broadening of the emitter linewidth to Γ_{eff} . The condition for indistinguishable photons can then be written as $\Gamma_{\text{eff}} \approx \Gamma_r$.

We first consider the case without spectral diffusion. For the values we have measured for $\text{Er}^{3+}:\text{Y}_2\text{O}_3$ nanoparticles in this chapter, which is $T_1 = 13.7$ ms and $T_2 = 840$ ns, we have $T_2 \ll 2T_1$. To satisfy the condition for indistinguishable photons, we would need to either increase T_2 or decrease T_1 . As discussed in Sec. 4.3.3, the T_2 at low temperatures in the current samples is limited due to fast spectral diffusion arising from coupling to neighbouring two-level systems (TLS). This behaviour is characteristic of amorphous materials [99], and could be arising in our system due to the presence of defects and the poor crystalline quality of our nanoparticles. As the contribution from TLS to homogeneous linewidth depends on temperature, coherence times can be significantly improved by cooling the samples further. In our current samples, the homogeneous linewidth reduces by 121 kHz per kelvin and reaches a value of 10 kHz ($T_2 \approx 32$ μs) when extrapolated to 0 K. The effect of TLS can also be minimized by annealing the samples at high temperatures ($> 1200^\circ\text{C}$), but this also leads to an

increase in the average size of our nanoparticles. As the total scattering loss $2B \propto d^6/\lambda^4$, where d is the diameter of the particle (see Sec. 3.1.3), an increase in the size of the particle would make it more difficult to integrate them into microcavities. An alternative method that involves starting with bigger higher quality nanoparticles and then chemically etching them down to the required size has shown promising results [77]. By chemically etching 400 nm Y_2O_3 nanoparticles doped with europium down to 150 nm, they were able to demonstrate a T_2 of 10 us.

Nonetheless, it is clear that both for the purpose of producing indistinguishable photons and also for making the emission efficient, we would need to reduce additionally the T_1 (see Sec. 1.2 for details). This can be achieved by coupling the emitter to an optical cavity. When coupling an emitter to a cavity, the emitter's excited state lifetime is reduced to $T_c = T_1/(C + 1)$, where T_1 is the natural lifetime, T_c is the Purcell enhanced lifetime, and C is the Purcell factor. For a fiber based plano-concave microcavity as the one used in this thesis with finesse F , radius of curvature R and length L , C is given by (see Sec. 2.4.1)

$$C = \zeta \frac{6\lambda}{\pi^2} \frac{F}{\sqrt{RL}} \quad (4.5)$$

where ζ is the branching ratio of the relevant transition and λ is the wavelength. To efficiently extract photons emitted by ions in our nanoparticle coupled to a microcavity, this scattering loss needs to be smaller than all other losses in the cavity.

The $Er^{3+}:Y_2O_3$ nanoparticles investigated in this thesis with an average size of 150 nm introduce a scattering loss of ≈ 31 ppm. Assuming the total transmittivity losses of the cavity to be ≈ 100 ppm, we can use cavities with $F \sim 60,000$. By using $R = 20 \mu\text{m}$ and $L = 2 \mu\text{m}$, which are already experimentally feasible (see Sec. 3.2.2), and $\zeta = 0.13$ as we have reported above, we get $C \sim 1,000$. Using $T_1 = 13.68$ ms as we have measured above, this corresponds to $T_c \sim 14 \mu\text{s}$. To produce indistinguishable photons we would then need $T_2 \sim 28 \mu\text{s}$, which is much higher than the value of $T_2 \sim 1 \mu\text{s}$ that we measured in this chapter. However, improved sample fabrication, such as with chemical etching of higher quality nanoparticles,

as well as cooling the samples further could result in much higher values of T_2 . Additionally, if the nanoparticles can be made with an average diameter of ≈ 100 nm, then the scattering losses drop to ≈ 4 ppm, in which case it would be possible to use cavities with $F \sim 200,000$ that would result in $C \sim 3,000$ and $T_c \sim 5 \mu\text{s}$. In this case, the required $T_2 \sim 10 \mu\text{s}$ could be more easily achieved.

Once spectral diffusion is factored in, the effective linewidth Γ_{eff} of Er^{3+} ions in Y_2O_3 nanoparticles increases significantly with time. In Sec. 4.3.4, after a time of $40 \mu\text{s}$, we measure $\Gamma_{\text{eff}} \approx 3$ MHz, which is almost an order of magnitude broader than $\Gamma_h = 378$ kHz that was measured using two-pulse photon echoes at shorter time-scales. Hence, the requirement on the Purcell factor needed would be much higher in this case. As coupling to TLSs is the main contribution to spectral diffusion in our case, nanoparticles with better crystalline quality could mitigate this issue. Alternately, erbium-doped Y_2SiO_5 crystal that is polished down to a thickness of $20 \mu\text{m}$ has recently shown exceptionally narrow optical linewidths, with $\Gamma_h \approx 3$ kHz and $\Gamma_{\text{eff}} \approx 100$ kHz [57]. Producing indistinguishable photons from Er^{3+} ions in such crystals would require $C \sim 10,000$, which could be within reach with state of the art Fabry-Perot cavities [100].

We have performed the first experiments on inserting $\text{Er}^{3+}:\text{Y}_2\text{O}_3$ nanoparticles into fiber-based optical microcavities in this thesis and the results are presented in Ch. 5 and Ch. 7.

4.5 $\text{Pr}^{3+}:\text{Y}_2\text{O}_3$ nanoparticles

Praseodymium is another rare-earth ion that has shown excellent optical and spin coherence properties in bulk crystals. It has been extensively used for demonstrations of storage of quantum light both in the excited state [19, 101, 102] and in the spin state [38, 42, 44, 103]. It has a high oscillator strength on the $^1D_2 - ^3H_4$ transition at around 619 nm that results in a short T_1 . In addition, Pr^{3+} has a branching ratio into the ZPL that is larger than some other rare-earth ions, such as europium. These properties together make single Pr^{3+} ions a promising platform for a spin-

photon interface. When combined with optical frequency conversion into the telecom band, such an interface could also be easily integrated with existing telecom fiber networks [104].

However, while very few previous studies on the optical coherence properties of $Pr^{3+}:Y_2O_3$ exist [105–107], there are no studies on the spectroscopic properties of the spin-state. In this section we study the spectroscopic properties of both the optical and spin states of $Pr^{3+}:Y_2O_3$. The work was done together with Dr. Diana Serrano in the lab of Dr. Philippe Goldner at ChimieParistech (Paris, France). The results reported in this section have been published in the journal *Physical Review B* [60], and the figures and text from the published paper have been suitably adapted here where necessary.

We investigate two batches of 500 ppm $Pr^{3+}:Y_2O_3$ nanoparticles with average sizes of 400 nm and 150 nm diameter, and crystalline domains of 120 nm and 80 nm respectively as determined by x-ray diffraction [84]. They were synthesized using the same technique as used for $Er^{3+}:Y_2O_3$ nanoparticles above that is based on homogeneous precipitation followed by high temperature annealing (see Sec. 3.1.1 for details). The 400 nm particles were annealed at 1200 °C, while the 150 nm particles were annealed at 900 °C. The lower annealing temperature of the 150 nm particles was to avoid particle agglomeration which becomes a serious problem at these sizes. It is also the reason crystalline domains are smaller in 150 nm particles. After synthesis, both samples were subjected to oxygen plasma at 900 W for 3 minutes. In addition, we used a 500 ppm $Pr^{3+}:Y_2O_3$ ceramic with crystalline domains of $\sim 1 \mu\text{m}$ as a bulk reference. Those were fabricated from a mix of commercial Y_2O_3 and Pr_6O_{11} powders (with 99.99 % purity). The powders were pressed into pellets with a pressure of 5 MPa, and then annealed at 1500 °C for 48 h under air atmosphere. The obtained ceramics were cut into thin slabs of $\sim 250 \mu\text{m}$ for the optical measurements.

The optical setup used is very similar to the ones described above in Sec. 4.2.2 for $Er^{3+}:Y_2O_3$. The excitation laser was a continuous wave dye laser (Sirah Matisse DS), that passed through an acousto-optic modulator for pulse shaping and frequency shifting. The light was then focused using spherical lenses onto the samples which were placed in a copper holder

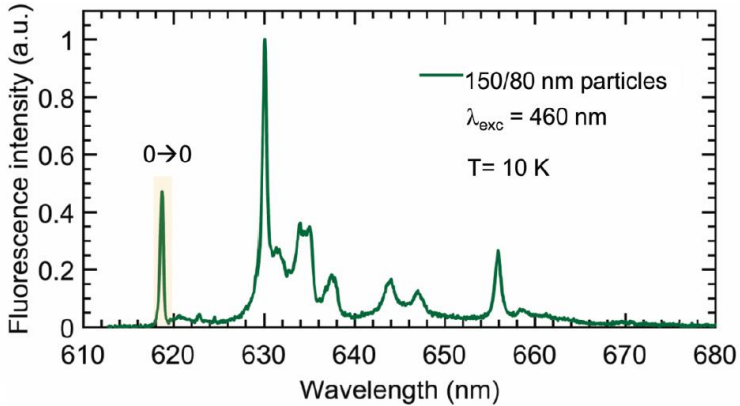


Figure 4.9: Fluorescence spectra from single nanoparticles of $Pr^{3+}:Y_2O_3$ at 10 K on the $^1D_2 - ^3H_4$ transition at 619 nm after excitation at 460 nm. By estimating the emission in the zero-phonon line compared to the total overall emission, we extract a branching ratio of 5.7 % for the zero-phonon line.

with a pinhole. Peak power at the sample was ~ 50 mW and spot-size of $\approx 50 \mu\text{m}$. The samples were placed in a helium bath cryostat (Janis SVT-200) which could be cooled down to 1.4 K when operated in liquid mode. The light that interacts with the sample was then collected using spherical lenses before being focused onto a detector (Thorlabs A/M110).

The photoluminescence measurements shown in Fig. 4.9 were performed in a closed cycle cryostat at 10 K with a 460 nm excitation laser. Emitted light was sent to a spectrometer (Acton SP2300) and detected using a CCD camera (Princeton Instruments). By estimating the emission in the zero-phonon line compared to the total overall emission, we extract a branching ratio of 5.7 % for the zero-phonon line. This value is much higher than for

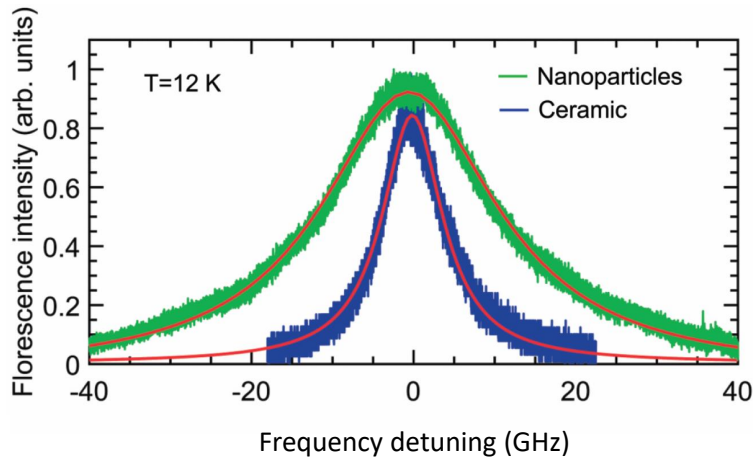


Figure 4.10: Optical inhomogeneous linewidth of $Pr^{3+}:Y_2O_3$ samples was measured to be 9 GHz in ceramics with a centre at 619.011 nm and 27 GHz for the nanoparticles with a centre at 619.001 nm.

europium doped Y_2O_3 , which is $\approx 1\%$ [66].

Optical inhomogeneous lines of the $^1D_2 - ^3H_4$ transition for both the $Pr^{3+}:Y_2O_3$ ceramics and nanoparticles were obtained by exciting around the central wavelength of 619 nm and collecting the resulting fluorescence after passing through a long-pass filter. We find the linewidth of the Lorentzian line to be 9 GHz for the ceramic with a centre at 619.011 nm and 27 GHz for the nanoparticles with a centre at 619.001 nm. The broadening and blue-shifting of the linewidth in the nanoparticles is due to the post-synthesis oxygen plasma treatment, which induces an additional strain in the nanoparticle due to the increased oxygen content [90]. The lifetime of the excited state was measured to be $T_1 = 140 \mu s$ at 1.4 K for 400 nm nanoparticles with an excitation at 619.008 nm (see Fig. 4.11). In comparison, T_1 for europium doped Y_2O_3 nanoparticles is ≈ 1 ms [76] and that

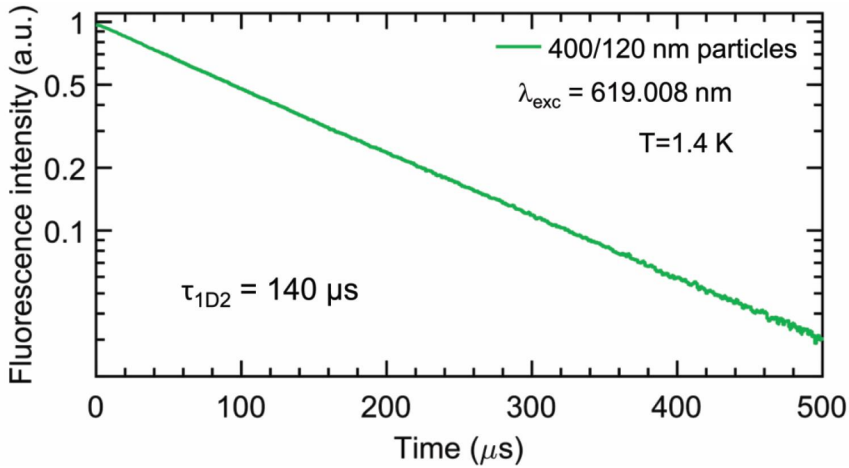


Figure 4.11: Excited state lifetime of 400 nm $Pr^{3+}:Y_2O_3$ nanoparticles was measured to be 140 μs with an excitation at 619.008 nm.

for erbium is ≈ 13 ms [96].

4.5.1 Optical homogeneous linewidth

The coherence time of the optical transition is obtained by using the two-pulse photon echo technique, where the echo is detected using a heterodyne detection method. The echo amplitude is expected to decay as a function of delay between the two pulses τ as

$$E = E_0 \exp(-2\tau/T_2) \quad (4.6)$$

where T_2 is the coherence time of the transition, which is related to the homogeneous linewidth by $\Gamma_h = 1/(\pi T_2)$. At the lowest available tempera-

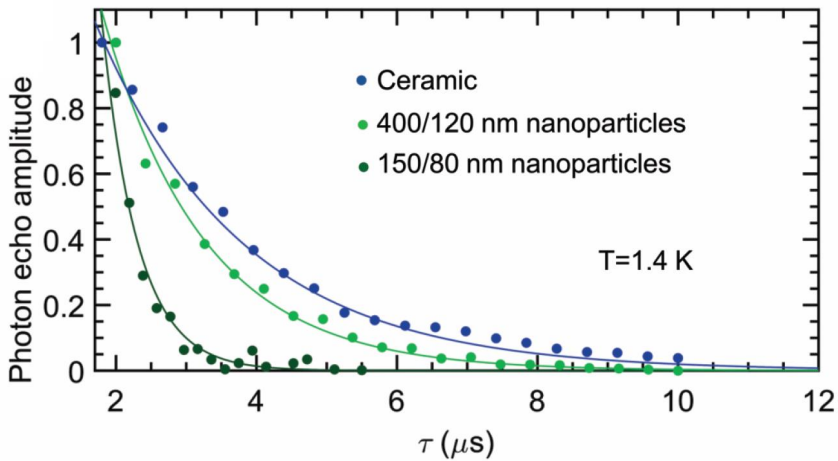


Figure 4.12: Coherence time at a temperature of 1.4 K of $Pr^{3+}:Y_2O_3$ samples was measured to be $4.5 \mu s$, $3 \mu s$ and $1 \mu s$ for the ceramics (blue), nanoparticles with 400 nm diameter (green) and nanoparticles with 150 nm diameter (dark green) respectively.

ture of 1.4 K and no magnetic field, decay in echo amplitude as a function of τ for the different $Pr^{3+}:Y_2O_3$ samples is plotted in Fig. 4.12. We measure a coherence time of $4.5 \mu s$ ($\Gamma_h = 70$ kHz), $3 \mu s$ ($\Gamma_h = 106$ kHz) and $1 \mu s$ ($\Gamma_h = 318$ kHz) for the $Pr^{3+}:Y_2O_3$ ceramics (blue), nanoparticles with 400 nm diameter (green) and nanoparticles with 150 nm diameter (dark green) respectively. The homogeneous linewidth appears to be broadening as the size of the crystalline domains decreases. There are two dephasing mechanisms that explain this behaviour. First, as the crystalline domains become smaller, the coupling of the emitters to neighbouring two-level systems (TLS) that arise in amorphous-like materials increases [58, 99]. This

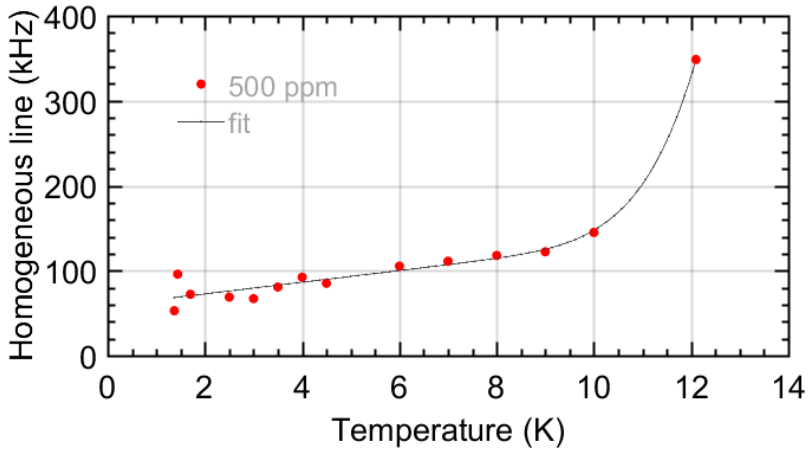


Figure 4.13: Optical homogeneous linewidth as a function of temperature is plotted for 500 ppm $Pr^{3+}:Y_2O_3$ ceramics. Continuous line is a fit to Eq.(4.2) that gives: $\Gamma_0 \approx 50$ kHz, $\alpha_{\text{TLS}} = 6.9$ Hz/K, and $\alpha_{\text{Orb}} = 1.4e7$ kHz.

leads to a broadening of the homogeneous line due to spectral diffusion. Second, electric charge noise due to fluctuating surface charges on the crystalline domains or oxygen vacancies can cause spectral diffusion due to the varying electric field at the position of the emitter [58, 77, 90]. The smaller crystalline domain size increases both the average electric field from surface charges experienced by the ions sitting in the volume and also the oxygen stoichiometry in the particles. Both these effects hence manifest in lower coherence times for the smaller nanoparticles.

The dependence of homogeneous linewidth on temperature is given by Eq. 4.2. Our measurement of the homogeneous linewidth of the ceramics

as a function of temperature are shown in Fig. 4.13. A fit to Eq. 4.2 gives $\Gamma_0 \approx 50$ kHz, $\alpha_{\text{TLS}} = 6.9$ kHz/K, and $\alpha_{\text{Orb}} = 1.4\text{e}7$ kHz. We can conclude from these values that the major contribution to homogeneous linewidth at the lowest temperature of 1.4 K is the dephasing due to electric charge noise. The contribution from oxygen defects can be minimized by diffusing more oxygen into the particles by annealing at higher temperatures as well as treating them to pure oxygen plasma [77]. Note that the value of α_{TLS} obtained here is much smaller than the one we obtained for $\text{Er}^{3+}:\text{Y}_2\text{O}_3$ nanoparticles, where it was $\alpha_{\text{TLS}} = 121.7$ kHz/K. This is expected because ceramics are closer than nanoparticles in their behaviour to bulk crystals, where TLS behaviour isn't observed as strongly.

Note that this behaviour could change for the nanoparticles, as both the coupling to surface charges and TLS increases with reduced crystalline domain size. A similar measurement would hence need to be done to quantify the contribution of each of these processes in the nanoparticles. Additionally, no dependence on the magnetic field was found for a maximum applied field of 1.5 T.

4.5.2 Spin coherence properties

With a nuclear spin $I = 5/2$, the hyperfine structure of Pr^{3+} consists of three doubly degenerate levels $\pm 1/2, \pm 3/2$ and $\pm 5/2$ in the ground and excited states. The energy level splitting of these hyperfine states in $\text{Pr}^{3+}:\text{Y}_2\text{O}_3$ was not known before this work. We hence begin by measuring this by spectral hole burning with a 500 μs long pulse followed by a weak frequency chirped pulse. The resulting holes and side-holes enable the identification of the level structure in the ground and excited state. As shown on the left in Fig. 4.14, we measure a hyperfine splitting of 10.4 MHz for $\pm 5/2 - \pm 3/2$ and 6 MHz for $\pm 3/2 - \pm 1/2$ in the ground state, and 1.4 MHz for $\pm 1/2 - \pm 3/2$ and 2.9 MHz for $\pm 3/2 - \pm 3/2$ in the excited state.

The coherence time of the ground state spin transitions $\pm 5/2 - \pm 3/2$ (at 10.4 MHz) and $\pm 3/2 - \pm 1/2$ (at 6 MHz) are probed by the two-pulse photon echo technique. To begin, we first induce a population difference between the two levels involved in the transition by optical pumping via

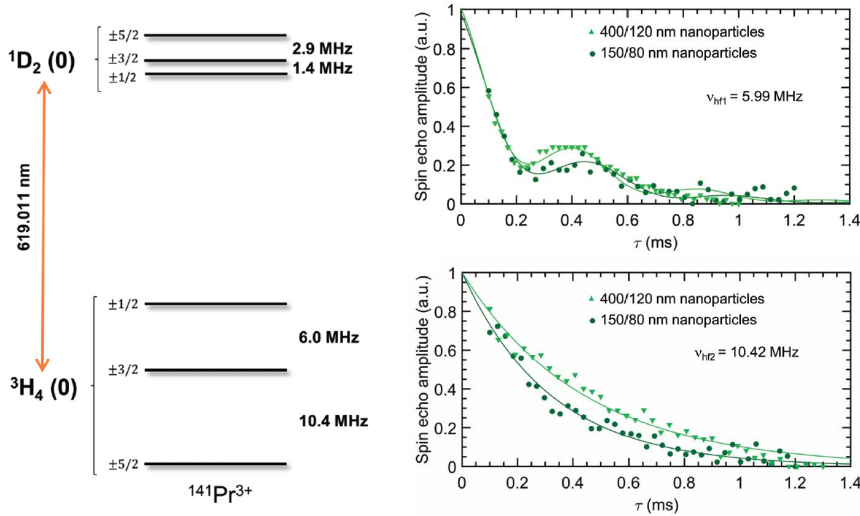


Figure 4.14: Hyperfine structure of $\text{Pr}^{3+}:\text{Y}_2\text{O}_3$ is shown on the left. The decay in echo amplitude for the hyperfine transition at 6 MHz and 10.4 MHz for both the investigated nanoparticles at 1.4 K and zero applied magnetic field is shown on the right.

the excited state. We then perform the two-photon echo technique, where the two pulses each consist of two-colour Raman pulses with a frequency difference matching that of the transition. After a time equal to the separation between the two pulses τ , the spin echo is transferred to the optical state with the help of an optical pulse, and detected using the heterodyne technique. The decay of echo amplitude as a function of τ for the two spin transitions at 6 MHz and 10.4 MHz for both 400 nm and 150 nm nanoparticles at 1.4 K and zero applied magnetic field is plotted on the right in Fig. 4.14. There is a clear modulation of the echo amplitude for the 6 MHz transition, which could be due to the removal of the degeneracy of the hyperfine level via super-hyperfine coupling to nearby nuclear spins.

The echo decay is hence described by

$$E = E_0 \exp(-2\tau/T_2) (1 + m \cos^2(\omega\tau/2)) \quad (4.7)$$

where m is the modulation amplitude and ω is the amplitude frequency. Fitting to this equation for the 6 MHz transition gives $T_2 = 680 \mu\text{s}$ ($\Gamma_h = 470 \text{ Hz}$) for the 400 nm nanoparticles and $T_2 = 640 \mu\text{s}$ ($\Gamma_h = 500 \text{ Hz}$) for the 150 nm nanoparticles. The modulation frequency was $\sim 2.5 \text{ kHz}$ for both. No such modulation was however observed for the 10.4 MHz transition, and further investigation is needed to identify the precise reason. The spin coherence time could hence be deduced by fitting to a simple echo decay, which gives $T_2 = 880 \mu\text{s}$ ($\Gamma_h = 360 \text{ Hz}$) for the 400 nm nanoparticles and $T_2 = 640 \mu\text{s}$ ($\Gamma_h = 500 \text{ Hz}$) for the 150 nm nanoparticles. Note that these values are higher than the ones measured in bulk $Pr^{3+}:Y_2SiO_5$ that have been used in demonstrations of quantum memories [108].

4.5.3 Single Pr^{3+} ion as a spin-photon interface

As discussed in Sec. 1.2, single rare-earth ions coupled to microcavities could enable efficient spin-photon interfaces that could be utilized in quantum networks. As Sec. 4.4 above details, one of the main requirements for a spin-photon interface is to produce indistinguishable photons. This requires $T_2 = 2T_c$, where T_2 is the coherence time of the optical state and $T_c = T_1/(C+1)$, where T_1 is the natural excited state lifetime and C is the Purcell enhancement given by Eq. 4.5. With the values we have measured here, we have $T_1 = 140 \mu\text{s}$ and $T_2 = 1 \mu\text{s}$ for the smallest nanoparticles of 150 nm diameter, that is $T_2 \ll 2T_1$. We would hence need significant Purcell enhancement via coupling to cavities with very high finesse F and low radius of curvature R and length L to achieve indistinguishable photons.

However, the total scattering loss introduced by a nanoparticle of diameter 150 nm at the wavelength of 619 nm is $2B = 8600 \text{ ppm}$, which is too high to be integrated into any high finesse cavity. We would hence need to reduce the diameter of the nanoparticle. At a diameter of 60 nm, we have $2B = 35 \text{ ppm}$, which would be low enough to integrate into cavities with total transmittivities of even 100 ppm, which corresponds to finesse

$F = 60,000$. Considering a more realistic case with $F = 20,000$, a plano concave cavity with $R = 20 \mu\text{m}$ and $L = 2 \mu\text{m}$, and using $\zeta = 0.057$ as we have measured here, we get $C = 70$ which corresponds to $T_c = 2 \mu\text{s}$. To have indistinguishable photons, we would need $T_2 = 4 \mu\text{s}$. While this is higher than the values we have measured in this section for nanoparticles with 150 nm diameter, higher values of T_2 have been measured for $Eu^{3+}:Y_2O_3$ in small nanoparticles [77, 90]. Hence, achieving the desired coherence in $Pr^{3+}:Y_2O_3$ nanoparticles with an average diameter of 60 nm could be possible in the near future.

Another important capability a spin-photon interface should have is to possess long-lived states for storage. As we have measured in this section, the spin coherence times for all $Pr^{3+}:Y_2O_3$ nanoparticles approach 1 ms at a temperature of 1.4 K, which is highly desirable. This coherence time could be further improved significantly by using dynamical decoupling techniques, as has been demonstrated using only optical pulses for Eu^{3+} [59]. When combined with optical frequency conversion of the emitted photons to telecom wavelengths, as has already been demonstrated [104], single Pr^{3+} ions coupled to high-finesse optical microcavities could be a very promising platform for quantum network applications.

Chapter 5

Dynamic control of Purcell-enhanced emission

In this chapter, we demonstrate the dynamical control of the Purcell enhanced emission of a small ensemble of erbium ions in a single nanoparticle coupled to a fiber-based microcavity. The $\text{Er}^{3+}:\text{Y}_2\text{O}_3$ nanoparticles are doped at 200 ppm atomic concentration and an average diameter of 140 nm, while the fiber microcavity has a finesse of 21,000 (see Chapter. 3 for more details). Using our experimental setup detailed in Sec. 5.2, we first demonstrate an average Purcell enhancement of 14 in Sec. 5.3. The decay is compatible with a multi-exponential model describing Purcell enhancement with an ensemble of ions that predicts that 10% of the ions experience an effective Purcell enhancement higher than 74. The model is discussed in detail in Sec. A.1. We then demonstrate in Sec. 5.4 that the resonance frequency of our cavity can be tuned on a time scale of hundred microseconds, which is 100 times faster than the spontaneous emission lifetime of the ions. This is achieved by physically moving the fiber mirror with sub-nanometer precision using a piezoelectric device. Finally, we show in Sec. 5.4.2 that we can shape in real time the Purcell enhanced emission of the ions to control the emitted photons' waveforms, without perturbing the emitter. Our approach opens the door to a solid-state quantum node with the potential

of exhibiting quantum computing and communication capabilities all in a single device.

Results reported in this chapter were published in the journal *Nature Communications* [109]. Material in this chapter has either been suitably adapted from it where necessary or quoted verbatim.

5.1 Introduction

The coupling of a RE ion to a cavity with high Q/V would Purcell-enhance the emission of the RE ion, which would result in an efficient spin-photon interface as the emission from the RE ions is channelled into the cavity mode. However, a strong reduction of the optical lifetime also reduces the available time to realize quantum gates that rely on dipole-blockade mechanisms achieved by driving the emitter to the excited state [45]. One attractive solution to this problem is to decouple the emitters from the cavity when performing the quantum gates, and coupling it back to emit a single photon at a desired time. The ability to achieve a dynamic modulation of the Purcell factor would therefore be a key ingredient to achieve this type of quantum gates in a high efficiency spin-photon interface, as well as an essential tool to shape the emitted single photon waveform and to realize cavity enhanced non-destructive detection of photonic qubits [110]. Additionally, the dynamic resonance modulation also enables addressing inhomogeneously broadened ensembles of single emitters as multi-qubit registers.

The control of collective light emission from ensembles of atoms in free space has been demonstrated [111, 112]. Experiments towards the dynamic control of emission of the cavity enhanced spontaneous emission rate have been so far mostly performed with semi-conductor quantum dots featuring short optical and spin coherence time [113–116], with Raman schemes with single atoms [117] and ions [118], and by modifying the local optical environment of RE ion doped crystals [119, 120]. Related work on fast modulation of erbium ions emission has been performed recently, using electrical modulation of erbium-graphene interaction [121]. Although REIs

coupled to nanophotonic cavities have recently led to the detection and manipulation of single rare-earth ions [52, 53, 55, 56], there has yet to be a demonstration of the dynamic modification of spontaneous emission.

5.2 Experimental setup

Our setup involves a small ensemble of erbium ions in a single nanoparticle coupled to a fiber-based microcavity. The $\text{Er}^{3+}:\text{Y}_2\text{O}_3$ nanoparticles are doped at 200 ppm atomic concentration and an average diameter of 140 nm, while the fiber microcavity has a finesse of 21,000 (see Chapter. 3 for more details). Our setup allows to move the fiber around the mirror and localize the nanoparticles, and to set the separation between the fiber and the mirror to form a cavity on resonance with the ions (see Sec. 3.3 for details). Nanoparticles are located by scattering loss microscopy (see Sec. 3.5 for details) [66, 86, 87]. We use a nanoparticle with a radius of 91(1) nm (see Fig. 5.4(a)) adding a total intra-cavity loss of $2 \times 43(2)$ parts-per-million (ppm) per round trip. It contains close to 11,000 erbium ions in the measured C_2 crystallographic site (see Sec. 3.1.2 for details). The empty cavity has a finesse of 21,000, which is reduced to 16,000 in the presence of the nanoparticle. For cavities as short as 3 μm we can expect a maximal Purcell factor $C_{\text{max}} = 208$, which then reduces to 149 for a cavity length of 6 μm as used in the work presented here.

The optical setup is shown in Fig 5.1. It allows us to perform resonance excitation and detection both via the optical fiber. The 1535 nm laser is used to excite the ions and the 790 nm laser to stabilize the length of the cavity. An acousto-optic modulator (AOM) in a double pass configuration is used to ‘pulse’ the excitation laser. A single pass AOM operates as excitation/detection ‘router’. During excitation, the router AOM is off and the excitation light is directed to the cavity while most of the reflected light is directed back to the same channel. During detection, the router AOM is on and the spontaneous emission from the ions is deflected towards an InGaAs single photon counter (detection efficiency 10 %). A ‘filter’ double pass AOM after the router is used to add additional protection

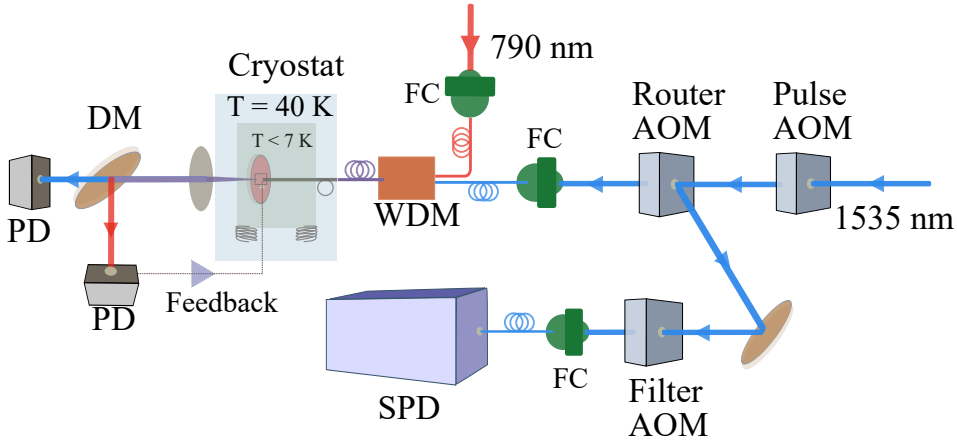


Figure 5.1: A 1535 nm laser is used to excite the ions and a 790 nm laser to stabilize the length of the cavity. The two lasers are combined using a wavelength division multiplexer (WDM). A set of acousto optic modulators (AOM) are used to create pulses from the CW excitation laser, to route the excitation light to the cavity and the cavity photons to the detector, and to suppress the excitation light to the single photon detector (SPD) by 60 dB (InGaAs, detection efficiency 10 %) during excitation. DM is a 780/1535 nm dichroic mirror, PD are continuous avalanche photo-diodes (APD) for cavity length stabilization and transmission monitoring.

(60 dB) to the single photon detector during excitation. A wavelength-division multiplexing (WDM) and dichroic mirrors (DM) both for 780/1535 are used for merging the light directed onto the cavity and to separate the transmitted light. The transmitted light is then directed to continuous APDs (PD) for cavity length stabilization and transmission monitor. In our setup, the probability for a photon emitted in the cavity mode to reach the single photon detector is 2.8 % and the coupling efficiency between the fiber and the cavity mode is calculated to be 55% (see Sec. 5.5).

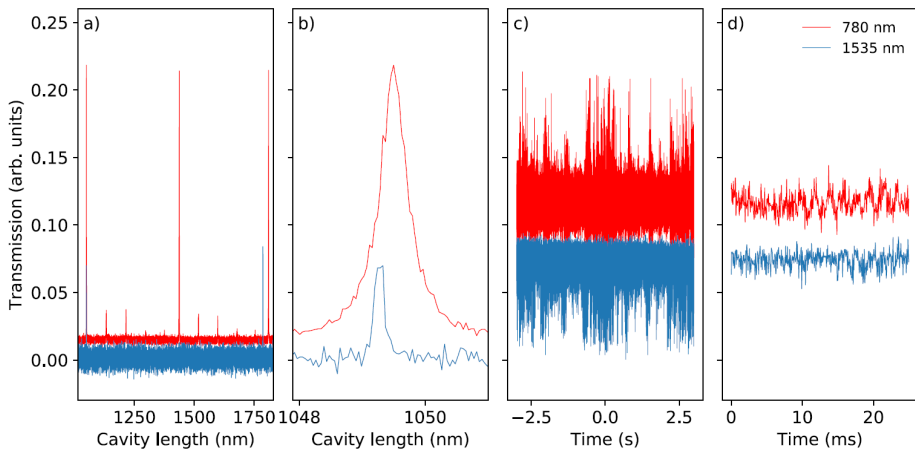


Figure 5.2: a) 780 nm (red) and 1535 nm (blue) cavity transmission as function of cavity length. For this measurement, the cavity finesse at 780 nm and 1535 nm was 700 and 5,000 respectively. b) Zoom in of (a) on the fringe used to stabilize the cavity length. c) Transmission during 5 seconds while the cryostat is on. The cavity length is actively stabilized to the side fringe of the 780 nm transmission while it is on resonance at 1535 nm. By calculating the standard deviation of the 790 nm transmission, we infer a cavity stability of 30 pm d) Zoom in of (c) on 30 milliseconds over which the cavity stability is the highest.

5.2.1 Cavity stability

To ensure the highest Purcell factor, a cavity length stability smaller than $\frac{\lambda}{2F} \approx 40$ pm is required. As detailed in Sec. 3.3, we have built a compact and passively stable nano-positioning platform which is robust against the high frequency noise coming from the closed-cycle cryostat such that active stabilization in the low frequency domain, i.e., below 1 kHz, is enough to stabilize the cavity. We use a second laser at 790 nm to actively stabilize the

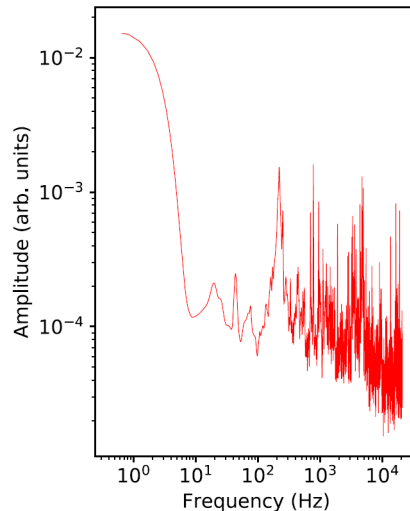


Figure 5.3: Fast Fourier transform of a typical 790 nm transmission signal when the cavity is lock. The dominant noise resides in the 150 – 300 Hz frequency domain.

length of the cavity on an arbitrary point on the transmission fringe. The coating is designed to have a finesse of 2,000 around 790 nm and such that there is a red mode close by to all 1535 nm resonances for cavity lengths in the 2–20 μm range.

Fig. 5.2(a) shows a transmission scan at 1535 nm and 790 nm while scanning the cavity length by close to 1 μm . For this particular measurement, the finesse F of cavity at 790 nm is 700 and at 1535 nm is 5,000. To stabilize the length of the cavity, we fine tune the wavelength of the 790 nm laser such that the maximum of the 1535 nm transmission peak overlaps with the middle of the 790 fringe (see Fig. 5.2(b)). Then, the transmission of the red laser is used to monitor cavity drifts and feedback is applied to the piezoelectric crystal to keep this signal at a constant level (side of fringe lock). Fig. 5.2(b) and (c) show the transmission of both lasers as function of the time while the feedback system is on for the whole cryostat cycle.

Fig. 5.3 shows a Fast Fourier Transform of the 790 nm transmission signal when the cavity is locked. The dominant noise resides in the 150 – 300 Hz frequency domain. Note that this is a limiting factor for our cavity stability, as the first eigenfrequency of our setup is close to 1.7 kHz.

We estimate the cavity stability using both the 790 nm and the 1535 nm transmissions and by modelling the cavity displacement by a single-frequency sinusoidal as $\delta(t) = A \cos(t \cdot 2\pi\nu)$ where ν is set to 200Hz, that is, the main frequency component of the 790 nm transmission signal, and A corresponds to the displacement amplitude. Then, the cavity transmission $T(t)$ as function of time can be calculated as:

$$T(t) = T_{\max} \cdot \mathcal{L}(t) = T_{\max} \cdot \frac{(\Delta/2)^2}{(\delta(t) + \delta_0)^2 + (\Delta/2)^2} \quad (5.1)$$

where \mathcal{L} is the Lorentzian spectral line shape of the cavity, δ_0 is the detuning from the center of the line, T_{\max} is maximum of the transmission and $\Delta = \frac{\lambda/2}{F}$ is the full width at half maximum (FWHM).

We then calculate A for both the 790 nm and 1535 nm fringes such that the calculated standard deviation (STD) for long times matches the measured values. Finally, we assess the root mean square (RMS) cavity stability as $\frac{A}{\sqrt{2}}$. For the 790 nm fringe, $\delta_0 = \Delta_{790}/2$, that is, the cavity is stabilized on the side of the fringe at half maximum, and the estimated RMS cavity stability is 31 pm. For the 1535 nm fringe, $\delta_0 = 0$, that is, the cavity is stabilized at the center of the fringe, and the estimated RMS cavity stability is 37 pm. We attribute the discrepancy to a larger uncertainty in the finesse of the 1535 nm mode. The 1535 nm fringes for the finesse measurement were not recorded with high enough resolution, and the obtained value of 5,000 is therefore a lower bound.

In Fig 5.2(c), we can identify time intervals which show significantly smaller signal dispersion, this interval corresponds to the quietest part of the cryostat cycle, which is close to 500 ms. Fig 5.2(d) corresponds to a zoom in of 30 milliseconds over which the cavity stability is the highest, for which we estimated RMS cavity stability of 21 pm and 31 pm when calculated using the 780 nm and the 1535 fringes respectively.

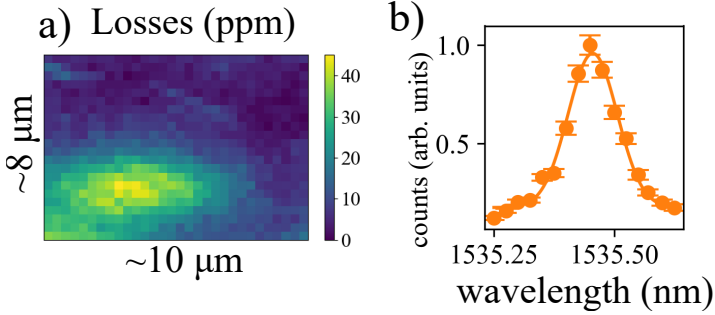


Figure 5.4: (a) Map of scattering loss introduced by a single nanoparticle when scanning the cavity mode across it. (b) Measurement of the inhomogeneous line of the ${}^4I_{15/2} - {}^4I_{13/2}$ transition. The solid line is a Gaussian fit, yielding a full-width-half-maximum linewidth of 15(2) GHz (error bars represents one standard deviation).

However, for the measurements presented in this chapter the stability is lower and typical values between 50 and 75 pm RMS were recorded. In the following sections, we will assume a cavity stability of 62.5 pm RMS, consistent with most of our measurements. The reason for that is not a fundamental limitation. The high stability reported in this section was recorded in the first assembly of the positioner, while for the data shown in the rest of this chapter the positioner was re-assembled several times. A possibility exists that during the subsequent assemblies a component was not optimally placed resulting in a degraded stability.

5.3 Measurement of Purcell enhancement

We begin by first performing resonant cavity spectroscopy of the ${}^4I_{15/2} - {}^4I_{13/2}$ transition with an input power (in the input fiber) of $2.4 \mu\text{W}$. We excite the ions for $300 \mu\text{s}$, then wait for $50 \mu\text{s}$ to ensure the pulse AOM is completely switched off, and collect light for 5 ms. Fig. 5.4(b) shows the normalized counts in the detection window as a function of the excitation wave-

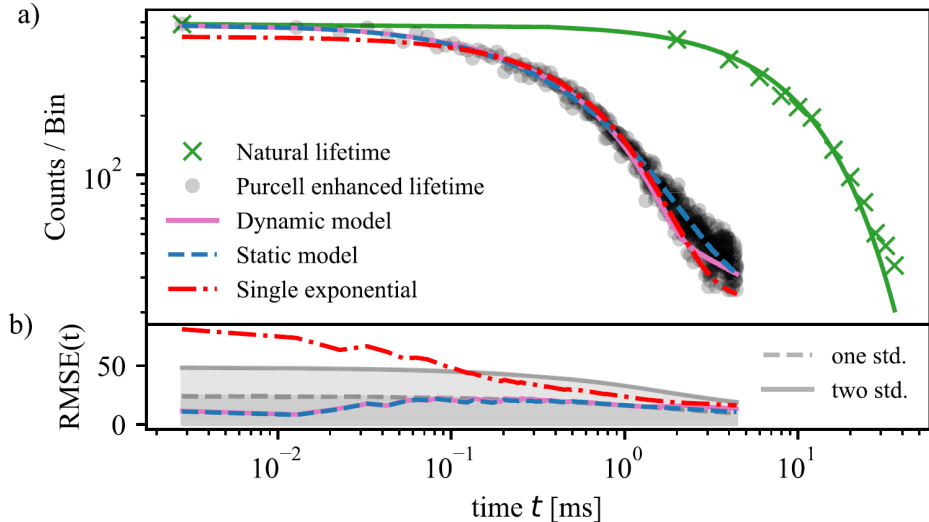


Figure 5.5: Purcell enhanced lifetime measurements. (a) Black points and green crosses correspond to the natural and Purcell enhanced lifetime measurements. Dash-dotted red line: Single exponential fit. Solid magenta and dashed blue line are the dynamic and static model respectively. (b) Gray lines correspond to one and two standard deviation calculated by summing all the counts in the detection window $[t_0, t]$ of the Purcell enhanced lifetime measurement (black points), where t_0 is the time at which the photon counting is started, and considering Poissonian counting statistics. Root-mean-square error (RMSE) of the single exponential, the static and the dynamic models, also calculated as function of the detection time window. The single exponential fit deviates by more than two stand deviations at earlier times, while the model and the reconstructed decaying curve stay below this threshold.

length. We fit it with a Gaussian profile and extract a FWHM linewidth of 15(2) GHz centered at 1535.42 nm.

When coupling an emitter to a cavity the emitter's lifetime is reduced to $T_c = T_1/(C + 1)$, where T_1 is the natural lifetime and C is the effective Pur-

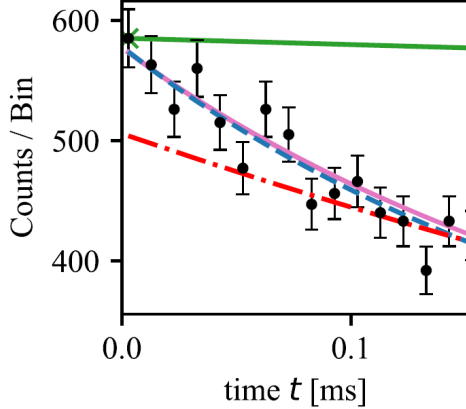


Figure 5.6: Zoom of the first 150 μs of the plot shown in Fig. 5.5. Error bars represent one standard deviation calculated from Poissonian counting statistics.

cell factor. Additionally, the collection efficiency of the cavity mode is given by $\beta = C/(C + 1)$. To measure Purcell enhancement, we fix the frequency of the laser to be in the center of the line and perform lifetime measurements (input power of 11 μW). Fig. 5.5(a) shows two data sets. Black points and green crosses correspond to the Purcell enhanced and natural lifetime measurements respectively. Single exponential fits reveal Purcell enhanced and natural lifetimes $T_c = 0.74(1)$ ms and $T_1 = 10.8(3)$ ms (see Sec. 5.4 for a description of the procedure to extract the natural lifetime). We calculate the effective Purcell factor $C = C_0\zeta = T_1/T_c - 1 = 14$ (1) which yields $C_0 = 108(3)$ with $\zeta = 0.13$ the branching ratio of the transition. We then estimate the probability for an ion to emit in the cavity mode $\beta = C/(C + 1) = 93.2\%$.

Black points in Fig. 5.5 correspond to photons generated by a few hundred ions due to power broadening, and by decreasing the input power to 300 pW, a number as low as 10 ions could be detected with a signal-to noise ratio around 5 (see Sec. 5.5).

The single exponential fit does not describe well the data for the Purcell

enhanced case suggesting that emitters experiencing different enhancement contribute to the detected signal (see dash dotted red line in Fig. 5.5 and Fig. 5.6). To investigate this further, Dr. Bernardo Casabone, with the help of other authors, derived a model describing our experiment (see Sec. A.1). The model considers a maximum Purcell factor C_{\max} which is then reduced due to the randomly oriented dipole moment of the emitters, the finite extension of the particle [65] and fluctuations of the cavity resonance. From the model we can perform a dynamic and a static analysis. The dynamic approach is based on the probability of an ion to emit into the cavity mode which is proportional to

$$e^{-\int_0^t \frac{C(t')}{T_1} dt'} \quad (5.2)$$

where $C(t')$ is the experienced Purcell factor as function of time. The static approach starts by estimating the distribution of Purcell factors in the system $p(s = C/C_{\max})$, from which we reconstruct a decaying curve proportional to

$$\int_0^1 p(s) e^{-s t C_{\max}/T_1} ds \quad (5.3)$$

While the first method is a direct simulation of the experiment, which is sensitive to the frequency of the cavity vibration, from the second method we can obtain a distribution of Purcell factors and estimate the maximum enhancement present in the system (see Sec. A.1). The magenta and blue lines in Fig. 5.5 and Fig. 5.6 are the models following the dynamic and static analysis respectively when considering expected parameters from our system but reducing C_{\max} to 150 in order to obtain a satisfying description of the experimental data.

Fig. 5.7 shows the probability $P_{c>C}$ that a given ion experiences a Purcell factor c greater than C calculated from the estimated $p(s)$. From this model, we infer that 50% of the ions experience a Purcell factor larger than $C = 15$ consistent with the measured $T_c = 0.74(1)$ ms, and that at least 10% of the ions experience a Purcell factor larger than 74. The models describe the data with noticeably more accuracy than the single exponential (see RMSE calculations in Fig. 5.5(b)). In particular, they succeed

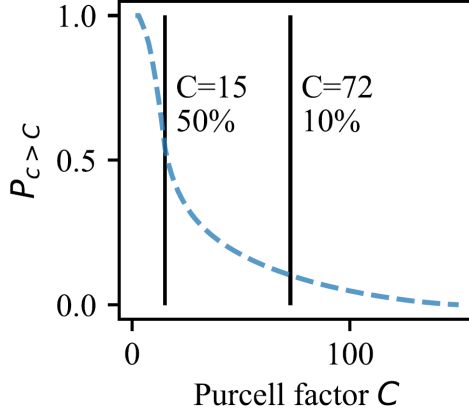


Figure 5.7: Estimated probability $P_{c>C}$ that a given ion decays with a Purcell factor c greater than C .

to reproduce the decay at early times, confirming the presence of Purcell enhancement larger than 15.

5.4 Cavity switching

We now explain our strategy to tune the cavity resonance in a time scale faster than the spontaneous lifetime. First, we set the 1535 nm excitation laser on resonance with the center of the inhomogeneous line of the ions. Then, we use a second laser at 790 nm to stabilize the length of the cavity. The 790 nm wavelength is tuned such that 50% transmission level of the positive slope overlaps with the center of the 1535 nm cavity resonance (see Fig. 5.8). By a fast change of the voltage offset V from V_p to V_n or vice-versa, and by switching the sign of the feedback action, we can stabilize the cavity to the positive and negative sides of the 790 nm fringe at will (the feedback is off during the transient phase). The voltage is varied as $\sin^2(\frac{\pi t}{2S_{790}})$ and the process happens during a time $S_{790} = 300 \mu s$ for our realization (see Sec. A.2). Between the two locking positions, the total

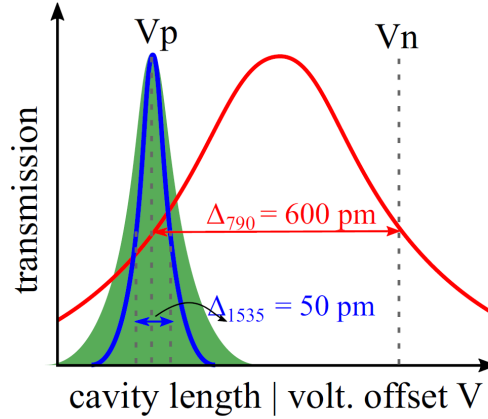


Figure 5.8: Scheme to stabilize the length of the cavity on/off resonance with the ions. The cavity length is controlled applying a voltage offset V that moves the fiber. For V_p , the transmission of the 790 nm locking laser is at the 50% level on the positive slope of the fringe (red curve), and on resonance with both the center of the inhomogeneous line of the ions (green area) and the 1535 nm excitation laser (blue fringe). For V_n , the fiber is displaced by $d_f = \Delta_{790} = 600$ pm with respect to the position of V_p . The transmission of the 790 nm locking laser is at the 50% level but on the negative slope, and both the excitation 1535 nm laser and the center of the homogeneous line are detuned by $12\Delta_{1535}$. The cavity length can be stabilized to the 50% level of either 790 nm fringe, for which the feedback sign has to be adequately set.

fiber displacement d_f corresponds to the full width at half maximum of the 790 nm cavity fringe, that is, $d_f = \Delta_{790} = \frac{790\text{nm}}{2F_{790}} \approx 600$ pm ($F_{790} \approx 700$, reduced due to the particle losses). This displacement is 12 times larger than $\Delta_{1535} \approx 50$ pm, such that the detuning between the erbium ions and the 1535 nm cavity is $\delta = 12\Delta_{1535}$. Using the Lorentzian linewidth of the cavity, one can estimate a maximum reduction of Purcell factor $C \propto \mathcal{L}(\circ) \approx 1/577$ and for the fluorescence count rate of $1/630$ [122] (see Sec. A.2 for all details).

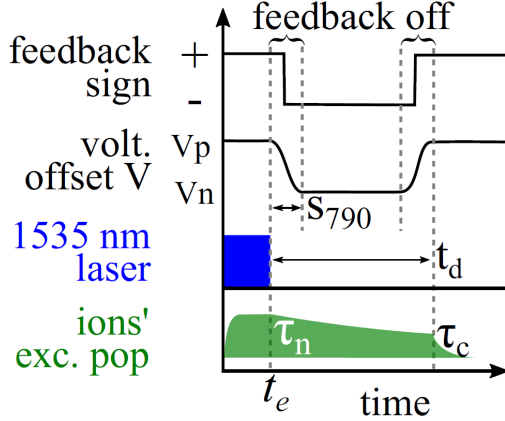


Figure 5.9: Sequence used to extract T_1 . First, V_p is applied for a time t_e and the 1535 nm resonance is driven. At a time t_e , the voltage is switched from V_p to V_n in a time S_{790} . The excited state population then decays at T_1 . After a time $t_e + t_d + S_{790}$, v_n is switched back to V_p . Feedback sign is set to positive (negative) for V_p (v_np), and feedback action is off in the transient stage of the voltage.

5.4.1 Measuring natural lifetime

In this section, we show how the cavity-switching technique detailed above can be used to extract the natural lifetime T_1 of a single nanoparticle while isolating the effect of the cavity from any other lifetime reduction process. We first set the cavity on resonance with the ions ($V = V_p$) and turn on the excitation laser at 1535 nm for $t_e = 300 \mu\text{s}$ (see Fig. 5.9). Immediately after, we detune the cavity ($V = V_n$) and start to collect photons. After a time t_d , we set the cavity back on resonance ($V = V_p$). Fig. 5.10 shows the counts as function of time for $t_d = 5, 16$ and 28 ms. As shown in Fig. 5.10, the total counts decreases while increasing t_d . When the cavity is off resonance with ions, the excited state population decays with the natural lifetime T_1 , and therefore less ions contribute to the detected signal for longer t_d .

In order to extract the natural lifetime, we repeat the measurements

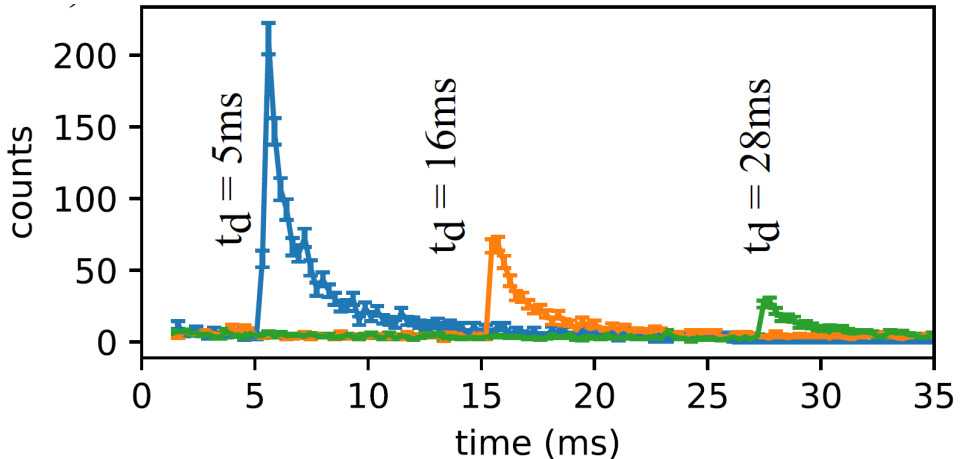


Figure 5.10: Counts recorded as function of time t for $t_d = 5, 16$ and 28 ms. Error bars represent one standard deviation of photon counts.

for t_d in a range from 1 — 28 ms and calculate the detected number of photons in the $[t_d - t_d + 5]$ ms time window (crosses in Fig. 5.5). A fit to a single-exponential gives a lifetime of $T_1 = 10.8(3)$ ms. Note that this value is almost 1.3 times shorter than the natural lifetime of these nanoparticles that we measured in Sec. 4.3.2. In an earlier work [66], the authors performed FDTD simulations on the emission lifetime of a dipole placed on a planar Bragg mirror and found that this reduces the excited state lifetime by up to a factor 1.3. This means that already the presence of a single mirror leads to some Purcell-enhanced emission rate. This prediction is hence in agreement with the reduction in natural lifetime observed for a nanoparticle when on a planar mirror compared to free space.

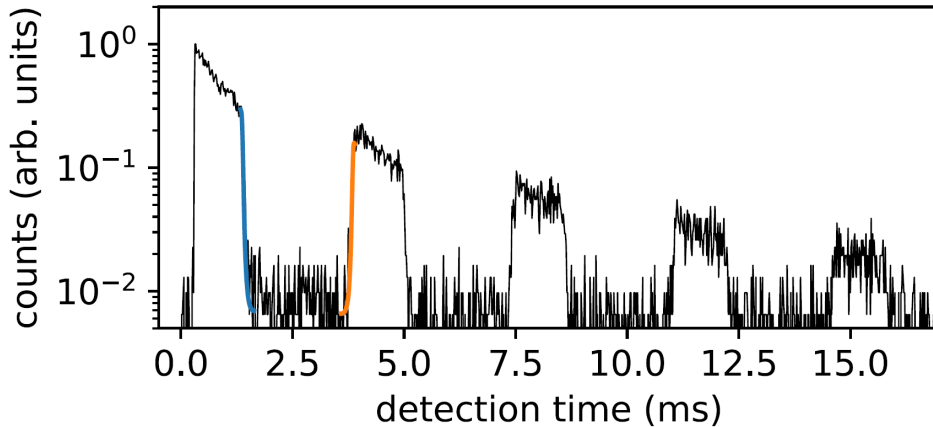


Figure 5.11: Counts as function of time when the voltage is alternated between V_p and V_n 5 times at intervals of 1 ms after excitation of the ions.

5.4.2 Dynamic switching

Finally, we demonstrate that this technique can be operated with a bandwidth high enough to shape the spontaneous emission of the erbium ions. Fig. 5.11 shows the recorded counts as function of the detection time while the cavity is tuned on (off) resonance for 1 ms (2.5 ms) 5 times. Fig. 5.12 shows a zoom-in of the falling and rising edges. The solid lines are a model using the piezo displacement, S_{790} and an effective 1535 nm cavity linewidth to account for cavity instability (see Sec. A.2 for details). Defining the switching time S_{1535} as the time needed to decrease the count rate by a factor of 10, we extract from the model $S_{1535} = 85(15) \mu\text{s}$. This value is more than two orders of magnitude shorter than the natural population decay time, and a factor of 9 shorter than the Purcell enhanced decay time T_c of the ionic ensemble. For future experiments with single erbium ions (or with other ions with shorter lifetime), much higher Purcell factors and

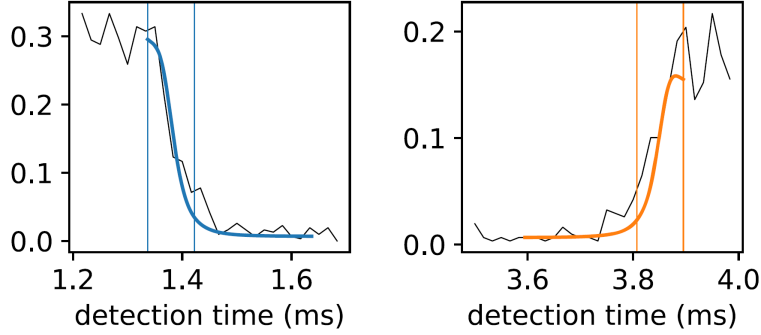


Figure 5.12: Zoom of Fig. 5.11 of the falling (left) and rising (right) edges are shown, revealing an average transition time of $S_{1535} = 85(15) \mu\text{s}$ for the falling edge and $87(16) \mu\text{s}$ for the rising edge.

consequently much shorter T_c will be required. Therefore, much shorter switching times are desirable. Several improvements on our experiments are possible to decrease S_{1535} . First, the current measured value is slower than the expected time of $67 \mu\text{s}$, which can be explained by the limited cavity stability.

Improvements on the cavity stability will therefore directly impact S_{1535} . Another possibility is to increase the finesse of the cavity at 1535 nm (and therefore decrease Δ_{1535}), as also required for increasing the Purcell factor. Finally, the switching time S_{790} could be decreased by designing a system with higher mechanical eigen frequencies or by iterative learning algorithms to minimize added noise. Altogether, we estimate that values of S_{1535} of a few microseconds could be achievable by combining these improvements.

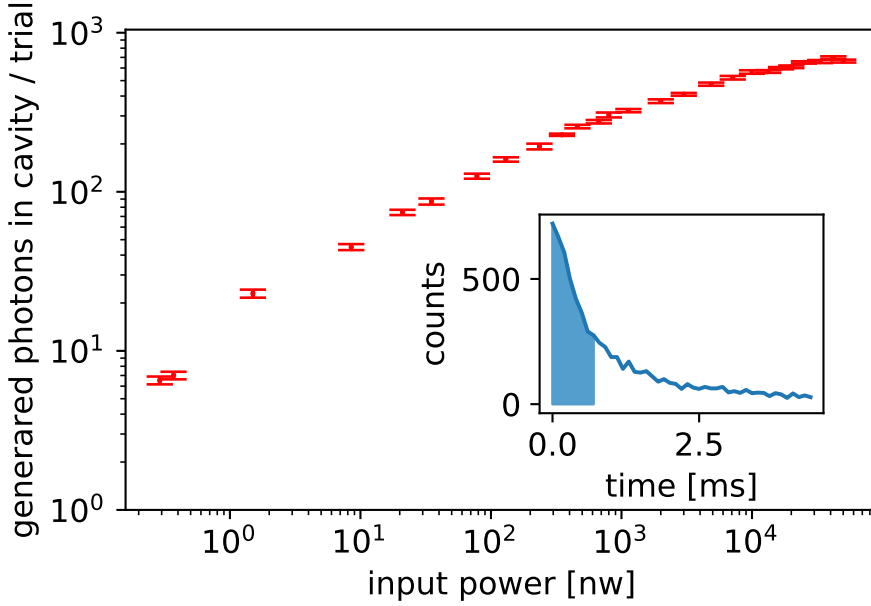


Figure 5.13: Number of photons generated in the cavity mode as a function of the excitation power before the cavity. Excitation pulse length is $500 \mu\text{s}$. Error bars represent one standard deviation of photons counts. The inset shows the detection window $[0 - T_c]$, with $T_c = 0.7 \mu\text{s}$.

5.5 Number of ions

In this section we specify the efficiencies of our setup and the sensitivity of our setup to a single ion. The probability p_{det} to detect a photon generated in the cavity mode is given by (see Sec. 3.2.3 for details):

$$p_{det} = \eta_g \times \eta_{esc} \times \epsilon \times \eta_{det} \quad (5.4)$$

where η_g is the proportion of the single photon in the detection time window, η_{esc} is the probability of the photon leaving through the fiber-mirror,

ϵ is the mode matching between the fiber and the cavity mode, and η_{det} is the efficiency to detect a photon once it is collected in the fiber, which includes the detector efficiency.

For our cavity, $\eta_{esc} = 0.25$ when detecting via fiber and when the particle is aligned to the cavity mode, $\eta_{det} = 0.03$, and $\eta_g = 0.63$ for a detection time window $t_{det} = [0 - T_c]$ where T_c is the Purcell enhanced lifetime. We theoretically calculate that $\epsilon < 0.60$. The value of ϵ is a higher bound because errors such as centering error between the core of the fiber mode and that of the cavity mode as well as angular misalignments between the two modes can lower it. All together then results in $p_{det} = 0.0028$.

Fig. 5.13 shows a measurement of the number of photons generated in the cavity as a function of the excitation input power at the input of the cavity. For an input power of 7 nW as in Fig. 5.5, the detected signal corresponds to 40 intra cavity photons generated by 80 ions (an ion is excited with at most 50% probability). For the first data point of Sec. 5.13 with input power of 330 pW, the detected signal corresponds to 5 intra cavity photons generated by 10 ions.

In order to detect a single ion, we need to compare the probability of detecting a photon p_{det} with the probability of detecting noise in the same time window t_{det} . We define the signal to noise ratio as $S/N = \frac{p_{det}}{p_n}$, where p_n is the background probability in the detection window t_{det} , in our case mostly due to the dark-count rate of the single photon detector (10 Hz). We then calculate

$$S/N = \frac{p_{det}}{T_c} \times \frac{1}{10 \text{ Hz}} = 0.5. \quad (5.5)$$

This means that the number of photons that must be generated in the cavity to achieve a $S/N = 1$ is equal 2, assuming $\epsilon = 0.60$. If ϵ is smaller than this value, then the S/N value would decrease further. Since we excite incoherently, each ion can generate 0.5 photons on average. To reach a $S/N = 1$, we therefore need to detect the fluorescence from four ions, which is not sufficient to reach high-fidelity detection of a single ion with this setup.

5.6 Conclusion

In conclusion, in this chapter we have demonstrated the dynamical control of the Purcell enhanced emission of a mesoscopic ensemble of erbium ions confined in a nanoparticle embedded in an open fiber based microcavity. By controlling the position of the fiber mirror, we have shown that we can control the cavity resonance and therefore the Purcell factor at a rate more than 100 times faster than the natural decay rate of the ions with the potential of reaching microseconds switching times. By varying the speed at which the fiber is displaced during the switching process, our setup would allow arbitrary shaping of the temporal waveform of the emitted photons. Combined with single ion addressing, this ability will enable the generation of fully tunable narrowband single photons, and provides a route to quantum processing using single rare-earth ions.

Chapter 6

Detection of a single erbium ion

In this chapter, we report on the detection of single erbium ions in $\text{Er}^{3+}:\text{Y}_2\text{O}_3$ nanoparticles coupled to a fiber micro-cavity. We begin by detailing the experimental setup in Sec. 6.1, which includes several improvements to the setup that was used in Ch. 5 so as to enable higher sensitivity to single Er^{3+} ions. We also estimate relevant experimental parameters to help understand the behaviour of the coupled emitter-cavity system including the expected maximum Purcell factor as well as the escape efficiency of a photon generated in the cavity. All the obtained results are reported in Sec. 6.2 including the Purcell enhanced lifetime of a single ion and its power broadened frequency spectrum. We also perform a measurement of the $g^{(2)}$ of the emitted photons and illustrate how it is limited by the signal to noise ratio. Sec. 6.3 concludes the chapter with a summary of all the results.

The measurements presented in this chapter were done together with Eduardo Beattie, who is a PhD student on the project. A manuscript is currently being prepared for submission to a peer-reviewed journal [123].

6.1 Experimental setup

The $\text{Er}^{3+}:\text{Y}_2\text{O}_3$ nanoparticles used for the experiments in this chapter are synthesized using the same procedure as detailed in Ch. 4, except that the doping is done at 20 ppm rather than 200 ppm. In a nanoparticle with a diameter of 140 nm, we estimate that we should have ~ 750 Er^{3+} ions in site 1. The inhomogeneous line in this sample was previously measured to be centered at 1535.49 nm with a FWHM of 6.3 GHz. This gives us a spectral density of ~ 1 ion/10 MHz at the centre of the inhomogeneous line. The temperature of the mirror holder is measured to be 6.5 K (see Sec. 3.3), where the homogeneous linewidth of the ions is expected to be 3 MHz (see Sec. 4.3.3). It should hence be possible to spectrally resolve individual Er^{3+} ions close to the centre of the inhomogeneous line.

The fiber mirror has a radius of curvature $R = 65 \mu\text{m}$ with the same dielectric coating as detailed in Sec. 3.2. The planar mirror is the second generation with lower transmissivity that is described in Sec. 3.2.5. The resulting micro-cavity has a finesse of 44,000 at 1535 nm and 2,200 at 790 nm. It should simultaneously result in a higher Purcell factor C and a higher escape efficiency η_{esc} for the photons than the previous generation of cavities. However, after the preparation of nanoparticles on the planar mirror the maximum finesse drops to $\sim 35,000$, indicating that the sample preparation introduces additional losses.

The microcavity setup was mounted on the second iteration of the nanopositioner. This provided for a cavity stability of ≈ 13 pm in the quiet part of the cryostat (see Sec. 3.3), where the experiment was conducted. The value of stability is smaller than the FWHM of the empty cavity of $\lambda/2F \approx 27$ pm at a finesse of $F = 28,000$.

The optical setup is similar to the one shown in Fig 5.1 in Ch. 5. Both excitation and detection is performed using the fiber mirror of the micro-cavity. A set of three acousto-optic modulators (AOMs) in a double pass configuration are used to ‘pulse’ the 1535 nm laser, while one AOM in single-pass configuration operates as excitation/detection ‘router’. The photons collected from the fiber mirror are directed with an efficiency of 44 % to superconducting nano-wire single-photon detectors (SNSPDs), which have

a detection efficiency of 80 %. The efficiency to detect a photon once it is collected in the fiber is then $\eta_{det} = 35$ %.

6.1.1 Experimental parameters

Using the fine-positioning piezos installed on the fiber, we locate a nanoparticle that introduces a total intra-cavity loss of $2B = 90$ ppm at the operating cavity length of $L = 8.5$ μm . This corresponds to a diameter of ≈ 185 nm, which is slightly larger than the average diameter of our nanoparticles. The effective finesse at the particle hence reduces to $\approx 20,000$. The maximum Purcell factor we can expect with this finesse, given $R = 65$ μm and $L = 8.5$ μm , is $C = 148$. Note that this value of C is lower than the one in Ch. 5 mainly because the cavity length used here is almost a factor 2 higher.

The mode-matching between the fiber and cavity mode is measured to be $\epsilon \geq 0.18$. This is a lower bound on ϵ because it is estimated based on the observed transmission after the micro-cavity, but any additional losses in the transmission path to the detector as well as imperfect alignment onto the detector could result in a lower estimate. Nonetheless, the measured value is much lower than the maximum theoretically calculated value of 0.71. The measured value of ϵ could be further limited due to experimental imperfections such as centering error between the core of the fiber mode and that of the cavity mode as well as angular misalignment between the two modes, which are ignored in the theoretical estimate.

With the transmissivity of the fiber mirror $T_f = 100$ ppm, and all other losses amounting to 314 ppm, the efficiency with which a photon generated inside the cavity escapes through the fiber-mirror can then be calculated using Eq. 2.23 to be $\eta_{esc} = 0.32$. Defining the efficiency with which a photon generated inside the cavity is collected into the fiber as $\eta_{out} = \eta_{esc} \times \epsilon$, we get $\eta_{out} \geq 0.058$. The efficiency with which a photon that is collected in the fiber is detected is measured to be $\eta_{det} = 0.35$, which includes both the transmission efficiency of the photon as well the efficiency of the detector. Note that η_{det} is much higher than the one in Ch. 5 as we now employ superconducting nano-wire single-photon detectors (SNSPDs)

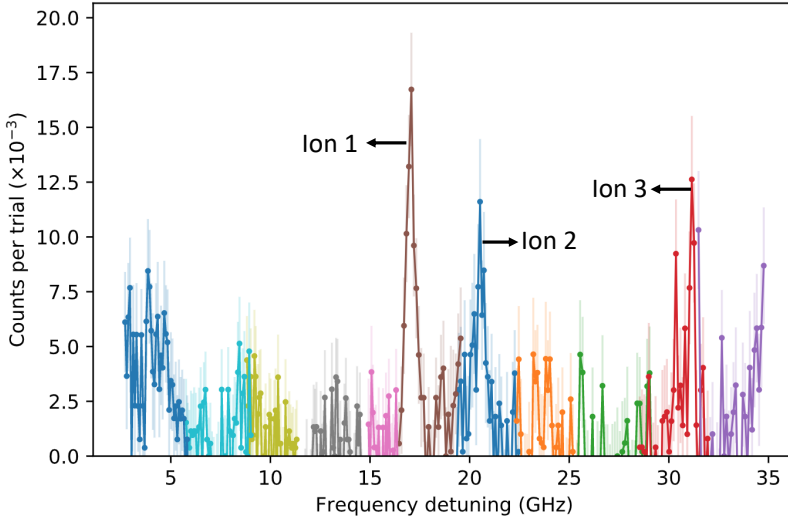


Figure 6.1: Counts received per trial as a function of laser frequency detuning from 1535.49 nm. Colours represent scans done in different spectral regions.

that have a detection efficiency of 0.8, which is a factor 8 higher than our previous detectors. The total probability to detect a photon generated in our cavity mode can then be calculated as $p_{det} = \eta_{esc} \times \epsilon \times \eta_{det} \geq 0.02$. If an ion is incoherently excited, then it generates on average 0.5 photons per excitation. Hence, the counts expected per excitation pulse is $0.5 \times 0.02 \geq 0.01$.

6.2 Results

The inhomogeneous linewidth of an ensemble of $\text{Er}^{3+}:\text{Y}_2\text{O}_3$ nanoparticles was previously measured to be centered at 1535.49 nm with a FWHM of 6.3 GHz. To resolve spectral features, we record counts as a function of the laser frequency, where the excitation and collection are, respectively,

200 μs and 1.8 ms. As we were unable to isolate any spectral features at the centre of the inhomogeneous line, we detune the laser frequency further from the centre. Fig. 6.1 shows counts received per excitation cycle as a function of laser frequency detuning from 1535.49 nm. The scan covers a detuning range of $\sim 5 - 30$ GHz and we can clearly identify three distinct spectral features within this range. The features appear much broader than the ~ 3 MHz we would expect at the given temperature. The spectral density at the centre of the inhomogeneous line would be too high to resolve ions with such broad linewidths, which might explain the large detuning necessary for these measurements.

6.2.1 Spectrum of a single ion

In this section, we investigate the feature identified as ‘Ion 1’ in Fig. 6.1 at a detuning of ~ 17 GHz. Fig. 6.2 shows the background subtracted counts per trial from Ion 1 as a function of laser frequency detuning from 1535.49 nm for three different mean intra-cavity photon numbers N_{ph} . N_{ph} is related to the input power P_{in} and to the cavity linewidth κ as $N_{ph} = 4P_{in}/(\hbar\omega\kappa)$. For our cavity, $\kappa = 2\pi \times 980$ MHz, which results in $N_{ph} = 5.25$ for an input power of 1 nW.

To extract the linewidth of the emitter at zero power, we recall from Sec. 2.3.1 that the power broadened linewidth of an emitter is given by

$$\Gamma_{pb} = \Gamma_h \sqrt{1 + S} \quad (6.1)$$

where Γ_h is the homogeneous linewidth of the emitter at zero power, and S is the saturation parameter. S is given by $S = \Omega^2/(\Gamma_1\Gamma_2)$, where Ω is the Rabi frequency of the emitter, Γ_1 is the rate of decay from excited to ground state and Γ_2 is the rate of de-coherence between the two states. Writing Ω in terms of the emitter-cavity coupling rate g and the mean intra-cavity photon number N_{ph} as $\Omega = 2g \sqrt{N_{ph}}$, we can re-write

$$S = \frac{4g^2}{\Gamma_1\Gamma_2} N_{ph} \quad (6.2)$$

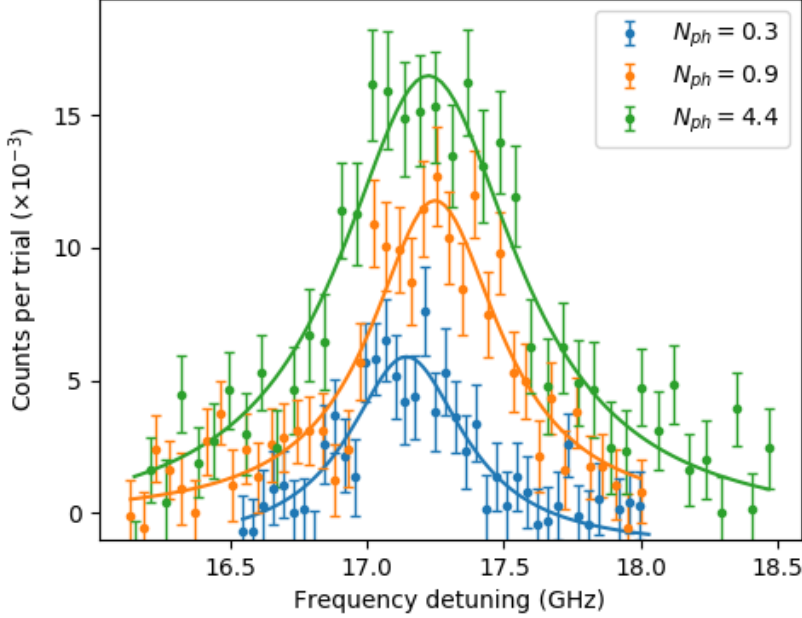


Figure 6.2: Counts received per trial from ‘Ion 1’ as a function of laser frequency detuning from 1535.49 nm for mean intra-cavity photon numbers $N_{ph} = 0.3, 0.9, 4.4$.

The linewidth of the emitter as a function of intra-cavity photon number N_{ph} is plotted on the right in Fig. 6.3. A fit to Eq. 6.1 gives $\Gamma_h = 380(70)$ MHz, which is almost two orders of magnitude larger than the expected linewidth. This could be due to several reasons. First, the local temperature of the nanoparticle could be much higher than the 6.5 K that is measured on the mirror holder. Based on the measurements done in Sec. 4.3.3 on the dependence of homogeneous linewidth on temperature, we can estimate that the emitters need to be at a temperature of ~ 16 K to have a linewidth of 380 MHz. Second, since this emitter is far detuned from the centre of the inhomogeneous line, it could be coupling to certain

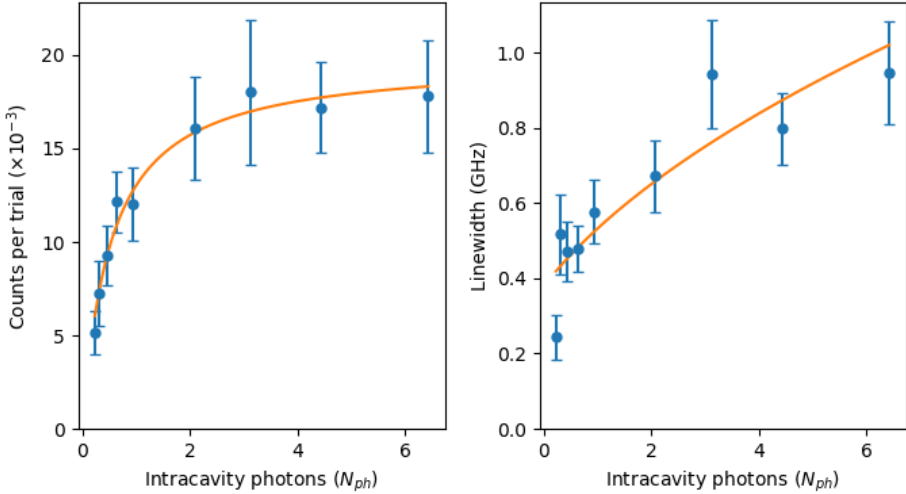


Figure 6.3: (left) Counts received per trigger as a function of mean intracavity photon number N_{ph} , where the counts saturate to $\approx 19(\times 10^{-3})$ at high N_{ph} . Orange line is a fit to Eq. 6.3. (right) Power broadened linewidth Γ_{pb} of the emitter as a function of N_{ph} . Orange line is a fit to Eq. 6.1, which gives $\Gamma_h = 380(70)$ MHz.

defects more strongly than the ones at the centre of the line. Further data on other emitters closer to the centre of the inhomogeneous line as well as emitters in other nanoparticles is needed to arrive at a definitive answer.

As discussed in Sec. 2.3.1, the steady state value of ρ_{ee} , which gives the probability to find the emitter in the excited state, is $\rho_{ee} = S/(2S + 2)$. For $S \gg 1$, this approaches 1/2. Including the efficiency to detect p_{det} , we can write the expected counts from a single emitter in the steady state per excitation cycle as

$$C_{det} = p_{det} \times \frac{S}{2(S + 1)} \quad (6.3)$$

The maximum counts obtained from the emitter as a function of N_{ph} are plotted on the left in Fig. 6.3. A fit to Eq. 6.3 gives $4g^2/(\Gamma_1\Gamma_2) = 1.9(2)$,

which means that we obtain $S = 1$ with $N_{ph} \approx 0.5$ ($P_{in} \approx 100$ pW).

We can also obtain $p_{det} = 0.039(1)$ from the fit, which is almost a factor 2 greater than the one we estimated in Sec. 6.1.1. This could be because our estimate of the mode-matching efficiency $\epsilon = 0.18$ is only a lower bound. For higher values of N_{ph} where $S \gg 1$, we can observe a clear saturation of counts at $\approx 19(\times 10^{-3})$ per trial, which is a signature of a single emitter.

6.2.2 Purcell enhancement of a single ion

To measure the lifetime of the ion, we begin by resonantly exciting the emitter for 200 μs before collecting the emitted photons for 1.8 ms. The collected photons are then passed through a 50:50 beam-splitter before being detected with an SNSPD in each output mode. Note that the beam-splitter is placed in the path of the photons so that the same measurement can then be used to measure the statistics of the photons in a Hanbury Brown-Twiss (HBT) experiment (see section below). Fig. 6.4 shows the cumulative counts recorded in the two SNSPDs. The data was recorded for ≈ 2 hours, and the counts are displayed as a histogram with a bin width of ≈ 16 μs . A fit to a single exponential gives a lifetime of $T_c = 225(3)$ μs and a cumulative background for both detectors of 18.44 Hz. The excited state lifetime in free space for an ensemble of nanoparticles was measured to be $T_1 = 13.68$ ms in Sec. 4.3.2. The effective Purcell factor C can then be calculated as $C = T_1/T_c - 1 = 60(1)$. Note that this value is a factor 4 better than the median value we measured in Ch. 5, where the first generation of the nano-positioner was used. However, it is lower than the expected maximum Purcell factor of 148. An imperfect overlap between the dipole of the emitter and the cavity polarization axis as well as residual cavity instability could result in the achieved value of C being lower than the expected value.

6.2.3 Measurement of $g^{(2)}(0)$

The presence of a single emitter can be confirmed by a measurement of the $g^{(2)}(0)$ of the emitted photons. As a single emitter can emit at most

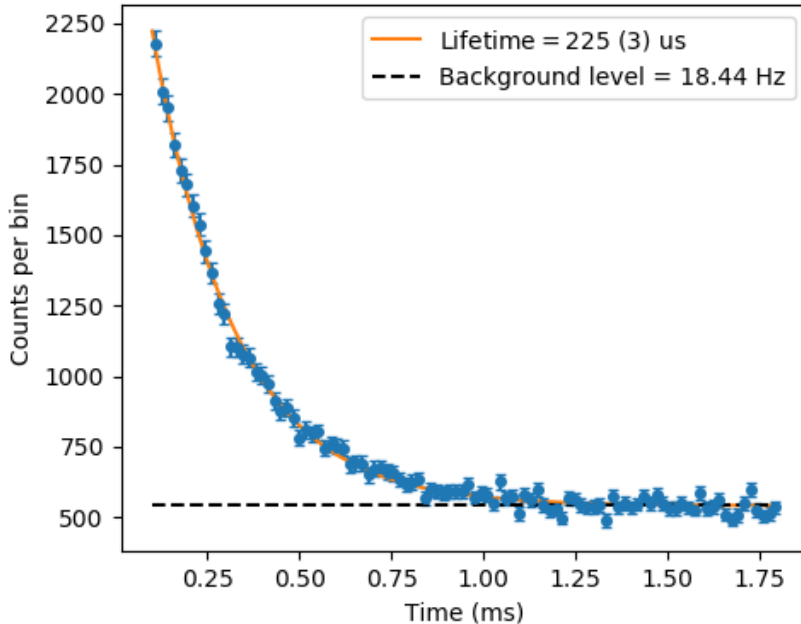


Figure 6.4: Purcell-enhanced lifetime of a single ion when the laser is on resonance with the ion at an input power of $P_{in} = 0.27$ nW ($N_{ph} = 1.4$). Fit to a single exponential gives a lifetime of $T_c = 225(3)$ μ s, which corresponds to a Purcell factor of $C = 60(1)$. The background is estimated to be 18.44 Hz from the fit.

a single photon, we expect $g^{(2)}(0) = 0$ for an ideal single emitter in the absence of any noise. We measure the $g^{(2)}(0)$ of the emitted photons by performing a Hanbury Brown-Twiss (HBT) experiment (see Sec. 2.3.2). The data used to compute the $g^{(2)}(0)$ is the same as shown in Fig. 6.4, but analyzed by looking at the counts in the two detectors separately. We receive $\approx 7 \times 10^{-3}$ counts from the emitter per detector per trial, while the background is constant at ≈ 9 Hz per detector. As the signal decays exponentially, we expect the signal to noise to also decay exponentially.

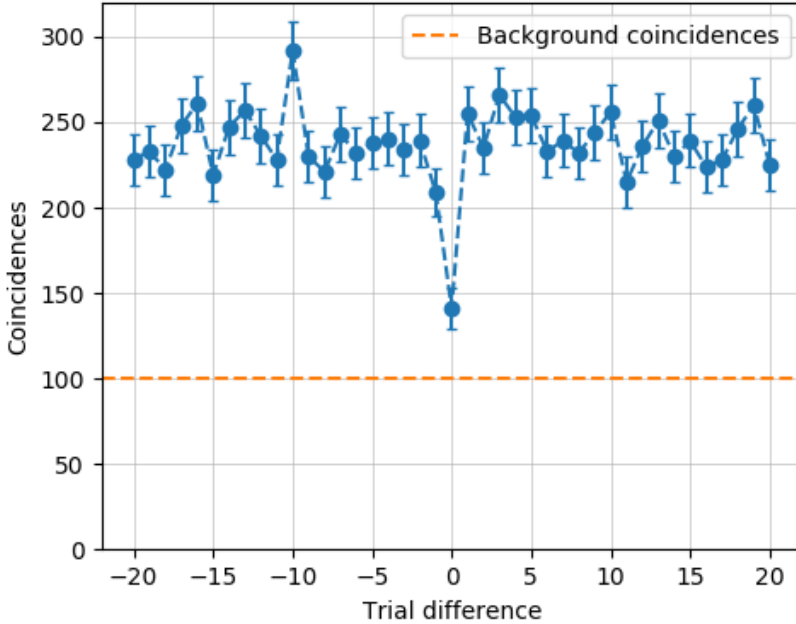


Figure 6.5: Coincidence counts as a function of trial difference. Orange dotted line indicates the expected background coincidences due to the presence of noise. We calculate an uncorrected $g^{(2)}(0) = 0.59(5)$, which after background subtraction gives $g^{(2)}(0) = 0.29(9)$.

We hence first consider only the initial $200 \mu\text{s}$ of the detection window, where the signal count-rate is estimated to be $\approx 18 \text{ Hz}$ per detector, which corresponds to a signal-to-noise ratio (SNR) of ≈ 2 in each detector in this window.

Recall from Sec. 2.3.2 that $g^{(2)}(0) = N_{1,2}/(N_1 \times N_2)$, where $N_{1,2}$ are the coincidences between modes 1 and 2 within a set time-interval, and N_1 and N_2 are the counts detected in mode 1 and mode 2 respectively within the same time-interval. Since our experiment is recorded in trials of excitation followed by detection, we can define the time-interval in which we look

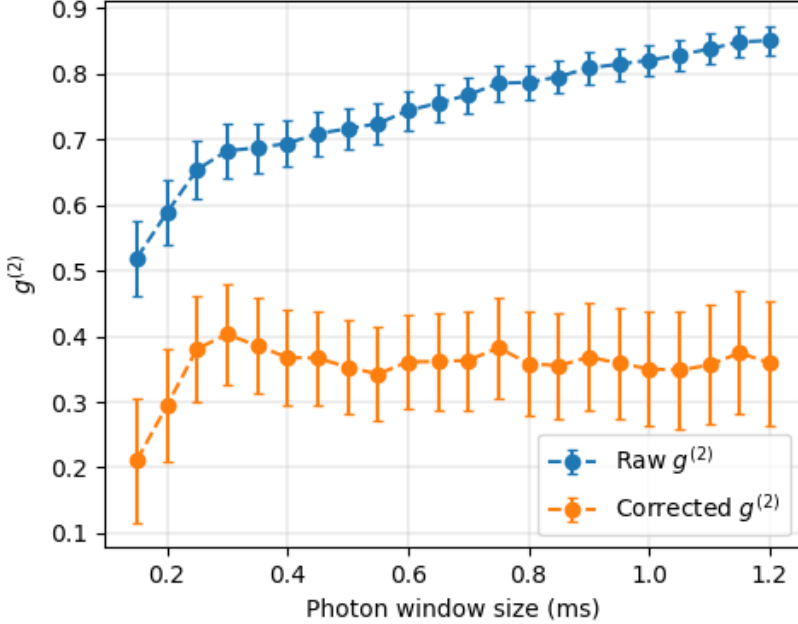


Figure 6.6: Value of raw and corrected $g^{(2)}(0)$ as a function of the window size of the photon considered.

for coincidences to be the time taken for each trial. In this case, $N_{1,2}$ is equal to the coincidences between the two detectors in the same trial while $(N_1 \times N_2)$ is equal to the coincidences between the two detectors in any other trial.

For a single emitter, the value of $g^{(2)}(0)$ depends on the SNR as [52]

$$g^{(2)}(0) = \frac{1 + 2 \times \text{SNR}}{(1 + \text{SNR})^2} \quad (6.4)$$

We can see that $g^{(2)}(0) \approx 0$ when $\text{SNR} \gg 1$. Using the data shown in Fig. 6.4, we initially consider only the first 200 μs of the detection window to estimate the $g^{(2)}(0)$. As mentioned above, $\text{SNR} = 2$ in this window, which

should result in a $g^{(2)}(0) = 0.55$. The coincidences we obtain between the two detectors as a function of the trial difference between them are plotted in Fig. 6.5. We can calculate the value of $g^{(2)}(0) = 0.59(5)$, which is close to the value we would expect given $\text{SNR} = 2$. As this value is already below 1, the input photonic state can already be classified as non-classical, which is strong evidence that it is emitted by a single emitter.

The orange dotted line in Fig. 6.5 indicates the expected background coincidences due to the presence of noise. It includes contributions from coincidences between signal-noise as well as noise-noise, where the expected value of signal and noise are extracted from the fit as described above. Subtracting the background coincidences gives a corrected value of $g^{(2)}(0) = 0.29(9)$. Emission from other detuned ions, such as Ion 2 (see Fig. 6.1), could be limiting the corrected value from reaching 0. We have also occasionally detected bursts of additional counts, which originate from the coupling of electronic noise to our detectors, that could be contributing to the coincidences in the same trial.

To further illustrate how SNR limits the uncorrected value of $g^{(2)}(0)$, we compute the value of $g^{(2)}(0)$ as a function of the window size of the photon considered. Fig. 6.6 shows the uncorrected (blue) as well as corrected (orange) value of $g^{(2)}(0)$ as a function of the window size of the photon considered. As expected, considering a longer portion of the photon results in an increase in the value of the uncorrected value of $g^{(2)}(0)$ due to an exponentially decaying SNR. However, the corrected value of $g^{(2)}(0)$ also seems to unexpectedly increase initially before saturating to a fixed value. Further measurements are needed to understand this behaviour.

6.2.4 Higher Purcell factors

Fig. 6.7 shows the Purcell-enhanced lifetime measured using the same microcavity but on a nanoparticle that is different from the one described above. The finesse when the fiber mirror was positioned on the nanoparticle was $\approx 18,000$ and the cavity length was set to $L = 3 \mu\text{m}$. The maximum Purcell factor we expect for a cavity with these parameters is ≈ 160 . Fitting the measured Purcell-enhanced lifetime to a single exponential results in

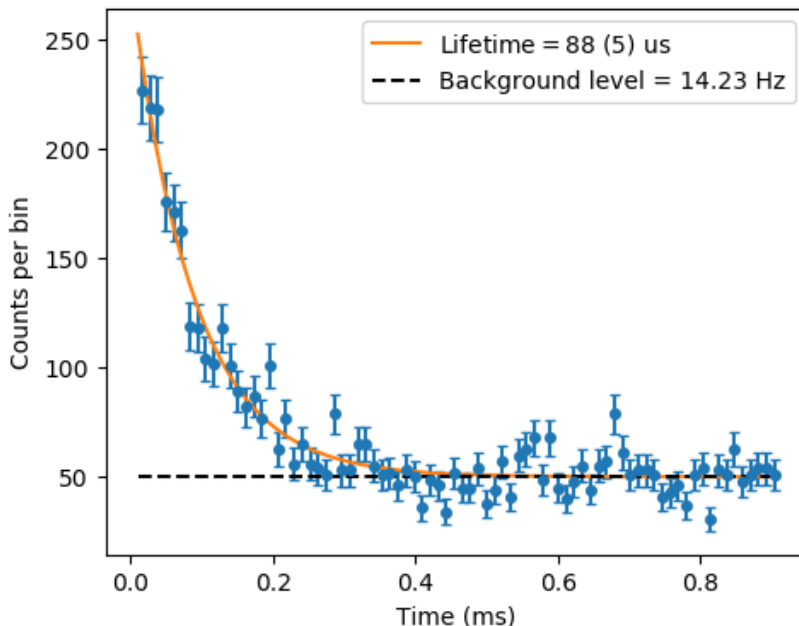


Figure 6.7: High Purcell-enhancement observed on a different nanoparticle. Fit to a single exponential gives a lifetime of $T_c = 88(5) \mu\text{s}$, which corresponds to a Purcell factor of $C = 155(8)$.

$T_c = 88(5) \mu\text{s}$, which corresponds to a Purcell factor of 155(8) that matches with the maximum expected Purcell factor. Additionally, the emission was strongly dependent on the frequency of excitation, which could imply that the emission was originating from one or few spectrally resolved ions. As the obtained Purcell-factor matches with the expected value, we can conclude that the dipoles of these emitters perfectly align with the polarization axis of the cavity. This measurement demonstrates that with the demonstrated cavity stability we could achieve the maximum expected Purcell factors if suitably oriented ions can be found in a nanoparticle. We couldn't unfortunately continue our measurements on this nanoparticle due to technical

issues with the cryostat.

6.3 Conclusion

In conclusion, in this chapter we have demonstrated the detection of a single erbium ion doped in a nanoparticle coupled to a fiber microcavity. This was enabled by improving several aspects of our experimental setup including the cavity stability and the collection and detection efficiency of the photons generated inside the cavity. We were able to demonstrate a Purcell factor of 60(1) for the detected single erbium ion, which is a factor 4 higher than the average value reported in Ch. 5. The photons emitted by the erbium ion were detected with an estimated efficiency of $p_{det} = 0.039$, which is an improvement of factor ≈ 15 over the previous setup. Hence, the SNR was higher by a factor ~ 50 in the lifetime of the photon for the experiments in this chapter compared to the ones presented in Ch. 5.

The SNR is limited by the measured Purcell factor as well as by the total intra-cavity losses. The measured Purcell factor of 60 can be increased towards the expected value of ≈ 150 by coupling to ions whose dipole aligns better to the cavity polarization axis. Isolating ions in different nanoparticles could eventually allow us to couple to an optimally aligned ion, as demonstrated in Sec. 6.2.4. The intra-cavity losses arise due to the scattering loss of the nanoparticle as well due to the loss introduced by our nanoparticle preparation procedure. If we can improve this so as to introduce a total intra-cavity loss of $2B \approx 30$ ppm, which is the loss we expect for an averagely sized nanoparticle, then the finesse on the nanoparticle would be $\sim 35,000$. This would not only improve the escape efficiency to $\eta_{ecp} = 0.58$ from the current value of 0.32, but also the maximum expected Purcell factor to ≈ 260 from the current value of 150. Hence, for a perfectly coupled ion we would expect the SNR to improve by a factor ~ 8 (SNR ~ 16).

In the lifetime of the emitter, we measured an uncorrected $g^{(2)}(0) = 0.59(5)$ for the emitted photons, which is limited by the SNR in our experiment. If the SNR can be improved to 16, then we would expect this value

to be ≈ 0.11 . The obtained value of $g^{(2)}(0)$, together with a saturation of counts, is conclusive evidence that the photons are emitted by a single emitter.

The linewidth of the erbium ion was found to be 380 MHz, which is more than two orders of magnitude higher than the expected value. It could be a result of multiple factors, including a higher local temperature of the nanoparticle, as well as the ion experiencing higher dephasing due to coupling to defects. Reducing the temperature of the nanoparticles, for example by placing them in a cryostat where they are directly cooled by helium gas, could substantially reduce the linewidth of the ions. This should also enable detecting ions closer to the centre of the inhomogeneous line, which could experience lower dephasing due to reduced coupling to defects.

Chapter 7

Conclusion & Outlook

7.1 Main results of this thesis

The main goal of this thesis was to detect single erbium ions in Y_2O_3 nanoparticles coupled to fiber-based high-finesse microcavities and investigate their feasibility for applications in quantum networks. We hence first measured the optical coherence properties of the ${}^4I_{15/2} - {}^4I_{13/2}$ transition in $\text{Er}^{3+}:\text{Y}_2\text{O}_3$ nanoparticles at cryogenic temperatures in Ch. 4. The branching ratio of the transition was estimated to be $\zeta \approx 0.13$. The optical inhomogeneous linewidth was found to be centred at 1535.49 nm with a FWHM of 10.7 GHz and the excited state lifetime T_1 was measured to be 13.68 ms. The optical coherence time T_2 was measured to be 840 ns ($\Gamma_h = 379$ kHz) at the lowest available temperature of ~ 3 K. The homogeneous linewidth was found to have a linear dependence with temperature due to coupling to two-level systems (TLS) and the linewidth extrapolated to 0 K is ~ 10 kHz. The time-dependent spectral diffusion was measured to broaden the linewidth to $\Gamma_{\text{eff}} \sim 3$ MHz after a waiting time of ~ 40 μs . We concluded that significant improvement in the crystalline quality of our nanoparticles as well as a reduction in their temperature is needed for them to be useful for quantum network applications.

In Sec. 4.5, we also investigated the optical and spin coherence proper-

ties of the $^1D_2 - ^3H_4$ transition at ~ 619 nm in $\text{Pr}^{3+}:\text{Y}_2\text{O}_3$ nanoparticles. The branching ratio of the transition was estimated to be $\zeta \approx 0.057$. Lifetime of the optical excited state was measured to be $T_1 = 140 \mu\text{s}$, while a coherence time of $1 \mu\text{s}$ was measured for 150 nm nanoparticles. The coherence times of the spin states were in excess of $500 \mu\text{s}$, which is even longer than the ones measured in bulk $\text{Pr}^{3+}:\text{Y}_2\text{SiO}_5$. With reasonable improvements in the optical coherence time while reducing the size of the nanoparticle, we conclude that praseodymium could be a promising alternate to erbium.

In Ch. 5, using the first iteration of the custom-built nano-positioner system, we report on the Purcell-enhanced emission from an ensemble of erbium ions doped into Y_2O_3 nanoparticles coupled a high-finesse fiber microcavity. We achieve an average Purcell factor of 14 for the whole ensemble, while a small subset of the ions show Purcell factors over 70. The decay is multi-exponential, which is explained with a detailed model that includes contributions from the random dipole orientation of the erbium ions in the nanoparticle as well as cavity instability. Additionally, we demonstrate dynamic control of the Purcell-enhanced emission by tuning the cavity resonance on a time-scale of $\sim 100 \mu\text{s}$, which is faster than the spontaneous emission rate of the ions. Using this technique, we measure the lifetime of the ions placed on the planar mirror to be 10.8 ms, as well as shape the waveform of the emitted photons without perturbing the emitter.

Finally, utilizing the second iteration of the nano-positioner system, we reported on the detection of a single erbium ion in $\text{Er}^{3+}:\text{Y}_2\text{O}_3$ nanoparticles coupled to a fiber micro-cavity in Ch. 7. This was enabled by improving several aspects of our experimental setup including the cavity stability and the collection and detection efficiency of the photons generated inside the cavity. The single ion exhibited a Purcell factor of 60(1), which corresponds to a cavity enhanced lifetime of $225 \mu\text{s}$. The emitted photons were detected with an estimated efficiency of $p_{det} = 3.9 \%$, which is an improvement of factor ≈ 15 over the setup in Ch. 5, while the signal-to-noise ratio (SNR) was higher by a factor ~ 50 in the lifetime of the ion. The photons received per trial showed a clear saturation at higher excitation powers, which is characteristic of single emitters. In the lifetime of the emitter, we measured

an uncorrected $g^{(2)}(0) = 0.59(5)$ for the emitted photons, which is limited by the SNR in our experiment. The value after background subtraction is $0.29(9)$, which could be limited due to emission from other weakly coupled ions as well as electronic noise. The obtained value of $g^{(2)}(0)$, together with a saturation of counts, is conclusive evidence that the photons are emitted by a single erbium ion. The linewidth of the erbium ion was found to be 380 MHz, which is more than two orders of magnitude higher than the expected value. Further measurements are needed to investigate the source of this broadening. We were also able to measure a Purcell factor ~ 150 in another nanoparticle, which demonstrates that Purcell factors close to the theoretical limit are possible with our system.

7.2 Outlook

In the short term, the main goal of this project beyond the work reported in this thesis is to fully understand the behaviour of single erbium ions in our system. Primarily, we will investigate the mechanisms that broaden the erbium ions beyond the expected value. Measuring the linewidth of ions in other nanoparticles could inform us about the inhomogeneity in measured properties among different nanoparticles. Additionally, comparing the dependence of the ions' linewidth on temperature with the measurements done on an ensemble of nanoparticles (see Sec. 4.3.3) could help us identify the actual temperature of the single ions. Issues with thermalization could be solved by embedding the nanoparticles in a dielectric layer [66], or by utilizing a cryostat where the nanoparticles are directly cooled with helium gas. Furthermore, coupling to a smaller nanoparticle would not only enable higher Purcell factors but also increase the SNR in the experiment. This would lower the measured value of uncorrected $g^{(2)}(0)$.

As our fiber micro-cavity is slightly birefringent (see Fig. 3.15), we expect it to only enhance spin-selective transitions when coupled to a single polarization mode. This leads to highly-cycling transitions that can be utilized to readout the spin-state of a single erbium ion [53], as well as to generate spin-photon entanglement using the scheme described in [22].

If the photons emitted by two single erbium ions are indistinguishable, then heralded entanglement between the two erbium ions can be achieved by performing a Bell-state measurement (BSM) of the emitted photons. The spin-state of each erbium ion can then be transferred to another rare-earth ion for long-term storage as well as to perform deterministic Bell-state measurement [46–48], which could greatly enhance the rate of entanglement distribution over distances larger than 500 km [6, 124].

For the photons emitted by an erbium to be indistinguishable, we need to satisfy $\Gamma_{\text{eff}} \approx \Gamma_r$. As discussed in detail in Sec. 4.4, state-of-the-art fiber micro-cavities together with improvements in the optical coherence properties of erbium-doped nanoparticles could enable this in the near future. Other platforms, such as erbium doped thin crystals, could also be integrated into fiber microcavities towards this goal. High indistinguishability can also be achieved by temporal filtering of the emitted photons at the cost of reduced entanglement distribution rates [124].

In addition, since we identified praseodymium as a promising alternative to erbium, we are already working towards coupling $\text{Pr}^{3+}:\text{Y}_2\text{O}_3$ nanoparticles to high-finesse fiber microcavities. As discussed in detail in Sec. 4.5.3, producing indistinguishable photons from Pr^{3+} ions doped in Y_2O_3 nanoparticles could be more easily achieved due to their superior coherence properties. $\text{Pr}^{3+}:\text{Y}_2\text{O}_3$ nanoparticles have long spin coherence times in their spin state [60], which enables them to store quantum information for long times. In addition, two-qubit gates between two Pr^{3+} ions could be also be implemented to perform deterministic BSM [124]. Due to the small frequency splitting in the hyperfine states in $\text{Pr}^{3+}:\text{Y}_2\text{O}_3$, the frequency separation between multiple qubits in the inhomogeneous line can be small [124], which allows a large number of ions to be addressed. This, however, comes at the cost of reduced fidelities as the probability to interact with other hyperfine states off-resonantly increases. If combined with optical frequency conversion to telecommunications wavelength, single Pr^{3+} ions could form a node in a quantum network with both communication and computing capabilities.

Appendix A

Appendix

A.1 Model for multi-exponential decay

The single exponential fit does not describe well the data for the Purcell enhanced case suggesting that emitters experiencing different enhancement contribute to the detected signal (see dash dotted red line in Fig. 5.5). To investigate this further, Dr. Bernardo Casabone, with the help of other authors, derived a model describing our experiment. The model considers a large ensemble of ions in a nanoparticle that experience a maximum Purcell factor C_{\max} which is then reduced due to three main factors.

The first factor is related to the orientation of the dipole moments of the ions. To estimate this first contribution, we consider a spherical nanoparticle of radius r , which is composed from several crystalline structures. Each crystalline structure supports three orthogonal directions for the orientation of the dipoles. Already for a small number of structures, it is reasonable to assume that the dipole orientations are random and homogeneously distributed. For a cavity axis along \hat{z} and considering that both components of the cavity electric field $\vec{E} = E_x\hat{x} + E_y\hat{y}$ have the same resonance frequency, each ion i in the nanoparticle experiences a reduced Purcell $C_{\max} \cdot R_{i,d}$ with

$$R_{i,d} = (\hat{x} \cdot \hat{n}_i)^2 + (\hat{y} \cdot \hat{n}_i)^2 = n_{i,x}^2 + n_{i,y}^2 \quad (\text{A.1})$$

where $n_{i,\{x,y\}}$ are the components of the dipole moment $\bar{d}_i = d_i \hat{n}_i$ along the x and y axes.

Next, we consider the finite extension of the nanoparticle with respect to the standing wave of the cavity field, meaning that ions far from the center experience an additional reduction of the Purcell factor. This reduction is given by

$$R_{i,\text{sw}} = \cos\left(\frac{z_i + z_{\text{offset}}}{\lambda} \cdot 2\pi\right)^2 \quad (\text{A.2})$$

where z_i is the distance of the ion i in the z -axis from the center of crystal, and z_{offset} is the distance of the center of the crystal to the maximum of the standing wave.

Finally, we model the fluctuation of the cavity by a single-frequency sinusoidal as $\delta(t) = A \cos(t \cdot 2\pi\nu)$ where ν is the main frequency component of the 790 nm transmission signal, and A corresponds to the cavity displacement amplitude (see Sec.5.2.1). This affects equally all ions, thus the Purcell factor is globally reduced by

$$R_{\mathcal{L}(t,\phi)} = \frac{(\Delta/2)^2}{(\delta(t) + \delta_0)^2 + (\Delta/2)^2} \quad (\text{A.3})$$

where \mathcal{L} is the Lorentzian spectral line shape of the cavity, $\Delta = \frac{\lambda/2}{F}$ is the FWHM and δ_0 is detuning of the cavity at the time a particular trial of the experiment starts.

Now, we model the detected counts as function of time following two different strategies: a dynamic one and a static one. For the dynamic approach, we assume a large number of ions and calculate the probability to detect photons as function of time which is mainly determined by the time-dependent Purcell factor. For the static one, we reconstruct the detected counts by calculating the distribution of decays rates present in our system. The main difference between these two methods is that the frequency at which the cavity vibrates is relevant only for the first method (see discussion below).

To model the counts per bin as function of the time following the dynamic strategy, we consider a large ensemble of ions which are excited and

start to decay. The probability that an ion i emits in the cavity as a function of time is proportional to

$$e^{-\int_0^t \frac{C(t',i,\delta_0)}{T_1} dt'}, \quad (\text{A.4})$$

with a time-dependent Purcell factor given by

$$C(t, i, \delta_0) = C_{\max} \cdot R_{i,d} \cdot R_{i,sw} \cdot R_{\mathcal{L}(t,\delta_0)}. \quad (\text{A.5})$$

The total detected counts as function of the time is estimated by averaging over a large number of ions with randomly chosen initial cavity detunings δ_0 , that is,

$$\text{cts}(t) \approx \eta \sum_i^{\#i} \sum_{\delta_0}^{\#\delta_0} \frac{e^{-\int_0^t \frac{C(t',i,\delta_0)}{T_1} dt'}}{\#i \#\delta_0} \quad (\text{A.6})$$

with $\#i$ and $\#\delta_0$ the number of ions and detunings which are considered, and η is a normalization factor that includes the detection efficiency and the number of ions which are excited at the beginning of the experiment.

For the static approach, we model the detected counts as linear superposition of exponential decaying curves, that is,

$$\text{cts}(t) \approx \int_0^1 p(s) e^{-\frac{s t C_{\max}}{T_1}} ds. \quad (\text{A.7})$$

with $s = C/C_{\max}$ and $p(s)$ the normalized distribution of Purcell factor present in the system. We start by discretizing eq. A.7 such that

$$\text{cts}(t) \approx \sum_{j=1}^n p(s_j) e^{-\frac{s_j t C_{\max}}{T_1}} \Delta_s \quad (\text{A.8})$$

with $s_j = [1/n, 2/n, \dots, 1]$, n the number of discrete steps and $\Delta_s = 1/n$ is the step size. To estimate $p(s_j)$, we first calculate the discrete distributions $p_d(s_d)$, $p_{sw}(s_{sw})$ and $p_{\mathcal{L}}(s_{\mathcal{L}})$ corresponding to the distributions of the dipole orientations of the ions, the position of the nanoparticle with respect to the standing wave and the fluctuations of the cavity respectively.

Note $s_d, s_{sw}, s_{\mathcal{L}}, = [1/n, 2/n, \dots, 1]$. $p_d(s_d)$ and $p_{sw}(s_{sw})$ are calculated by making normalized histograms of $R_{i,d}$ and $R_{i,sw}$ by placing ions randomly and homogeneously distributed in the nanoparticle with randomly oriented dipole moments. Note that the bin size of the histogram is set to be the same as the step size $1/n$ of the discrete distribution, such that the bins correspond to $[(0-1/n), (1/n-2/n), \dots, -1]$.

The distribution $p_{\mathcal{L}}$ cannot be directly calculated because it is a time dependent function. We therefore estimate it following a stroboscopy approach. That is, $p_{\mathcal{L}}$ is given by the normalized histogram of $R_{\mathcal{L}(t,\delta_0)}$ calculated at random times t in a time interval larger than the chosen period of the cavity vibration.

We now have three lists, which correspond to the three discrete distributions, of the form (s, p) with n elements each. $p(s_j)$ is then calculated as follows: first, we make a new list (s', p') containing n^3 elements where

$$s' = s_d[k] \cdot s_{sw}[l] \cdot s_{\mathcal{L}}[m], \quad (\text{A.9})$$

$$p' = p_d(s_d)[k] \cdot p_{sw}(s_{sw})[l] \cdot p_{\mathcal{L}}(s_{\mathcal{L}})[m], \quad (\text{A.10})$$

where $k, l, m = [1, 2, \dots, n]$ are indices for elements of the corresponding lists. We then construct a new histogram out of the list (s', p') with bin size set to $1/n$. Finally, the histogram is normalized to obtain $p(s_i)$. The obtained distributions $p_d, p_{sw}, p_{\mathcal{L}}$ and p are shown in Fig. A.1.

The main difference between the static and the dynamic methods arises mainly in how $p_{\mathcal{L}}$ is calculated. In our calculation, the frequency of the cavity vibration ν does not influence the value of $p_{\mathcal{L}}$. We now illustrate how this small difference strongly affects the model. First, we consider the case where the time scale of the cavity vibration $1/\nu$ is much slower than the slower lifetime τ' present in the system, that that is, $1/\nu \ll \tau'$. In this case, in some trials of the experiment, we will record very fast photons as the cavity is on resonance for a time longer than $\tau_{C_{\max}}$, while moments later, when the cavity is slowly moving out of resonance, slower photons will be recorded. After integrating counts for a very long time, fast and slow contributions should be clearly visible in the data. Now, we consider the opposite case in where $1/\nu \gg \tau'$, that is, very fast cavity vibration

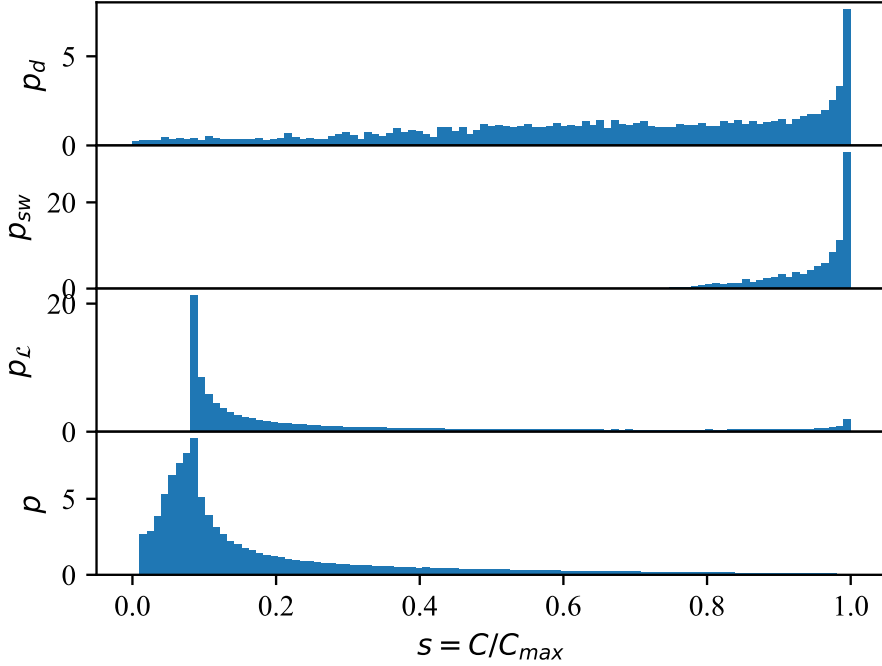


Figure A.1: Normalized distributions p_d and p_{sw} obtained after making histograms of $R_{i,d}$ and $R_{i,sw}$ over a large number of randomly placed ions with randomly oriented dipoles. The distribution $p_{\mathcal{L}}$ is calculated following a stroboscopic approach on the values of $R_{\mathcal{L}(t,\delta_0)}$ over a large sampling space. Finally, the normalized distribution p is calculated from p_d , p_{sw} and $p_{\mathcal{L}}$ as described in the text.

compared to the slower decay rate present in the system. In this case, on each trial, we can assume that the cavity will be on average enough time on resonance such that all the ions had already decayed at early times of the trial, thus no photons will be recorded at later stages. In this case, for long integration times, a slow component is not expected in the signal, although

the cavity displacement can be assumed to be the same as in the opposite case. The influence of the frequency of the vibrations of the cavity on the ions can only be studied by the dynamic model and not by the static one.

Fig. 5.5 and Fig. 5.6 show both the dynamic and the static model for the parameters of our system. The radius of the particle is set to 90 nm consistent with measurements. The finesse of the cavity is 16,000 for which $\Delta = 50$ pm. The offset of the maximum of the standing wave with respect of the crystal z_{offset} is 50 nm. The amplitude of the cavity fluctuations is set to $A = \text{Noise}_{\text{RMS}} \cdot \sqrt{2} = 88.4$ pm where $\text{Noise}_{\text{RMS}} = 62.5$ pm and the frequency of the cavity displacement $\nu = 200$ Hz (see Sec. 5.2.1), and a maximum Purcell factor $C_{\text{max}} = 150$.

Finally, the remaining parameter is the normalization factor. The normalization factor is related to the number of ions that are excited after the pulse and the detection efficiency. This factor is difficult to assess as the number of excited ions strongly depends on the power broadening which depends on the homogeneous linewidth which is unknown. The normalization is set by minimizing the RMSE between the model and the data set. Finally, on each bin we add counts to account for the measured dark count rate of 13.7 Hz. As seen in Fig. 5.5, both models stay consistently below one standard deviation from the data. The dynamic model fails to describe the slower components, thus suggesting that slower component in the cavity vibration are present. These slower components can be explained by the 2 Hz cycle of the cryostat.

In conclusion, we presented a model that accurately describes the data. From the model we conclude that the early fast decay seen in the data can only be explained if a small ensemble of ions experience a large Purcell factor which is then reduced. The main reduction is related to the cavity stability. In case the cavity stability improves, ions in the center of the nanoparticle and with the dipole moment aligned to the cavity electric field could be in principle isolated yielding to an up to five times higher signal to noise ratio, a level at which single ion detection would be feasible in our setup (see below).

A.2 Cavity switching time

As discussed in Sec. 5.4, we switch the cavity resonance by a fast change of a voltage offset on a piezoelectric and by stabilizing the cavity to either side of the 790 nm cavity fringe at will. Between the two sides of the fringe, the total cavity length displacement is $\Delta_{790} = \text{FWHM}_{790}$. The 1535 nm resonance with linewidth Δ overlaps with the middle of one side of the 790 nm fringe, thus when the cavity is stabilized to the opposite side, erbium ions are detuned from the cavity. Now, we characterize the reduction of the Purcell factor and the spontaneous emission rate in the cavity mode during the time the cavity resonance is switched. The Purcell factor as function of the detuning δ from the cavity resonance Δ is then given by

$$C(\delta) = \mathcal{L}(\circ) \cdot C, \quad (\text{A.11})$$

where

$$\mathcal{L}(\circ) = \frac{(\Delta/2)^2}{\delta^2 + (\Delta/2)^2}, \quad (\text{A.12})$$

is the normalized Lorentzian spectral line of the cavity. The detected count rate as function of the time is given by [122]

$$r(t) = \frac{C(t)}{T_1} \cdot \mathcal{N}(t) \quad (\text{A.13})$$

where T_1 is the natural lifetime, $\mathcal{N}(t)$ is the number of ions in the excited state and $C(t)$ is the Purcell factor. The number of ions in the excited state can be calculated as

$$\mathcal{N}(t) = \mathcal{N}_0 e^{-\frac{t}{T_1} - \int_0^t \frac{C(t')}{T_1} dt'} \quad (\text{A.14})$$

where \mathcal{N}_0 is the number of ions in the excited state before the cavity frequency is shifted. The first term in the exponent of Eq. A.14 takes into account the decrease in population due to emission in free space, while the second term does it in the cavity mode. Eq. A.14 only takes into account the modification in the density of states and neglects light-matter dynamics [122].

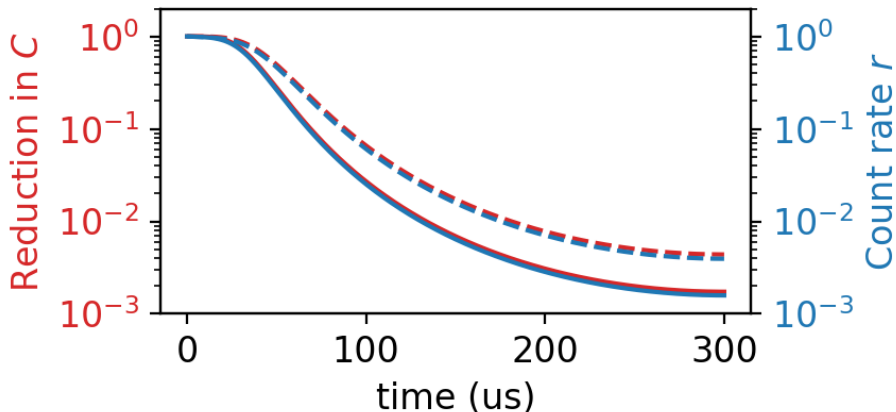


Figure A.2: Reduction of the Purcell factor (red) and the count-rate (blue) as function of time during $S_{790} = 300 \mu\text{s}$. Solid lines is for the ideal detuning of $\delta = \frac{\Delta_{790}}{\Delta_{1535}} \Delta = 12\Delta$ and dashed line for $\delta = \frac{\Delta_{790}}{\Delta_{1535,eff}} \Delta = 7.5\Delta$, the value obtained considering the cavity stability.

In order to minimize coupling of mechanical noise in the cavity, the detuning as function of time, that is, the voltage applied to the piezoelectric transducer, is given by

$$\delta(t) = \Delta_{790} \cdot \sin^2 \left(\frac{\pi t}{2S_{790}} \right) \quad (\text{A.15})$$

where S_{790} is the switching time between the two locking points. For this experiment, we use $S_{790} = 300 \mu\text{s}$. Assuming the cavity resonance at 1535 nm is $\Delta_{1535} = \Delta_{790}/12$ and a Purcell factor 15, we expect a total reduction of $1/577$ in the Purcell factor and $1/630$ in the countrate (see Fig. A.2). Depending on the practical purpose a faster decoupling time might be required, which can be achieved at the expenses of a smaller reduction of the Purcell factor or the countrate. Here we define the switching

time S_{1535} as the time needed to decrease the countrate by a factor of 10. For ideal parameters, we therefore expect $S_{1535} = 67 \mu\text{s}$.

Now, we compare the expected reduction of the Purcell factor and the countrate with the measured values. Fig. 5.12 shows the detected countrate as a function of time at the moment the cavity is tuned off- and on-resonance. The solid line is the model defined in Eq. A.13. To take into account the cavity stability, we introduce an effective cavity linewidth defined as

$$\Delta_{1535,eff} = \sqrt{\Delta_{1535}^2 + \text{Noise}_{\text{RMS}}^2} \quad (\text{A.16})$$

with $\text{Noise}_{\text{RMS}} = 62.5 \text{ pm RMS}$ as measured. For these parameters, the maximum reduction of the Purcell factor is $1/227$ and for the countrate is $1/253$.

In Fig. 5.12 on left, the first vertical orange line indicates the beginning of the switching and the second is the time at which the countrate is reduced by a factor of 10, giving a $S_{1535} = 85(15) \mu\text{s}$. In Fig. 5.12 on right, the second vertical blue line indicates the end of the switching and the first is the time at which the detected countrate is a factor of 10 smaller than the maximum, for which the time interval is $87(16) \mu\text{s}$. Here, we see that by the time the cavity is back on resonance, the maximum countrate cannot be reached as population is lost during the switching process which occurs in a time scale comparable to the Purcell enhanced decay time.

In order to reduce further the switching time (assuming the cavity stability is not the limiting factor), one can simply move the piezo faster thus reducing S_{790} . However, a faster kick leads to increased residual mechanical noise. Fig. A.3 shows the residual noise as function of the switching time S_{790} . The residual noise is calculated as the standard deviation of the locking signal in the first 1 ms after the cavity is set on resonance at 1535 nm. As expected, the residual noise increases for a faster switching time S_{790} , that is, for faster switching frequency. We estimate the switching frequency as $1/(2 \times S_{790}) \approx 1.6 \text{ kHz}$. The characteristic frequency of the residual noise is between $7 - 10 \text{ kHz}$. We attribute this residual motion to the fiber in the plane perpendicular to the cavity axis. To first order, the cavity length should be robust against the lateral displacement of the fiber. However, a

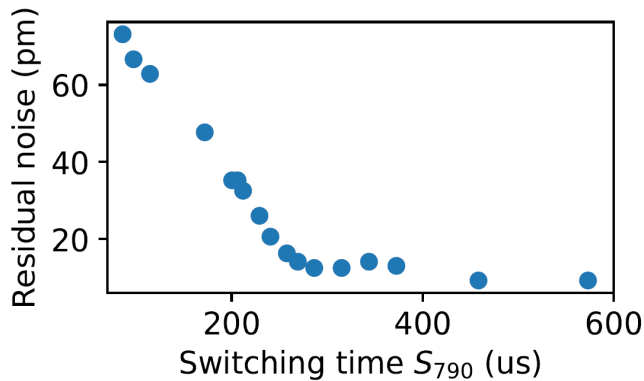


Figure A.3: Residual noise in the cavity as a function of the switching time S_{790} .

misalignment when placing the fiber in the positioner could lead to strong coupling between them, as confirmed in our experiment. We see that while moving the fiber laterally, the cavity length is shifted, and we estimate the coupling to be in the 20 – 40% range.

In order to increase the switching time S_{1535} , we can follow several strategies:

- perform a proper alignment of the fiber in order to minimize the coupling between the vibration modes,
- increase the frequency of all mechanical eigenmodes,
- increase the finesse of the 1535 nm resonance,
- use a faster growing function than \sin^2 or implement iterative learning algorithms to shape the signal sent to the piezo to minimize added noise

Altogether, we estimate that values of S_{1535} in the microsecond scale could be achievable by combing these improvements if the cavity stability issue is addressed.

A.3 Emitters coupled to an off-resonance cavity

As an off resonant cavity is in some cases expected to lead to a suppression of spontaneous emission, we need to quantify this effect in order to extract the natural lifetime by cavity-resonance switching as above. For an off-resonant cavity, emission suppression will be due to destructive interference of partial waves within a narrow solid angle only. The specific geometry of the mirror defines the quantitative value of the suppression, in particular the geometry of the concave profile. In our case, this is a very shallow profile (structure depth $\sim 1.5 \mu\text{m}$, radii of curvature of $50 \mu\text{m}$), such that only modes within a small angular range of $\alpha \approx 6 \text{ deg}$ will be suppressed. A comparable geometry of an open access microcavity, however with larger aspect ratio and thus larger angular range ($\alpha \approx 22$) was studied in [125], where a suppression of 32% was calculated by FDTD. This fits reasonably well to the fraction of the 4π -solid angle that the geometry covers, where $\Omega = 2 \times 2\pi(1 - \cos(\alpha))$ is the estimated effective solid angle that is relevant for the suppression. For $\alpha = 22 \text{ deg}$, this yields a 29% suppression, close to the FDTD result. Translated to our geometry, for $\alpha = 6 \text{ deg}$, we obtain a negligible lifetime suppression of $< 3\%$.

To summarize, in the data shown in Fig. 5.5 in order to extract the natural lifetime, we estimate that the effect of the off-resonance cavity is negligible, but can be of relevance for different geometries. We note that by performing measurements with dynamic switching at different mirror separations, it will be possible to quantify the effect of emission suppression, such that the measurement in principle indeed allows one to obtain an accurate value of the Purcell factor. We note however, that the presence of the mirror carrying the sample comes in addition, and needs to be quantified separately. Comparing to a crystal in free space would thus yield larger values of the Purcell factor.

Bibliography

1. Ladd, T. D. *et al.* Quantum computers. *Nature* **464**, 45–53 (2010).
2. Feynman, R. P. Simulating physics with computers. *International Journal of Theoretical Physics* **21**, 467–488 (1982).
3. Georgescu, I., Ashhab, S. & Nori, F. Quantum simulation. *Reviews of Modern Physics* **86**, 153–185 (2014).
4. Briegel, H.-J., Dür, W., Cirac, J. I. & Zoller, P. Quantum Repeaters: The Role of Imperfect Local Operations in Quantum Communication. *Phys. Rev. Lett.* **81**, 5932–5935 (1998).
5. Gisin, N., Ribordy, G., Tittel, W. & Zbinden, H. Quantum cryptography. *Rev. Mod. Phys.* **74**, 145–195 (2002).
6. Sangouard, N., Simon, C., De Riedmatten, H. & Gisin, N. Quantum repeaters based on atomic ensembles and linear optics. *Reviews of Modern Physics* **83**, 33–80 (2011).
7. Degen, C., Reinhard, F. & Cappellaro, P. Quantum sensing. *Review of Modern Physics* **89** (2017).
8. Kimble, H. J. The quantum internet. *Nature* **453**, 1023–1030 (2008).
9. Duan, L.-M., Lukin, M. D., Cirac, J. I. & Zoller, P. Long-distance quantum communication with atomic ensembles and linear optics. *Nature* **414**, 413–418 (2001).

10. Zukowski, M., Zeilinger, A., Horne, M. A. & Ekert, A. K. “Event-ready-detectors” Bell experiment via entanglement swapping. *Phys. Rev. Lett.* **71**, 4287– (1993).
11. Yu, Y. *et al.* Entanglement of two quantum memories via fibres over dozens of kilometres. *Nature* **578**, 240–245 (2020).
12. Jing, B. *et al.* Entanglement of three quantum memories via interference of three single photons. *Nature Photonics* **13**, 210–213 (2019).
13. Ritter, S. *et al.* An elementary quantum network of single atoms in optical cavities. *Nature* **484**, 195–200 (2012).
14. Northup, T. E. & Blatt, R. Quantum information transfer using photons. *Nature Photonics* **8**, 356 (2014).
15. Bernien, H. *et al.* Heralded entanglement between solid-state qubits separated by three metres. *Nature* **497**, 86–90 (2013).
16. Hensen, B. *et al.* Loophole-free Bell inequality violation using electron spins separated by 1.3 kilometres. *Nature* **526**, 682–686 (2015).
17. De Greve, K. *et al.* Quantum-dot spin-photon entanglement via frequency downconversion to telecom wavelength. *Nature* **491**, 421–425 (2012).
18. Saglamyurek, E. *et al.* Broadband waveguide quantum memory for entangled photons. *Nature* **469**, 512–515 (2011).
19. Lago-Rivera, D., Grandi, S., Rakonjac, J. V., Seri, A. & de Riedmatten, H. Telecom-heralded entanglement between multimode solid-state quantum memories. *Nature* **594**, 37–40 (2021).
20. Awschalom, D. D., Hanson, R., Wrachtrup, J. & Zhou, B. B. Quantum technologies with optically interfaced solid-state spins. *Nature Photonics* **12**, 516–527 (2018).
21. Reiserer, A. & Rempe, G. Cavity-based quantum networks with single atoms and optical photons. *Reviews of Modern Physics* **87**, 1379–1418 (2015).

22. Barrett, S. D. & Kok, P. Efficient high-fidelity quantum computation using matter qubits and linear optics. *Physical Review A* **71**, 060310 (2005).
23. Najer, D. *et al.* A gated quantum dot strongly coupled to an optical microcavity. *Nature* (2019).
24. Wang, D. *et al.* Turning a molecule into a coherent two-level quantum system. *Nature Physics* **15**, 483–489 (2019).
25. Nguyen, C. *et al.* Quantum Network Nodes Based on Diamond Qubits with an Efficient Nanophotonic Interface. *Physical Review Letters* **123** (2019).
26. Sipahigil, A. *et al.* An integrated diamond nanophotonics platform for quantum-optical networks. *Science* **354**, 847–850 (2016).
27. Gao, W. B., Fallahi, P., Togan, E., Miguel-Sanchez, J. & Imamoglu, A. Observation of entanglement between a quantum dot spin and a single photon. *Nature* **491**, 426–430 (2012).
28. Riedel, D. *et al.* Deterministic Enhancement of Coherent Photon Generation from a Nitrogen-Vacancy Center in Ultrapure Diamond. *Physical Review X* **7** (2017).
29. Ruf, M. *et al.* Optically Coherent Nitrogen-Vacancy Centers in Micrometer-Thin Etched Diamond Membranes. *Nano Letters* **19**, 3987–3992 (2019).
30. Debroux, R. *et al.* Quantum Control of the Tin-Vacancy Spin Qubit in Diamond. *Physical Review X* **11** (2021).
31. Hennessy, K. *et al.* Quantum nature of a strongly coupled single quantum dot–cavity system. *Nature* **445**, 896–899 (2007).
32. Kuhlmann, A. V. *et al.* Charge noise and spin noise in a semiconductor quantum device. *Nature Physics* **9**, 570–575 (2013).
33. Veldhorst, M. *et al.* An addressable quantum dot qubit with fault-tolerant control-fidelity. *Nature Nanotechnology* **9**, 981–985 (2014).

34. Uppu, R., Midolo, L., Zhou, X., Carolan, J. & Lodahl, P. Quantum-dot-based deterministic photon–emitter interfaces for scalable photonic quantum technology. *Nature Nanotechnology* (2021).
35. Christle, D. J. *et al.* Isolated electron spins in silicon carbide with millisecond coherence times. *Nature Materials* **14**, 160–163 (2014).
36. Zhong, T. & Goldner, P. Emerging rare-earth doped material platforms for quantum nanophotonics. *Nanophotonics* **8**, 2003–2015 (2019).
37. Macfarlane, R. & Shelby, R. in *Spectroscopy of Solids Containing Rare Earth Ions* 51–184 (Elsevier, 1987).
38. Heinze, G., Hubrich, C. & Halfmann, T. Stopped Light and Image Storage by Electromagnetically Induced Transparency up to the Regime of One Minute. *Phys. Rev. Lett.* **111**, 033601– (2013).
39. Zhong, M. *et al.* Optically addressable nuclear spins in a solid with a six-hour coherence time. *Nature* **517**, 177–180 (2015).
40. Rančić, M., Hedges, M. P., Ahlefeldt, R. L. & Sellars, M. J. Coherence time of over a second in a telecom-compatible quantum memory storage material. *Nature Physics* **14**, 50–54 (2018).
41. De Riedmatten, H., Afzelius, M., Staudt, M. U., Simon, C. & Gisin, N. A solid-state light-matter interface at the single-photon level. *Nature* **456**, 773–777 (2008).
42. Hedges, M. P., Longdell, J. J., Li, Y. & Sellars, M. J. Efficient quantum memory for light. *Nature* **465**, 1052–1056 (2010).
43. Clausen, C. *et al.* Quantum storage of photonic entanglement in a crystal. *Nature* **469**, 508–511 (2011).
44. Seri, A. *et al.* Quantum Correlations between Single Telecom Photons and a Multimode On-Demand Solid-State Quantum Memory. *Phys. Rev. X* **7**, 021028– (2017).
45. Wesenberg, J. H., Mølmer, K., Rippe, L. & Kröll, S. Scalable designs for quantum computing with rare-earth-ion-doped crystals. *Physical Review A* **75** (2007).

46. Kimiaee Asadi, F. *et al.* Quantum repeaters with individual rare-earth ions at telecommunication wavelengths. *Quantum* **2**, 93 (2018).
47. Asadi, F. K., Wein, S. C. & Simon, C. Protocols for long-distance quantum communication with single ^{167}Er ions. *Quantum Science and Technology* **5**, 045015 (2020).
48. Asadi, F. K., Wein, S. C. & Simon, C. Cavity-assisted controlled phase-flip gates. *Physical Review A* **102**, 013703 (2020).
49. Kolesov, R *et al.* Optical detection of a single rare-earth ion in a crystal. *Nature communications* **3**, 1029 (2012).
50. Utikal, T. *et al.* Spectroscopic detection and state preparation of a single praseodymium ion in a crystal. *Nature communications* **5**, 3627 (2014).
51. Eichhammer, E., Utikal, T., Götzinger, S. & Sandoghdar, V. Spectroscopic detection of single Pr ions on the $3\text{H}_4\text{-}1\text{D}_2$ transition. *New Journal of Physics* **17**, 083018 (2015).
52. Dibos, A., Raha, M., Phenicie, C. & Thompson, J. Atomic Source of Single Photons in the Telecom Band. *Physical Review Letters* **120** (2018).
53. Raha, M. *et al.* Optical quantum nondemolition measurement of a single rare earth ion qubit. *Nature Communications* **11**, 1605 (2020).
54. Chen, S., Raha, M., Phenicie, C. M., Ourari, S. & Thompson, J. D. Parallel single-shot measurement and coherent control of solid-state spins below the diffraction limit. *Science* **370**, 592–595 (2020).
55. Zhong, T. *et al.* Optically Addressing Single Rare-Earth Ions in a Nanophotonic Cavity. *Phys. Rev. Lett.* **121**, 183603 (2018).
56. Kindem, J. M. *et al.* Control and single-shot readout of an ion embedded in a nanophotonic cavity. *Nature* (2020).
57. Ulanowski, A., Merkel, B. & Reiserer, A. Spectral multiplexing of telecom emitters with stable transition frequency. *arXiv:2110.09409*. arXiv: 2110.09409 (2021).

58. Bartholomew, J. G., de Oliveira Lima, K., Ferrier, A. & Goldner, P. Optical Line Width Broadening Mechanisms at the 10 kHz Level in Eu³⁺:Y₂O₃ Nanoparticles. *Nano Lett.* **17**, 778–787 (2017).
59. Serrano, D., Karlsson, J., Fossati, A., Ferrier, A. & Goldner, P. All-optical control of long-lived nuclear spins in rare-earth doped nanoparticles. *Nature Communications* **9**, 2127 (2018).
60. Serrano, D. *et al.* Coherent optical and spin spectroscopy of nanoscale Pr:Y₂O₃. *Physical Review B* **100** (2019).
61. Böttger, T., Sun, Y., Thiel, C. W. & Cone, R. L. Spectroscopy and dynamics of Er³⁺:Y₂SiO₅ at 1.5 μm. *Phys. Rev. B* **74**, 075107 (2006).
62. Böttger, T., Thiel, C. W., Sun, Y. & Cone, R. L. Optical decoherence and spectral diffusion at 1.5 μm in Er³⁺:Y₂SiO₅ versus magnetic field, temperature, and Er³⁺ concentration. *Phys. Rev. B* **73**, 075101 (2006).
63. Hunger, D. *et al.* A fiber Fabry–Perot cavity with high finesse. *New Journal of Physics* **12**, 065038 (2010).
64. Albrecht, R., Bommer, A., Deutsch, C., Reichel, J. & Becher, C. Coupling of a Single Nitrogen-Vacancy Center in Diamond to a Fiber-Based Microcavity. *Phys. Rev. Lett.* **110**, 243602 (2013).
65. Benedikter, J. *et al.* Cavity-Enhanced Single-Photon Source Based on the Silicon-Vacancy Center in Diamond. *Phys. Rev. Applied* **7**, 024031 (2017).
66. Casabone, B. *et al.* Cavity-enhanced spectroscopy of a few-ion ensemble in Eu:Y₂O₃. *New Journal of Physics* **20**, 095006 (2018).
67. Lutz, T. *et al.* Modification of phonon processes in nanostructured rare-earth-ion-doped crystals. *Physical Review A* **94** (2016).
68. Könz, F. *et al.* Temperature and concentration dependence of optical dephasing, spectral-hole lifetime, and anisotropic absorption in Eu³⁺:Y₂SiO₅. *Phys. Rev. B* **68**, 085109–9 (2003).

69. Thiel, C., Böttger, T. & Cone, R. Rare-earth-doped materials for applications in quantum information storage and signal processing. *Journal of Luminescence* **131**, 353–361 (2011).
70. Sinclair, N. *et al.* Spectral Multiplexing for Scalable Quantum Photonics using an Atomic Frequency Comb Quantum Memory and Feed-Forward Control. *Phys. Rev. Lett.* **113**, 053603– (2014).
71. Seri, A. *et al.* Quantum Storage of Frequency-Multiplexed Heralded Single Photons. *Physical Review Letters* **123**, 080502 (2019).
72. Welinski, S. *et al.* Coherence Time Extension by Large-Scale Optical Spin Polarization in a Rare-Earth Doped Crystal. *Physical Review X* **10**, 031060 (2020).
73. Jobez, P. *et al.* Coherent Spin Control at the Quantum Level in an Ensemble-Based Optical Memory. *Phys. Rev. Lett.* **114**, 230502– (2015).
74. Laplane, C., Jobez, P., Etesse, J., Gisin, N. & Afzelius, M. Multimode and Long-Lived Quantum Correlations Between Photons and Spins in a Crystal. *Phys. Rev. Lett.* **118**, 210501– (2017).
75. Kutluer, K., Mazzera, M. & de Riedmatten, H. Solid-State Source of Nonclassical Photon Pairs with Embedded Multimode Quantum Memory. *Phys. Rev. Lett.* **118**, 210502– (2017).
76. Perrot, A. *et al.* Narrow Optical Homogeneous Linewidths in Rare Earth Doped Nanocrystals. *Physical Review Letters* **111** (2013).
77. Liu, S. *et al.* Defect Engineering for Quantum Grade Rare-Earth Nanocrystals. *ACS Nano* **14**, 9953–9962 (2020).
78. Fabre, C., Sandoghdar, V., Treps, N. & Cugliandolo, L. F. *Quantum Optics and Nanophotonics* (Oxford University Press, 2017).
79. Reithmaier, J. P. *et al.* Strong coupling in a single quantum dot–semiconductor microcavity system. *Nature* **432**, 197–200 (2004).
80. Fox, M. *Quantum Optics: An Introduction* (Oxford University Press, 2006).

81. Loudon, R. *The Quantum Theory of Light* (Oxford University Press, 2000).
82. Grandi, S. *Single quantum emitters: resonance fluorescence and emission enhancement* PhD thesis (Imperial College London, 2017).
83. Saleh, B. E. A. & Teich, M. C. *Resonator Optics* 310–341 (John Wiley and Sons, 1991).
84. De Oliveira Lima, K., Gonçalves, R. R., Giaume, D., Ferrier, A. & Goldner, P. Influence of defects on sub-GHz optical linewidths in Eu³⁺: Y₂O₃ particles. *Journal of Luminescence* **168**, 276–282 (2015).
85. Xu, Y.-N., Gu, Z. & Ching, W. Y. Electronic, structural, and optical properties of crystalline yttria. *Physical Review B* **56**, 14993–15000 (1997).
86. Mader, M., Reichel, J., Hänsch, T. W. & Hunger, D. A scanning cavity microscope. *Nature communications* **6**, 7249 (2015).
87. Wind, M., Vlieger, J & Bedeaux, D. The polarizability of a truncated sphere on a substrate I. *Physica A: Statistical Mechanics and its Applications* **141**, 33–57 (1987).
88. Tsutsumi, T. Dielectric Properties of Y₂O₃ Thin Films Prepared by Vacuum Evaporation. *Japanese Journal of Applied Physics* **9**, 735–739 (1970).
89. El-Kareh, B. *Fundamentals of Semiconductor Processing Technologies* (Kluwer Academic Publishers, 1995).
90. Liu, S. *et al.* Controlled size reduction of rare earth doped nanoparticles for optical quantum technologies. *RSC Adv.* **8**, 37098–37104 (65 2018).
91. Beck, F. *Europium-doped nanocrystals in cryogenic optical microcavities* MA thesis (Ludwig-Maximilians-Universität München, 2016).
92. Sharma, V., Park, K. & Srinivasarao, M. Shape separation of gold nanorods using centrifugation. *Proceedings of the National Academy of Sciences* **106**, 4981–4985 (2009).

93. Hunger, D., Deutsch, C., Barbour, R. J., Warburton, R. J. & Reichel, J. Laser micro-fabrication of concave, low-roughness features in silica. *AIP Advances* **2**, 012119 (2012).
94. McAuslan, D. L., Longdell, J. J. & Sellars, M. J. Strong-coupling cavity QED using rare-earth-metal-ion dopants in monolithic resonators: What you can do with a weak oscillator. *Phys. Rev. A* **80**, 062307– (2009).
95. Lutz, T. *et al.* Effects of mechanical processing and annealing on optical coherence properties of Er:LiNbO₃ powders. *Journal of Luminescence* **191**, 2–12 (2017).
96. Deshmukh, C. *et al.* Optical coherence properties of nanoscale Kramers' rare-earth ions for quantum applications. *To be submitted* (2022).
97. Orbach, R. Spin-lattice relaxation in rare-earth solids. *Proc. R. Soc. Lond. Ser. A* **264**, 458 (1961).
98. Harris, T. L. *Erbium-based optical coherent transient correlator for the 1.5-micron communication bands* PhD thesis (Montana State University, 2001).
99. Veissier, L. *et al.* Optical decoherence and spectral diffusion in an erbium-doped silica glass fiber featuring long-lived spin sublevels. *Phys. Rev. B* **94** (2016).
100. Merkel, B., Ulanowski, A. & Reiserer, A. Coherent and Purcell-Enhanced Emission from Erbium Dopants in a Cryogenic High- Q Resonator. *Physical Review X* **10**, 041025 (2020).
101. Gündoğan, M., Ledingham, P. M., Almasi, A., Cristiani, M. & de Riedmatten, H. Quantum Storage of a Photonic Polarization Qubit in a Solid. *Phys. Rev. Lett.* **108**, 190504– (2012).
102. Rieländer, D. *et al.* Quantum Storage of Heralded Single Photons in a Praseodymium-Doped Crystal. *Phys. Rev. Lett.* **112**, 040504– (2014).

103. Rakonjac, J. V. *et al.* Entanglement between a Telecom Photon and an On-Demand Multimode Solid-State Quantum Memory. *Physical Review Letters* **127**, 210502 (2021).
104. Maring, N., Lago-Rivera, D., Lenhard, A., Heinze, G. & de Riedmat-ten, H. Quantum frequency conversion of memory-compatible single photons from 606 nm to the telecom C-band. *Optica* **5**, 507 (2018).
105. Okuno, T., Tanaka, K., Koyama, K., Namiki, M. & Suemoto, T. Homogeneous line width of Praseodymium ions in various inorganic materials. *Journal of Luminescence* **58**, 184–187 (1994).
106. Okuno, T. & Suemoto, T. Two types of spectral holes in Pr³⁺:Y₂O₃ crystalline systems. *Journal of Luminescence* **66–67**, 179–183 (1995).
107. Okuno, T. & Suemoto, T. Systematic control of spectral hole burning and homogeneous linewidth by disorder in Pr³⁺:Y₂O₃ crystalline systems. *Physical Review B* **59**, 9078–9087 (1999).
108. Fraval, E., Sellars, M. J. & Longdell, J. J. Method of Extending Hyperfine Coherence Times in Pr:Y₂SiO₅. *Phys. Rev. Lett.* **92**, 077601–4 (2004).
109. Casabone, B. *et al.* Dynamic control of Purcell enhanced emission of erbium ions in nanoparticles. *Nature Communications* **12** (2021).
110. Goswami, S., Heshami, K. & Simon, C. Theory of cavity-enhanced nondestructive detection of photonic qubits in a solid-state atomic ensemble. *Physical Review A* **98** (2018).
111. Minář, J. *et al.* Electric control of collective atomic coherence in an erbium-doped solid. *New Journal of Physics* **11**, 113019 (2009).
112. Farrera, P. *et al.* Generation of single photons with highly tunable wave shape from a cold atomic ensemble. *Nature Communications* **7**, 13556 (2016).
113. Pagliano, F. *et al.* Dynamically controlling the emission of single excitons in photonic crystal cavities. *Nature communications* **5**, 1–6 (2014).

114. Bose, R., Cai, T., Choudhury, K. R., Solomon, G. S. & Waks, E. All-optical coherent control of vacuum Rabi oscillations. *Nature Photonics* **8**, 858–864 (2014).
115. Jin, C.-Y. *et al.* Ultrafast non-local control of spontaneous emission. *Nature Nanotechnology* **9**, 886 (2014).
116. Peinke, E. *et al.* Tailoring the properties of quantum dot-micropillars by ultrafast optical injection of free charge carriers. *Light: Science & Applications* **10** (2021).
117. Morin, O., Körber, M., Langenfeld, S. & Rempe, G. Deterministic Shaping and Reshaping of Single-Photon Temporal Wave Functions. *Physical Review Letters* **123** (2019).
118. Stute, A. *et al.* Tunable ion-photon entanglement in an optical cavity. *Nature* **485**, 482–485 (2012).
119. Karaveli, S., Weinstein, A. J. & Zia, R. Direct modulation of lanthanide emission at sub-lifetime scales. *Nano letters* **13**, 2264–2269 (2013).
120. Cuff, S. *et al.* Dynamic control of light emission faster than the lifetime limit using VO₂ phase-change. *Nature communications* **6**, 1–6 (2015).
121. Cano, D. *et al.* Fast electrical modulation of strong near-field interactions between erbium emitters and graphene. *Nature Communications* **11**, 1–8 (2020).
122. Thyrestrup, H., Hartsuiker, A., Gérard, J.-M. & Vos, W. L. Non-exponential spontaneous emission dynamics for emitters in a time-dependent optical cavity. *Optics express* **21**, 23130–23144 (2013).
123. Deshmukh, C. *et al.* Detection of a single erbium ion in a nanoparticle. *To be submitted* (2022).
124. Kinoshita, A. *et al.* Roadmap for Rare-earth Quantum Computing (2021).
125. Di, Z. *et al.* Controlling the emission from semiconductor quantum dots using ultra-small tunable optical microcavities. *New Journal of Physics* **14**, 103048 (2012).